Title

Characteristics and Significance of Chorus-Wave-Driven Relativistic Electron Microbursts in the Earth's Outer Radiation Belt: Wave-Particle Interaction Modeling Studies

Author

Kang, Ning

Publication Date

2025

Peer reviewed|Thesis/dissertation

UNIVERSITY OF CALIFORNIA
Los Angeles

Characteristics and Significance of Chorus-Wave-Driven Relativistic Electron Microbursts in the Earth's Outer Radiation Belt: Wave-Particle Interaction Modeling Studies

A dissertation submitted in partial satisfaction
of the requirements for the degree
Doctor of Philosophy in Atmospheric and Oceanic Sciences

by

Ning Kang

2025

ABSTRACT OF THE DISSERTATION

Characteristics and Significance of Chorus-Wave-Driven
Relativistic Electron Microbursts in the Earth's Outer Radiation Belt:
Wave-Particle Interaction Modeling Studies

by

Ning Kang
Doctor of Philosophy in Atmospheric and Oceanic Sciences
University of California, Los Angeles, 2025
Professor Jacob Bortnik, Chair

This dissertation presents a comprehensive investigation into chorus-wave-driven relativistic electron precipitation in Earth's outer radiation belt through a newly-developed numerical model, emphasizing the microscopic to macroscopic characteristics of relativistic microbursts.

We initially develop the Chorus Induced Particle Precipitation (CIPP) model, designed to simulate detailed precipitation signatures on arbitrary magnetic field lines resulting from equatorially generated chorus waves. The modeling approach accurately captures the spatial and temporal precipitation dynamics and demonstrates robust predictive capability.

We then model the spatial scales of chorus-driven relativistic electron microbursts, finding a typical scale size of approximately 60 km, consistent with observational data. Our results show that the spatial scale of microbursts primarily depends on wave propagation rather than source dimensions. Additionally, microbursts exhibit substantial poleward displacement from chorus wave source regions, challenging the traditional assumption of strict magnetic conjunction and highlighting the importance of non-conjugate geometries.

Extending our framework globally, we simulate chorus sources distributed across various L-shells and magnetic local time sectors. Results demonstrate sector-dependent variations in precipitation, with noon-sector microbursts significantly stronger and broader than those in dawn or midnight sectors, primarily due to reduced Landau damping. These findings highlight the controlling role of $\sim keV$ electron populations in relativistic precipitation processes and provide a quantitative basis for estimating global radiation belt losses.

Subsequently, we estimate relativistic electron lifetimes within the outer radiation belt under chorus-driven precipitation, finding lifetimes ranging from tens of hours in the core belt ($L = 5$–6.5) to significantly longer durations at lower L-shells. Our results confirm that chorus-driven microbursts can efficiently deplete relativistic electron populations on timescales of days, verifying their critical role in radiation belt electron dynamics.

Finally, we demonstrate that efficient night-side relativistic precipitation requires chorus wave ducting by cold plasma density structures. Using multi-spacecraft observations coupled with event-specific modeling informed by ELFIN measurements, we show that ducted waves retain an amplitude sufficient for resonant interactions at high latitudes, with relativistic energies, approaching the strong diffusion limit. Our findings imply that plasma density ducts may be a common and essential feature for relativistic electron precipitation on the night-side, significantly affecting radiation belt dynamics.

We conclude that chorus driven relativistic microbursts have unique and complicated spatiotemporal characteristics, and play an important role in the global radiation belt dynamics.

The dissertation of Ning Kang is approved.

Hao Cao

Roger Varney

Vassilis Angelopoulos

Jacob Bortnik, Committee Chair

University of California, Los Angeles

2025

鹤鸣于九皋，声闻于天。

鱼在于渚，或潜在渊。

——《诗经·小雅·鹤鸣》

The crane cries in the marshland, clear to the heavens its call.

Fishes linger by the islet, or dive deep beyond all.

- "Lesser Hymns: Cranes Calling" from the Classic of Poetry.

TABLE OF CONTENTS

LIST OF FIGURES

LIST OF TABLES

ACKNOWLEDGMENTS

The past five years as a Ph.D. student have been an incredibly precious experience to me. I have learned and grown so much that when I look back at my younger self from five years ago—filled with desire for knowledge and passion for science—I'm struck by how youthful I was, almost to the point where I barely recognize that person as my past self. It has been a challenging yet immensely rewarding journey, and I'm incredibly fortunate to have had the invaluable companionship and support of many mentors, families, and friends along the way, without whom I can never make this far.

First and foremost, I would like to express my most sincere and deepest gratitude to my advisor, Prof. Jacob Bortnik, who provides me enormous support, guidance and encouragement. He always mentors me in a patient and encouraging manner, supports my needs and provides me various opportunities as best as possible, and never hesitates to enthusiastically discuss any scientific problems I encounter. Most importantly, he not only teaches me about science, but also how to be a great scientist. Being a good scientist is to have the ability of analyzing and solving problems - that is perhaps the most valuable lesson I learned from him, and indeed, after five years of his incredible mentorship, I do find myself gradually mastering the problem-solving ability, which I will benefit from in my future science career and beyond.

I would also like to thank my other committee members. I had the honor of taking classes from Prof. Vassilis Angelopolis and Prof. Roger Varney, and I was deeply impressed by their devotion to excellency and really enjoyed their mastery in teaching physics. I also thank Prof. Hao Cao who cared about the life and career of me and many other students. I'm also grateful for all the comments, discussions and feedbacks on my researches from all of my committee members during various circumstances (majorly during SPARTHRB seminars), which are very important support and encouragement to me.

I am very luck to receive a lot of guidance from many senior colleagues to whom I

express my gratitude. Dr. Qianli Ma kindly provided me with many critical supports for my researches and I learned a lot from the amazing discussions with him. Dr. Anton Artemyev shared many interesting research ideas with me and helped a lot when working on these projects together. Dr. Xin An was the first person here dedicating to support me in my research, who guided me through the three-month summer project. Dr. Donglai Ma is an amazing senior student who gave me a lot of advice on research and life. Dr. Seth Claudepierre, being very friendly, helped me starting my very first project after joining the group. I also want to thank Dr. Jabei He, Prof. John Bonnell, Dr. Megha Pandya, Dr. Murong Qin, Prof. Wen Li, Dr. Xiaofei Shi, Dr. Haobo Fu and many other colleagues who worked with me. Finally, I want to express my deep gratitude to Prof. Jinlin Xie, Prof. Xinliang Gao and Prof. Quanming Lu, who are the mentors that led me to take the very first step on the path of space physics till this far.

I would like to thank my good friend Tianyi Wang for having a lot of fun with me, and showing me how to explore the ways of entertaining after work. I thank my former roommates Zesen Huang and Yichen Li and former neighbor Xiaofei Shi for having delicious home-cooked dinner and playing cards everyday. I thank all the friends I meet during each year's GEM and AGU conference: Shujie Gu, Jiabei He, Jinbei Huang, Wei Zhang, Xingzhi Lyu, Yang Mei and many others, with whom I always find these conferences much more enjoyable. I also thank my old friends Yanjie Zeng, Yuanlong Li, Binghao Ouyang and Yingjie Wang from college and Jiewen Xiao from middle school, though we are at different corners of the world now, I miss you.

Finally, I would like to thank my girlfriend Wenqi Zhou for bringing me great happiness and accompanying me through all the difficult times that I had during the past few years. As for my family - my dear parents, grandparents, uncle and aunt, sisters and brothers (cousins), and new-born little nephew - I don't think there are any words in the world that can express my thanks. All I can say is, I can never lose hope in life because of you.

VITA

2016–2020 B.S. in Applied Physics, University of Science and Technology of China, Hefei, Anhui, China.

2020–2023 M.S. in Atmospheric and Oceanic Sciences, University of Clifornia Los Angeles, Los Angeles, California.

2023–present Ph.D. in Atmospheric and Oceanic Sciences, University of Clifornia Los Angeles, Los Angeles, California.

PUBLICATIONS

Kang, N., Bortnik, J., An, X., & Claudepierre, S. G. (2021). Propagation of Chorus Waves Generated in Minimum-B Pockets. *Geophysical Research Letters*, 48(24), e2021GL096478.

Kang, N., & Bortnik, J. (2022). Structure of energy precipitation induced by superbolt-lightning generated whistler waves. *Geophysical Research Letters*, 49(5), e2022GL097770.

Kang, N., Bortnik, J., Zhang, X., Claudepierre, S., & Shi, X. (2022). Relativistic microburst scale size induced by a single point-source chorus element. *Geophysical Research Letters*, 49(23), e2022GL100841.

Kang, N., Bortnik, J., Ma, Q., & Claudepierre, S. (2024). Modeling the global distribution of chorus wave induced relativistic microburst spatial characteristics. *Journal of Geophysical Research: Space Physics*, 129(3), e2023JA032250.

Kang, N., Artemyev, A. V., Bortnik, J., Zhang, X. J., & Angelopoulos, V. (2024). The Principal role of chorus ducting for night-side relativistic electron precipitation. *Geophysical Research Letters*, 51(17), e2024GL110365.

Kang, N., Ma, Q., Bortnik, J., Qin, M., & Li, W. (2025). Ray tracing of whistler mode waves in jupiter's magnetosphere. *Geophysical Research Letters*, 52(5), e2024GL113727.

CHAPTER 1

Introduction

.

1.1 Overview

Relativistic electrons in the Earth's radiation belts are a critical component of space weather, with important implications for satellite operation and space-borne technologies. In this dissertation, we quantitatively examine the characteristics and significance of relativistic electron microbursts driven by chorus waves in the Earth's outer radiation belt. Our analysis spans both microscopic and macroscopic perspectives. On the microscopic level, we investigate the features of individual relativistic microbursts and explore how these features relate to properties of the driving chorus waves. On the macroscopic level, we characterize the global distribution of various microburst features and assess their overall impact on radiation belt dynamics.

The primary tool we use for these studies is an advanced numerical model we developed called Chorus Induced Particle Precipitation (CIPP) code, which is designed to model the electron precipitation via wave-particle interaction with chorus waves. The code is different from any existing numerical models focusing on chorus wave induced precipitation to the author's knowledge, due to its ability to describe the precipitation signatures over different locations induced by one chorus wave event.

We will investigate the following specific areas: 1) determining the spatiotemporal char-

acteristics of a single chorus-wave-driven microburst, with emphasis on the spatial scale size of the microburst; 2) establishing a global distribution of the spatial scale size of the chorus wave driven microburst based on chorus wave statistical results; 3) estimating the global impact of chorus wave driven microburst on the relativistic electron loss in the outer radiation belt by modeling the lifetime; 4) preliminary elucidating the role that density ducts play in the chorus wave driven relativistic microburst.

1.2 Scientific background

The Earth's radiation belts are a highly dynamic system, and the studies on its dynamics are drawing a lot of attention. The Earth's outer radiation belt dynamics is controlled by various processes [118, 146]. In this section, we introduce the topics that are of interest in this dissertation, namely an overview on the basic concepts of Earth's radiation belts, the loss process involved in electron microburst, and the chorus waves and their relation to the microburst.

1.2.1 The Earth's radiation belts

It has long been known that near-Earth space is full of high-energy particles since the revolutionary discovery using the Explore I spacecraft by Van Allan in 1958 [156], after whom the Van Allan radiation belts are named. Current understanding indicates that the radiation belts consist of two parts. The inner belt, centered at L-shell of 1.5, consists dominantly of high energy protons with energies $E > 10MeV$ [89], and is usually rather stable. The outer belt, on the other hand, is located between $4 < L < 6$, primarily consists of high energy electrons with energy $E > 100keV$, and is much more variable and dynamical [146, 154, 86]. Recently, the discovery of a (temporary) third radiation belt was reported [17, 99], showing the highly dynamic nature of the outer radiation belt. In between the inner and outer radiation belt ($2 < L < 3$) is the so called slot region, where the flux level of high energy

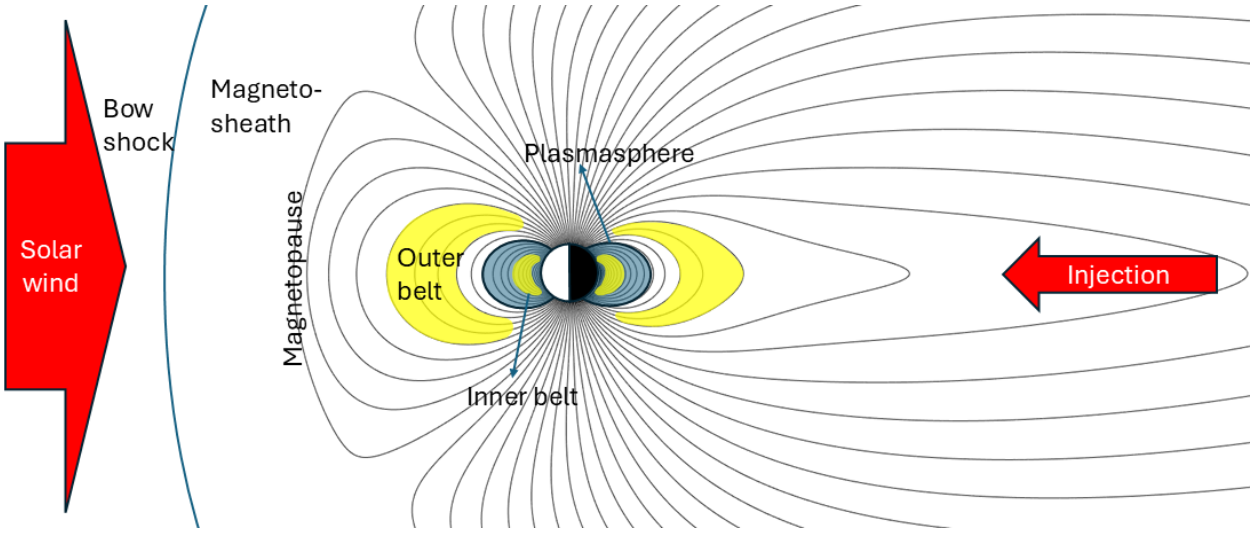

Figure 1.1: An illustration of the structure of Earth's magnetosphere and radiation belts.

particles stays low. The slot region is usually considered to be formed by loss mechanisms controlled by wave activities [95]. A sketch of the radiation belt configuration in the Earth's magnetosphere is illustrated in Figure 1.1.

To understand the dynamics of energetic particles in the radiation belts, we need to understand the motion of a single particle in the Earth's magnetic field. The particle motion has three characteristic periodic motions: 1) gyro motion where particle cycles around a field line; 2) bounce motion where particle bounces back and forth along a field line (thus get trapped in the magnetosphere); 3) drift motion where particle drifts across field lines around the Earth. According to classical mechanics theory, each periodic motion corresponds to an adiabatic invariant whose value is conserved, namely the magnetic moment μ, longitude invariant I, and total magnetic flux Φ. In the absence of perturbing forces, the adiabatic invariants will stay conserved and the periodic motions will be maintained. If a particle can complete a full period of all three periodic motions, the conservation of adiabatic invariants will guarantee this particle can stay in the periodic trajectory and thus is *trapped* in the magnetosphere. On the other hand, if any part of the trajectory is within the dense ionosphere, then the particle will get lost into the ionosphere due to collisions with neutrals and

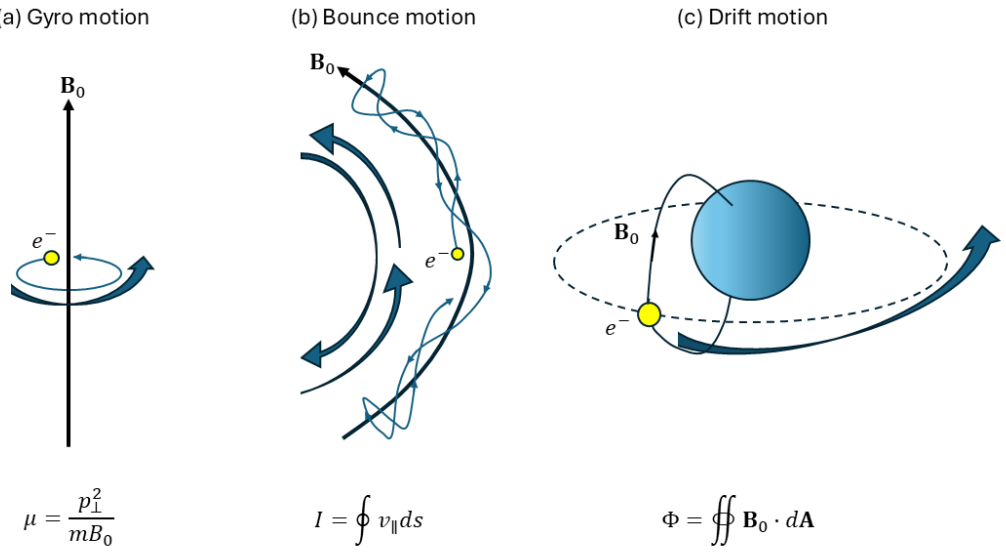

Figure 1.2: Illustration of three periodical motions of particles in the radiation belt and the corresponding adiabatic invariants. (a) gyro motion, (b) bounce motion and (c) drift motion.

	Gyro motion	Bounce motion	Drift motion
Typical period	$0.01 - 0.1ms$	$0.1 - 1s$	$10 - 1000s$
Typical frequency	$10 - 100kHz$	$1 - 10Hz$	$1 - 100mHz$
Adiabatic invariant	$\mu = \frac{p_\perp^2}{mB_0}$	$I = \oint v_\parallel \mathrm{d}s$	$\Phi = \oiint \mathbf{B}_0 \cdot \mathrm{d}\mathbf{A}$

Table 1.1: Three adiabatic motions of electrons and their corresponding typical periods, frequencies and adiabatic invariants.

not be able to come back to the magnetosphere, or called *precipitated*.

Each motion has a typical period range that does not overlap with each other, where the gyro motion is the fastest and the drift motion is the slowest, as listed in Table 1.1. To break the conservation of these adiabatic invariants, perturbation with a comparable frequency of the corresponding periodic motion is required, which forms the foundation of resonant wave-particle interaction. For the interest of this dissertation, we focus on a certain kind of perturbation with frequency $\approx 10kHz$, namely the chorus waves to be introduced later, which can break the conservation of the first adiabatic invariant μ, and is thus capable of scattering the trapped electrons out of the trapped state and getting precipitated into the atmosphere.

The energetic electrons in the radiation belts, especially those with relativistic energy $\geq 1MeV$ are often called "killer" electrons, as they can potentially damage the electronics and human, therefore pose severe threats to the spacecrafts and astronauts traveling through the radiation belts [15, 16, 158, 42]. Therefore, better understanding the dynamics of the radiation belts, especially the highly variable outer radiation belt which contains lots of killer electrons, is crucial for the utilization and the exploration of the near-Earth space environment as well as transit to outer space (e.g., cis-lunar space, Mars, and outer planets).

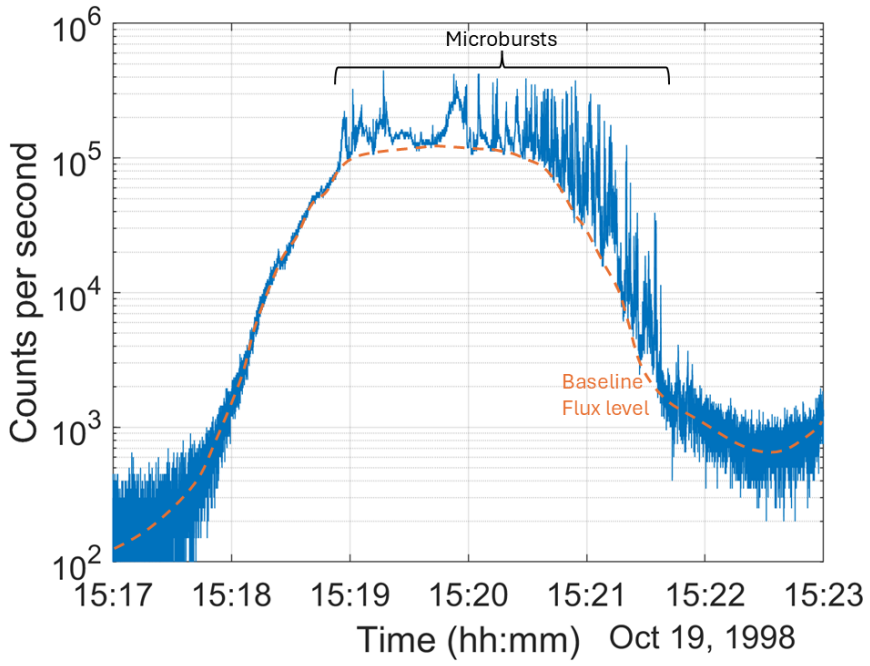

Figure 1.3: Electron $> 1MeV$ microbursts on October 19, 1998 observed by SAMPEX, as reported by [92].

1.2.2 Microburst precipitation

Microbursts are impulsive electron precipitation bursts with individual burst durations of less than 1 s. They are observed across a wide energy spectrum, ranging from several tens of keV [6, 105] to multiple MeV [92, 47, 63]. First discovered using balloon-borne X-ray detector arrays [6], microbursts have since been extensively studied through low Earth orbit (LEO) spacecraft observations [63, 92, 91, 19, 163, 113]. We refer to microbursts with energies ≥ 1 MeV as relativistic microbursts. Figure 1.3 shows a typical event of this kind, originally reported by [92]. The characteristic features are evident: a sudden increase in precipitation flux with a short duration, often forming a train of tens to hundreds of microbursts occurring within a short interval.

Previous statistical studies have characterized the global distribution of relativistic microbursts [47]. They are predominantly observed outside the plasmapause, within the

$3 < L < 7$ range. Their primary occurrence in magnetic local time (MLT) spans from midnight to early afternoon ($0 <$ MLT < 13), with peak activity in the morning sector. The occurrence rate is strongly modulated by geomagnetic activity—higher activity levels lead to more frequent microbursts and shift the peak occurrence to lower L-shells. Notably, these distribution characteristics closely resemble those of chorus waves, as will be discussed later. The durations of microbursts have also been investigated: Shumko et al. [132] found that bursts last approximately 80 ms in the dawn and night sectors, and extend to around 160 ms in the noon sector. However, no statistical results regarding the spatial scale size of relativistic microbursts have been reported, due to limitations that will be discussed in Section 3.1.

Microbursts are widely believed to play a key role in relativistic electron loss from the radiation belts. Lorentzen et al. [92] and Breneman et al. [30] performed event-based estimates of loss rates and concluded that microburst-induced precipitation can lead to substantial depletion of relativistic electrons, potentially emptying an entire flux tube within approximately 10 hours. In some cases, nearly complete loss during a single geomagnetic storm has been reported [92]. Additional statistical studies [46, 145, 54] suggest that microburst-driven electron lifetimes range from tens to hundreds of hours. Beyond their influence on radiation belt dynamics, microbursts significantly impact atmospheric composition by enhancing HO_x and NO_x levels and promoting ozone depletion in the upper mesosphere and lower thermosphere [100, 104, 125]. Consequently, microbursts are vital for advancing our understanding of radiation belt loss processes and the coupling between the magnetosphere, ionosphere, and atmosphere.

1.2.3 Chorus waves

Whistler-mode chorus waves are intense, naturally occurring electromagnetic emissions in the extremely/very low frequency (ELF/VLF) range (hundreds of Hz to several kHz), primarily observed outside the plasmapause in Earth's magnetosphere [33, 151, 103]. Chorus emissions

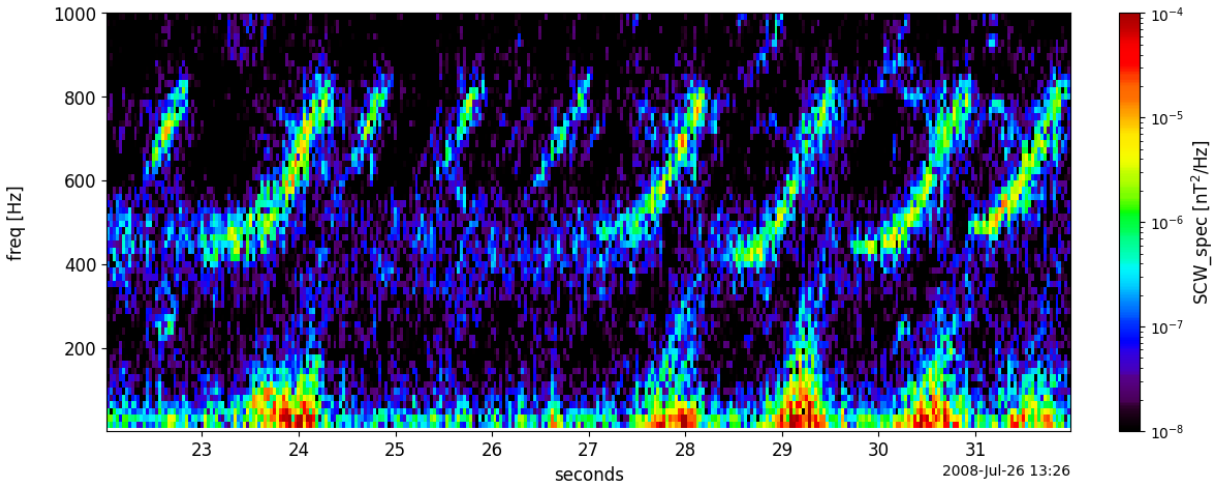

Figure 1.4: An example of a chorus wave event observed by THEMIS A on July 26, 2008.

are composed of discrete elements with characteristic frequency chirping—rising or falling tones lasting $\approx 0.1-0.3s$, clustered in longer modulations from a few seconds to minutes [121]. Figure 1.4 shows an example of the typical rising tone chorus wave elements observed by Time History of Events and Macroscale Interactions during Substorms (THEMIS) mission [8]. It is called "chorus" because when converted to audio signal, the typical rising tone spectra fall into the audio frequency range and sound like chirping chorus.

Chorus waves are generated through cyclotron resonance with anisotropic electrons injected from the plasma sheet, typically with energies from a few to tens of keV and with temperature anisotropy where perpendicular temperature exceeds parallel temperature ($T_\perp > T_\parallel$) [75, 76, 151, 51, 115]. The source region is generally located near the geomagnetic equator [82, 121, 88], though some dayside events may originate at higher latitudes [155, 67, 152]. Chorus waves are usually split into a lower band ($0.1 - 0.5f_{ce}$ where f_{ce} is the equatorial electron gyrofrequency) and an upper band ($0.5 - 0.8f_{ce}$), separated by a spectral gap near $0.5f_{ce}$ [83, 50]. Chorus activity is highly dependent on geomagnetic conditions and shows strong correlation with substorm-driven AE indices [103, 88].

The physical features of chorus vary with MLT, L-shell, and magnetic latitude. Large-

amplitude lower-band chorus ($> 300pT$) occurs mainly from premidnight to postdawn near the equator at $L < 8$ [88, 102], while weaker emissions extend through the noon and dusk sectors. Wave normal angle statistics show that strong lower-band chorus is typically field-aligned (wave normal angle $< 20°$), while more oblique propagation occurs for weaker waves, especially on the dayside [88, 102]. Nightside lower-band chorus is usually confined within $\pm 10°$ magnetic latitude (MLAT), whereas dayside emissions extend to higher latitudes. Upper band chorus differs from the lower band in having weaker amplitudes, more oblique propagation, and spatial confinement to $L < 8$ and $|MLAT| < 10°$ [122, 88]. These differences may arise from stronger Landau damping at higher frequencies [114]. Recent statistical studies confirm that both bands are predominantly generated within $|MLAT| < 3°$ of the magnetic equator [143].

Chorus waves are critical to radiation belt dynamics and magnetospheric energy transfer. They can accelerate electrons from hundreds of keV to MeV energies via linear and nonlinear cyclotron resonance [60, 61, 147], significantly enhancing the outer radiation belt during geomagnetic storms [117]. Simultaneously, chorus can scatter low energy ($0.1 - 100keV$) electrons into the atmospheric loss cone, producing diffuse and pulsating auroras [146, 112], and can scatter relativistic energy $\approx 1MeV$ electrons [91, 37]. The wave-particle interaction regime is amplitude-dependent: low-amplitude chorus induces quasi-linear diffusion, while large-amplitude elements cause nonlinear pitch-angle scattering, leading to rapid precipitation and energy loss [4, 29]. Moreover, chorus emissions that propagate into the plasmasphere are thought to be a major source of plasmaspheric hiss [28, 27], which contributes to the formation and maintenance of the two-belt radiation belt structure [95]. As such, chorus waves are a key agent in both energization and loss processes across the radiation belts, making their detailed understanding essential for space weather modeling and prediction.

1.2.4 Relationship between chorus waves and relativistic electron microbursts

It is widely accepted that chorus waves are a primary driver of relativistic electron microbursts. A large number of statistical studies support the connection between chorus waves and relativistic electron microbursts. Both phenomena are found to occur more frequently during geomagnetically active periods, especially in association with substorms and enhanced AE indices. Microbursts and chorus also share similar spatial distributions: they are typically observed outside the plasmapause, concentrated in the dawnside sector, and peak in occurrence between L-shell of 4 and 6 [47, 110, 163]. The magnetic local time and L-shell distributions of chorus and microbursts closely align, indicating that they are likely linked through the same generation region. Furthermore, microbursts often appear in short trains—multiple precipitation events spaced less than one second apart over durations of 10–15 seconds [6, 150]. This temporal structure is consistent with the amplitude modulation of chorus wave packets, which are also known to vary on similar timescales.

In addition to statistical correlations, direct satellite observations have shown strong one-to-one correspondence between equatorial chorus waves and low-altitude microburst detections. Multi-point measurements have captured simultaneous signatures of intense chorus wave activity near the magnetic equator and bursts of relativistic electron precipitation detected by low-Earth orbiting spacecraft along connected field lines. Such conjunctions have been reported in several studies [91, 77, 30], often showing close timing and spatial alignment between chorus wave packets and individual microbursts. These event-based observations provide strong support for the idea that chorus waves directly scatter radiation belt electrons into the loss cone, producing the observed precipitation signatures.

The ability of chorus waves in driving microbursts has also been indicated by various numerical simulation models, for example, particle-in-cell (PIC) simulation by Hikishima et al. [59], test particle model by Bortnik et al. [23] and Chen et al. [37, 40, 39], and time-of-flight model by Miyoshi et al. [106, 107, 120]. These works all show a one-to-one correlation

between equatorially generated chorus wave event and microburst, reflecting the underlying wave-particle interaction mechanisms between chorus waves and electrons that causes the microburst.

1.3 Open scientific questions: from microscopic to macroscopic aspects

The previous studies we reviewed in Section 1.2 have greatly expanded our understanding of the origin and role of the relativistic microbursts in the Earth's radiation belts. However, there are still several questions that have not been addressed. We can separate these questions into two categories: the microscopic aspect that focuses on the physical mechanism of how a single chorus wave element drives a single microburst, and the macroscopic aspect that focuses on the global distribution of microburst features and the global impact of microbursts. In this dissertation we will address these questions as follows.

Despite the extensive studies on the wave-particle interactions between chorus waves and electrons, it is quite common for investigations to only consider the interaction on a single field line, i.e., the field line where chorus waves are equatorially generated [29, 107, 97, 30, 91, 59, 114, 120]. Often the implications behind such an assumption is the strict field aligned propagation of chorus waves, sometimes even the strictly parallel $\mathbf{k}$ vector along the ray paths. This assumption makes the analysis unable to study a spatial distribution over different L-shells, and furthermore, it is known that a strictly parallel propagating, field line guided chorus waves are relatively uncommon in a smooth, inhomogeneous magnetosphere [80, 121]. Therefore, current research neglects the precipitation occurring on field lines away from the chorus wave equatorial source region, and thus we know very little about the spatial characteristics of the microbursts. This is a major gap of our understanding in the microscopic aspect of chorus driven microburst.

We also raise two questions concerning the macroscopic aspect. Due to the limitation of

single spacecraft in situ observation, we don't have the ability to widely obtain the microburst scale size from spacecraft observations. Currently we only have very limited case studies reporting the microburst scale size of single events, therefore we have very little understanding of the global distribution of microburst spatial characteristics. Moreover, current research on the electron lifetime due to microburst, mentioned in Section 1.2.2, are all based on direct observations of microbursts, therefore do not reveal the relation between global electron loss and the driver of microburst, the chorus waves. In other words, even though we know both the role of chorus waves driving microbursts and the impact of microbursts driving global electron loss, there is still a knowledge gap in linking the the chorus waves and global electron loss due to microbursts.

1.4 Thesis organization and major contributions

This dissertation is organized into the following 7 chapters:

Chapter 1 (the current section) introduces the basic concepts of microbursts in Earth's radiation belts and their relation to chorus waves, reviews related past work and current knowledge gaps, and raises the scientific questions that we address in this dissertation.

In Chapter 2 we introduce the numerical simulation tools we developed for our analysis, the Chorus Induced Particle Precipitation (CIPP) code. We comprehensively introduce the technical details of the code's algorithm, serving as a technical summary report.

Chapter 3 is devoted to a single event analysis using the CIPP code, which serves as a detailed demonstration of the capabilities of the CIPP code, as well as investigates the microscopic questions of chorus driven precipitation signatures at arbitrary field line and microburst spatial charateristics such as scale size.

Chapter 4 turns to macroscopic questions of the global distribution of microburst spatial charateristics. Utilizing the ability of our CIPP code, we model the microburst spatial charateristics at different L-MLT magnetosphere locations based on the global distribution

of chorus waves.

Chapter 5 estimates the lifetime of the relativistic electrons due to chorus driven microbursts, therefore address the ultimate goal of studying the macroscopic questions: understand how chorus waves contribute to relativistic electron loss and to assess their overall significance in this process.

Chapter 6 serves as an adjunct study where we make a preliminary attempt to study the chorus-driven microburst under a special condition: a density duct. We will explore the unique characteristics of microburst driven by ducted chorus waves via a single event-based modeling study.

Finally, in Chapter 7 we summarize the results presented in Chapter 3 to 6, discuss implications and limitations of these works, and conclude with proposing potential future works.

The key contributions of this dissertations are summarized below:

- We identified new characteristics of chorus-driven relativistic microbursts: the typical spatial scale is on the order of several tens of kilometers even under point-source assumptions; relativistic microbursts tend to occur at higher L-shells than their driving chorus waves; and they exhibit poleward motion with ground velocities of several hundred km/s. These features are consistent with expected chorus wave propagation effects, suggesting that such propagation may play a dominant role in shaping microburst spatiotemporal characteristics.

- We modeled the global distribution of microburst properties based on the statistical distribution of chorus waves and background plasma conditions. The results indicate that microbursts in the dawn and night sectors share similar scale sizes and maximum fluxes, whereas those in the noon sector tend to have larger spatial scales and stronger fluxes, likely due to reduced Landau damping of chorus waves near noon.

- We estimated relativistic electron lifetimes in the outer radiation belt due to chorus-

driven microbursts, using statistical chorus wave data. The resulting lifetimes, typically on the order of several tens of hours, provide a theoretical link between chorus wave activity and electron loss timescales, reinforcing the role of chorus waves in outer belt depletion.

- We conducted a case study of relativistic microbursts associated with ducted chorus wave propagation. Through event-specific modeling of a strong night-side precipitation event, we demonstrated that ducting may play a key role in enabling significant precipitation by mitigating strong Landau damping. This result suggests that pronounced relativistic precipitation on the night side is likely facilitated by ducted wave propagation.

CHAPTER 2

Theoretical background of the modeling method

In this chapter, we introduce our modeling tool, the Chorus Induced Particle Precipitation (CIPP) code, that is used in the following chapters in great detail. The prototype of the CIPP code is the Whistler Induced Particle Precipitation (WIPP) code, which was developed by Bortnik et al. [25, 26] two decades ago to investigate the electron precipitation induced by lightning generated whistlers (LGW). Despite its powerful capability to calculate precipitation signatures across field lines with a rather low computational cost, it has met very limited application and drawn very little attention after its development until recently, we systematically reviewed this code, addressed outstanding issues, and most importantly, upgraded it into the CIPP version so that it can be applied to model the precipitation induced by not only the ionospherically originated LGW waves (which was its original purpose) but also equatorially generated chorus waves, which have drawn more and more attention in recent years.

The CIPP code inherits the virtues of the WIPP code: taking the full propagation effect of waves into account, enabling the cross field line precipitation analysis for a single event, and the relatively low cost for wave-particle interaction calculation by adopting a few quasi-linear assumptions. These features make the CIPP code an ideal tool to overcome the single field line limitation inherent in many existing chorus wave-particle interaction studies. The other side of coin that we shoule bear in mind is the limitation inherited: it does not involve any feedback from particle to waves, and it does not involve any nonlinear effect for wave propagation, generation or wave-particle interaction, which necessarily limits application to

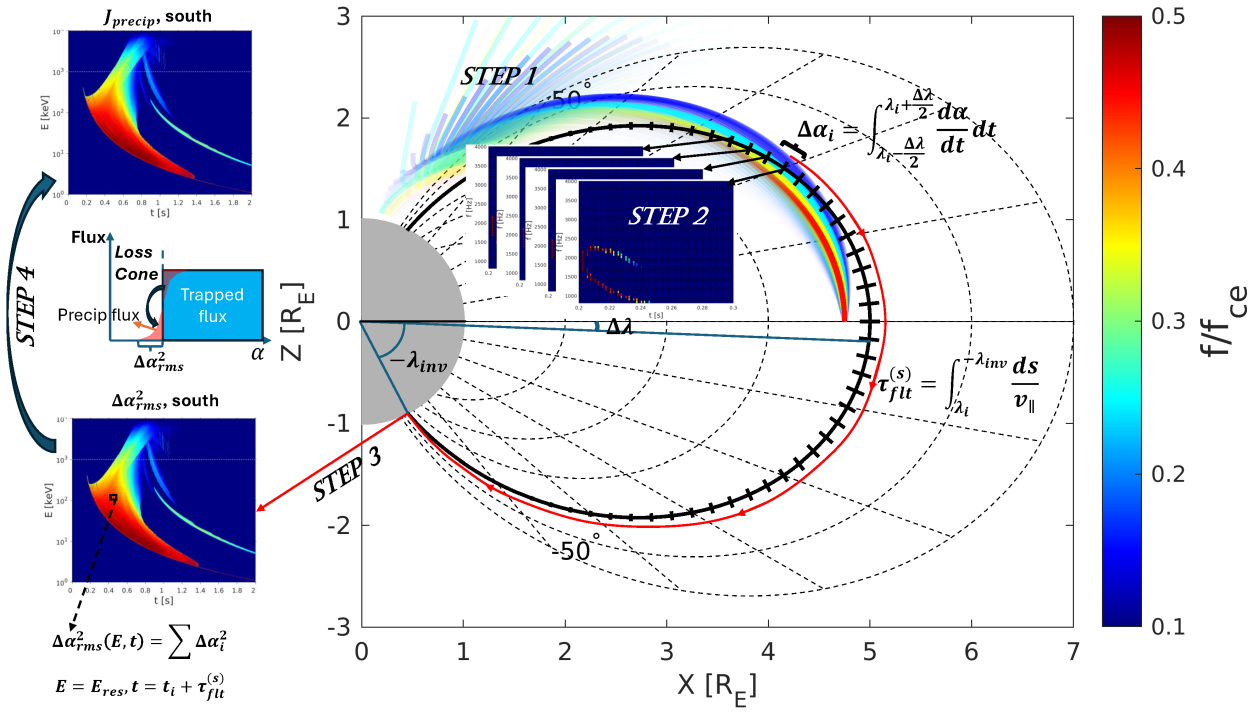

Figure 2.1: Workflow sketch of CIPP code, showing how the code starts with ray tracing of chorus waves to calculate the final result: the $E - t$ spectrum of precipitated flux on both northern and southern foot points of a certain field line. Here, only the precipitated flux in the southern hemisphere is shown but the same procedure applies to the northern hemisphere.

low and moderate intensity waves.

We introduce the technical details of the CIPP codes in the remaining part of this chapter. in Section 2.1 we introduce the top level workflow structure which consists of four major parts, and Section 2.2 to 2.5 introduce how each of the four major parts work. This chapter will serve as a technical summary report of the CIPP code.

2.1 The basic workflow of the Chorus Induced Particle Precipitation (CIPP) code

The purpose of the CIPP code is to calculate the energy-time ($E-t$) spectrum of the precipitated flux J_{precip} at the footpoints of *any* field lines due to a given chorus wave element. The most interesting feature about the CIPP code is that because we can in principle run the code for any field line simultaneously, in practice we often run it on multiple field lines, whose footpoints on ionosphere provide the valuable information about the spatial distribution of J_{precip}. The calculation over multiple field lines is just a simple repetition of the procedure on one field line, therefore we will only introduce how the code works to calculate $J_{precip}(E,t)$ for just one single field line.

The basic workflow of the CIPP code is shown in Figure 2.1. We divide the procedure into four steps, which are marked in Figure 2.1. The first step is to initialize chorus waves and trace their propagation trajectories using the ray tracing technique. This step, in principle, provides a full description of the chorus wave propagation and evolution.

The next step is to encode the wave information for those propagating through the target field line (we use the $L=5$ field line marked with thick line in Figure 2.1 as an example). For this purpose we divide the field line into small segments with latitude interval $\Delta\lambda$, and assign an effective area (EA, shown as the small areas perpendicular to the target field line) to each of these segments. If a ray cross through an EA, then the current wave information (current time, frequency, wave power, WNA, etc.) will be recorded and linked with the corresponding EA. After Step 2, each EA will establish an $f-t$ spectrum of wave information belonging to its small segment, as shown in Figure 2.1.

Step 3 is to calculate the $E-t$ spectrum of the scattered pitch angle at the both footpoints of the target field line. For each wave crossing an EA, we can calculate the resonance energy E_{res}, the flight time t_{flt} the electron need to travel from this EA to the ionosphere, and the scattered PA $\Delta\alpha$ by integrating $\frac{\mathrm{d}\alpha}{\mathrm{d}t}$ (determined by electron dynamic equations) over the

time electron need to travel through the small field line segment corresponding to this EA. This wave will then contribute a scattered PA $\Delta\alpha^2$ to the footpoint for energy E_{res} at arrival time $t = t_{cross} + t_{flt}$, where t_{cross} is the time when wave crosses the EA. We sum up over $\Delta\alpha^2$ instead of $\Delta\alpha$ to follow the quasi-linear assumption that variance increases linearly as a function of time, which we will discuss later.

The final step is to convert the $E - t$ spectrum of the scatted PA $\Delta\alpha^2_{rms}$ into the precipitation flux. This is achieved by introducing a new input dataset: the trapped flux. The scatted PA $\Delta\alpha^2_{rms}$ is a proxy indicating how many electrons will be scattered from just outside the loss cone (trapped flux) into the loss cone and get lost, as illustrated in the sketch of Figure 2.1. After this step we obtain our final product, $J_{precip}(E, t)$ on the target field line.

Next we will introduce each step in more detail in the following sections.

2.2 Tracing the wave power propagation trajectories

The purpose of this step is to initialize a chorus wave event and trace where the wave power propagates to. This requires the following data as input: 1) initial conditions of the chorus waves, including the equatorial source location (we will assume the chorus waves are all originated from the equator throughout) and the initial wave power density function; 2) environmental condition which determines the propagation trajectories of chorus waves, including magnetic field and cold electron density distribution (we will assume a standard dipole field geometry throughout); and 3) energetic electron flux at the Landau resonance energy range for Landau damping calculation. The method we use is the ray tracing technique, whose principles are introduced below.

2.2.1 The ray tracing method

The ray tracing method is an efficient technique used to simulate the propagation of waves in an inhomogeneous medium, first developed by Haselgrove [57] and introduced to wave studies

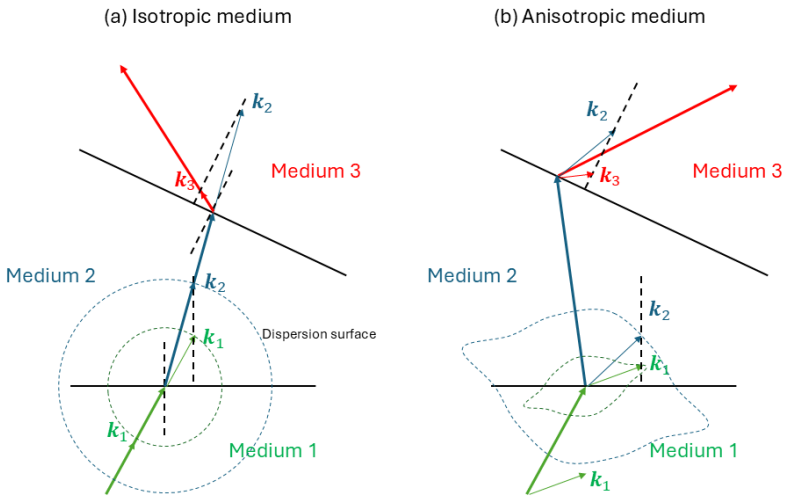

Figure 2.2: Ray tracing techniques explained with Snell's Law, in both the (a) isotropic and (b) anisotropic media

in the magnetosphere by Kimura [78]. This method assumes a plane wave propagating with a fixed frequency, and therefore the wave can be described as a simple ray. The ray path is described by the Snell's Law, which demands the tangential components of wave vector $\mathbf{k}$ on both sides of a medium stratification to be continuous, as indicated in Figure 2.2. The famous Snell's Law formula for common isotropic optical medium $n_1 \sin\theta_1 = n_2 \sin\theta_2$ provides a very straightforward slab-by-slab approach to trace the ray path, as shown in Panel (a) of Figure 2.2. However, the complexity that prevent us from doing so for waves in the magnetosphere is that the magnetized plasma is a highly anisotropic medium, which means 1) Snell's Law does not provide a simple and intuitive geometric approach to determine the wave normal vector, and 2) the ray propagation direction is in general not aligned with the wave normal direction, therefore an additional calculation for the group velocity direction is still needed even if we obtain the wave normal direction. These complexities are illustrated in Panel (b) of Figure 2.2.

To address these difficulties, Haselgrove [57] transformed the Snell's Law into an equivalent set of ordinary differential equations (ODEs) simultaneously describing the evolution of both the ray location and wave normal direction, which is repeated below as given by Kimura [78]:

$$\begin{cases} \dfrac{\mathrm{d}r}{\mathrm{d}t} = \dfrac{1}{\mu^2}(\rho_r - \mu\dfrac{\partial\mu}{\partial\rho_r}), \\ \dfrac{\mathrm{d}\chi}{\mathrm{d}t} = \dfrac{1}{r\mu^2}(\rho_\chi - \mu\dfrac{\partial\mu}{\partial\rho_\chi}), \\ \dfrac{\mathrm{d}\phi}{\mathrm{d}t} = \dfrac{1}{r\mu^2\sin^2\chi}(\rho_\phi - \mu\dfrac{\partial\mu}{\partial\rho_\phi}), \\ \dfrac{\mathrm{d}\rho_r}{\mathrm{d}t} = \dfrac{1}{\mu}\dfrac{\partial\mu}{\partial r} + \rho_\chi\dfrac{\mathrm{d}\chi}{\mathrm{d}t} + \rho_\phi\dfrac{\mathrm{d}\phi}{\mathrm{d}t}\sin\chi, \\ \dfrac{\mathrm{d}\rho_\chi}{\mathrm{d}t} = \dfrac{1}{r}(\dfrac{1}{\mu}\dfrac{\partial\mu}{\partial\chi} - \rho_\chi\dfrac{\mathrm{d}r}{\mathrm{d}t} + r\rho_\phi\dfrac{\mathrm{d}\phi}{\mathrm{d}t}\cos\chi), \\ \dfrac{\mathrm{d}\rho_\phi}{\mathrm{d}t} = \dfrac{1}{r\sin\chi}(\dfrac{1}{\mu}\dfrac{\partial\mu}{\partial\phi} - \rho_\chi\dfrac{\mathrm{d}r}{\mathrm{d}t}\sin\chi - r\rho_\phi\dfrac{\mathrm{d}\chi}{\mathrm{d}t}\cos\chi). \end{cases} \tag{2.1}$$

Here the ray location is described in spherical coordinate (r, χ, ϕ), μ is the refractive index, and the vector $\boldsymbol{\rho} = \rho_r\hat{\mathbf{r}} + \rho_\chi\hat{\boldsymbol{\chi}} + \rho_\phi\hat{\boldsymbol{\phi}}$ is defined as $\boldsymbol{\rho} = \frac{c\mathbf{k}}{\omega} = \mu\hat{\mathbf{k}}$ (where c is the speed of light and ω is the wave's angular frequency), which is the vectorized refractive index with direction of wave normal $\mathbf{k}$ and length of μ. Equation 2.1 is a complete set of first order ODEs, and can be numerically solved with standard methods such as Runge-Kutta method [119, 79].

It is important to point out that the variable t in Equation 2.1 is not time, but an integration variable with dimension of length. Its connection to the real time, or precisely, the group time defined as $t_g = \int \frac{ds}{v_g}$ where ds is the distance traveled by the ray and v_g is the group velocity, that is directly related to the energy propagation of the wave, is through the following equation:

$$\frac{\mathrm{d}t_g}{\mathrm{d}t} = \frac{1}{c}(1 + \frac{\omega}{\mu}\frac{\mathrm{d}\mu}{\mathrm{d}\omega}). \tag{2.2}$$

We will adopt a 2D version of the ray tracing equation by conducting the ray tracing only in a meridional plane. By setting ϕ as a constant and $\rho_\phi = 0$ (assuming the longitu-

dinal deflections is negligible because the gradients in the cold plasma density distributions in longitudinal direction is much smaller than radial and polar directions), we can reduce Equation 2.1 into a set of 2D ray tracing equations:

$$\begin{cases} \dfrac{\mathrm{d}r}{\mathrm{d}t} = \dfrac{1}{\mu^2}(\rho_r - \mu\dfrac{\partial\mu}{\partial\rho_r}), \\ \dfrac{\mathrm{d}\chi}{\mathrm{d}t} = \dfrac{1}{r\mu^2}(\rho_\chi - \mu\dfrac{\partial\mu}{\partial\rho_\chi}), \\ \dfrac{\mathrm{d}\rho_r}{\mathrm{d}t} = \dfrac{1}{\mu}\dfrac{\partial\mu}{\partial r} + \rho_\chi\dfrac{\mathrm{d}\chi}{\mathrm{d}t}, \\ \dfrac{\mathrm{d}\rho_\chi}{\mathrm{d}t} = \dfrac{1}{r}(\dfrac{1}{\mu}\dfrac{\partial\mu}{\partial\chi} - \rho_\chi\dfrac{\mathrm{d}r}{\mathrm{d}t}). \end{cases} \tag{2.3}$$

In the 2D case, the spherical coordinates degenerate into polar coordinates. We usually define the dipole direction as the polar axis, then the polar angle χ can be related to the latitude λ through $\lambda = \frac{\pi}{2} - \chi$.

From Equation 2.3 we can see that the driver of the ray propagation is the refractive index $\mu(r, \chi; \rho_r, \rho_\chi)$. Therefore we need to find the expression for the refractive index. Throughout this work we will adopt the cold plasma assumption, and then the refractive index can be derived from linear dispersion theory [138]:

$$\begin{vmatrix} S - \mu^2\sin^2\theta & -iD & \mu^2\sin\theta\cos\theta \\ iD & S - \mu^2 & 0 \\ \mu^2\sin\theta\cos\theta & 0 & P - \mu^2\sin^2\theta \end{vmatrix} = 0, \tag{2.4}$$

where i is the imaginary unit satisfying $i^2 = -1$, θ is the wave normal angle defined as the angle between wave normal $\mathbf{k}$ and the local ambient magnetic field $\mathbf{B}_0$, $S = \frac{R+L}{2}$ and $D = \frac{R-L}{2}$, and P, R, L are the Stix parameters defined as:

$$\begin{cases} P = 1 - \sum\limits_s \dfrac{\omega_{ps}^2}{\omega^2}, \\ R = 1 - \sum\limits_s \dfrac{\omega_{ps}^2}{\omega(\omega + \Omega_s)}, \\ L = 1 - \sum\limits_s \dfrac{\omega_{ps}^2}{\omega(\omega - \Omega_s)}, \end{cases} \tag{2.5}$$

where $\omega_{ps} = \sqrt{\frac{n_s q_s^2}{\epsilon_0 m_s}}, \Omega_s = \frac{q_s B_0}{m_s}$ are the plasma frequency and signed gyrofrequency of particle species s with charge q_s (can be both positive or negative), mass m_s and density n_s. ω_{ps}, Ω_s are function of location r, χ through their dependence on n_s and B_0, and the location dependence is further passed to P, S, D via ω_{ps}, Ω_s and finally to μ.

After some straightforward algebraic manipulation, Equation 2.4 can be reduced to a quadratic equation of μ^2:

$$A\mu^4 - B\mu^2 + C = 0, \tag{2.6}$$

where

$$\begin{cases} A = S\sin^2\theta + P\cos^2\theta, \\ B = RL\sin^2\theta + SP(1+\cos^2\theta), \\ C = PRL, \end{cases} \tag{2.7}$$

Equation 2.6 can be easily solved with two solutions: $\mu^2 = \frac{B \pm \sqrt{B^2 - 4AC}}{2A}$. These two solutions correspond to the two branches of plasma waves in the cold magnetized plasma. Since we are interested in the chorus waves, we will only select the whistler-mode wave branch as the solution for μ^2:

$$\mu^2 = \frac{B - \sqrt{B^2 - 4AC}}{2A}. \tag{2.8}$$

Equation 2.8 provides the full description of $\mu(r, \chi; \rho_r, \rho_\chi)$. The dependence on ρ_r, ρ_χ is obtained through the WNA θ, which, combined with the known direction of ambient field $\hat{\mathbf{b}}_0$, yields the direction of $\hat{\mathbf{k}}$, and ρ_r, ρ_χ can be calculated from $\rho_r \hat{\mathbf{r}} + \rho_\chi \hat{\boldsymbol{\chi}} = \mu \hat{\mathbf{k}}$.

To initialize the ray tracing run, we set the ray initial location (r_0, χ_0) to be the chorus equatorial source region $(L_{src} R_E, \pi/2)$. A chorus wave element can contain different frequency modes and different WNAs, which can be described with a wave power density function $P(f, \theta)$. We can select a frequency and WNA interval $\Delta f, \Delta\theta$, and the chorus wave element with $P(f, \theta)$ can be represented by a series of rays with frequency f_i, initial WNA θ_i, and initial wave power $P(f_i, \theta_i)\Delta f \Delta\theta$. By tracing these rays we can simulate the propagation of this chorus wave element.

We use the Stanford ray tracer [64, 160, 137, 157, 44] to conduct the ray tracing technique we described above.

2.2.2 Landau damping calculation

Although we assume cold plasma dispersion relation in the ray tracing part, which introduces no energy dissipation, a damping mechanism is still needed because the rapid wave power loss as chorus waves propagate to higher latitudes has been shown to be a key feature of chorus waves [103]. Failure to describe the damping behavior of waves will result in unrealistic wave power distribution. Therefore, it is crucial to introduce the most important damping mechanism, Landau damping, into our ray power calculation.

We will follow Brinca's method [31] to introduce Landau damping into a cold plasma dispersion relation. The idea is that we assume a very small portion of hot electron population exists in the cold electron background, and assume the hot electron population is so small that it does not alter the cold plasma dispersion relation, but contributes an additional small damping rate. Mathematically, we separate the frequency ω into a real part and imaginary part: $\omega = \omega_r - i\omega_i$ where $\omega_i \ll \omega_r$, and correspondingly $\mathbf{k} = \mathbf{k}_r + i\mathbf{k}_i$ where $k_i \ll k_r$, and assume the real part $\omega_r, \mathbf{k}_r$ are solely described by the cold plasma dispersion relation, while the small hot electron population contributes to $\omega_i, \mathbf{k}_i$. Brinca [31] derived the following formula for the damping rate:

$$
\begin{aligned}
\chi &= -\frac{ck_i}{\omega} \\
&= \frac{1}{4\mu(2A\mu^2 - B)} \Bigg(\\
&\quad \frac{\mu^2 \sin^2\theta - P}{2(S-\mu^2)} \Gamma_1 \left(\left[(R-\mu^2) J_{m-1} + (L-\mu^2) J_{m+1} \right]^2 G_1 \right) \\
&\quad - 2 \left[(S - \mu^2\cos^2\theta)(S-\mu^2) - D^2 \right] \Lambda_1 (J_m G_2) \\
&\quad - 2\mu^2 \sin\theta\cos\theta \Gamma_1 \left(\left[(R-\mu^2) J_{m-1} + (L-\mu^2) J_{m+1} \right] G_2 \right) \Bigg),
\end{aligned}
\tag{2.9}
$$

where A, B, C, P, S, D, R and L are the Stix parameters introduced in Section 2.2.1, J_m is the the Bessel function of the first kind of order m with argument being $\frac{k_\perp v_\perp}{\Omega_e}$, and the operator Γ_1 and Λ_1 is defined as:

$$\begin{aligned}\Gamma_1(\cdot) &= \frac{2\pi^2 e^2}{\epsilon_0 m_e \omega k_\parallel} \sum_{m=-\infty}^{\infty} \int_0^\infty dv_\perp v_\perp^2 \int_{-\infty}^{\infty} dv_\parallel \delta(v_\parallel - v_\parallel^{res})(\cdot), \\ \Lambda_1(\cdot) &= \frac{2\pi^2 e^2}{\epsilon_0 m_e \omega k_\parallel} \sum_{m=-\infty}^{\infty} \int_0^\infty dv_\perp v_\perp \int_{-\infty}^{\infty} dv_\parallel v_\parallel \delta(v_\parallel - v_\parallel^{res})(\cdot),\end{aligned} \tag{2.10}$$

and functions G_1 and G_2 are defined as:

$$\begin{aligned}G_1 &= (1 - \frac{k_\parallel v_\parallel}{\omega})\frac{\partial f}{\partial v_\perp} + \frac{k_\parallel v_\perp}{\omega}\frac{\partial f}{\partial v_\parallel}, \\ G_2 &= J_m[(1 + \frac{m\Omega_e}{\omega})\frac{\partial f}{\partial v_\parallel} - m\frac{\Omega_e v_\parallel}{\omega v_\perp}\frac{\partial f}{\partial v_\perp}],\end{aligned} \tag{2.11}$$

where $v_\parallel^{res} = \frac{\omega + m\Omega_e}{k_\parallel}$ is the resonance velocity, and $f(v_\parallel, v_\perp)$ is the phase space density of the hot electrons in units of $cm^{-6}s^{-3}$. Following the method of [24], if we assume an isotropic distribution:

$$f(v_\parallel, v_\perp) = \frac{A_N}{(v_\parallel^2 + v_\perp^2)^q}, \tag{2.12}$$

where $f(v_\parallel, v_\perp)$ can be easily calculated from a measured electron flux $J(E)$ by fitting the flux as $J(E) = J_0 E^{-n}$. Observing that $J(E) = \frac{v^2}{m_e} f(v_\parallel, v_\perp)$, we can quickly derive

$$q = n + 1; A_N = 2J_0(\frac{2}{m_e})^{n-1}. \tag{2.13}$$

In the remaining sections we will use this method to derive Landau damping rate from spacecraft observed electron flux data.

2.2.3 Magnetic field and plasma density model

In the ray tracer we use a simple dipole magnetic field model throughout the dissertation. We use a modified diffusive equilibrium (DE) model for the cold electron density in ray tracing which is critical for guiding the ray trajectories, following Bortnik et al. [22]. The density model is described as:

$$N_e = N_b N_{de} N_{li} N_{pl} \tag{2.14}$$

Here, N_b is the reference density at geocentric distance R_b. The diffusive equilibrium term N_{de} is:

$$N_{de} = \left[\sum_{i=1}^{3} h_i \exp\left(-\frac{G}{H_i}\right)\right]^{1/2} \tag{2.15}$$

where $i = 1, 2, 3$ corresponds to H^+, He^+, and O^+, respectively. h_i is the ion composition at R_b, and the geopotential height G is

$$G = R_b\left(1 - \frac{R_b}{R}\right) \tag{2.16}$$

The scale height H_i is

$$H_i = \frac{T_{DE}}{M_i m_p g(R_b)}, \quad g(R_b) = g(R_E)\left(\frac{R_E}{R_b}\right)^2 \tag{2.17}$$

with M_i the ion mass normalized by proton mass m_p, and T_{DE} the base temperature in unit eV. The ionospheric shaping term N_{li} ensures the density drops below the ionosphere and peaks at its base:

$$N_{li} = \begin{cases} 1 - \exp\left(-\frac{(R-R_0)^2}{H^2}\right), & R \le R_0 \\ 0, & \text{otherwise} \end{cases} \tag{2.18}$$

where R_0 is the ionospheric base height, and H is its scale height. The plasmapause term N_{pl} models the sharp density gradient at the plasmapause:

$$N_{pl} = \begin{cases} \left[\exp\left(-\frac{(L-L_p)^2}{w^2}\right) + 1 - \exp\left(-\frac{(L-L_p)^2}{w^2}\right)\right] \\ \quad \cdot \left[\left(\frac{R_c}{R}\right)^a + \left(1 - \left(\frac{R_c}{R}\right)^a\right)\exp\left(-\frac{(R-R_c)^2}{H_s^2}\right)\right], & L \le L_p \\ 1, & \text{otherwise} \end{cases} \tag{2.19}$$

Here, L_p is the inner plasmapause boundary, w its half-width, R_c the matching point between inner and outer densities, a the outer falloff exponent, and H_s the outer scale height.

The DE model provides us a framework with free parameters (such as w, H_s, R_c, etc.) to construct various density model. We choose the Carpenter and Anderson (CA) model [35], which provides equatorial electron density as a function of L-shell and MLT, as a reference empirical model, and adjust the parameters in the DE model so that the equatorial density profile of the DE model fits the CA model (see example in Section 3.3).

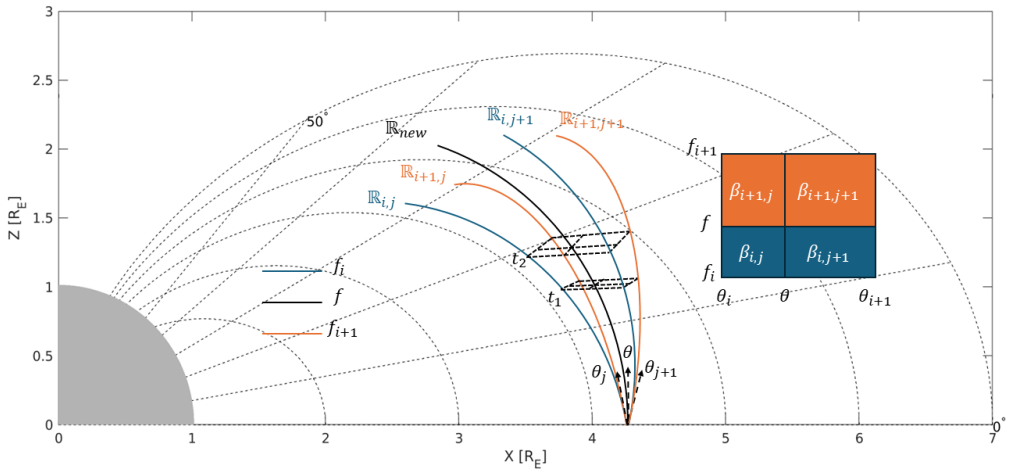

Figure 2.3: Sketch illustrating the ray interpolation method, showing how an untraced ray $\mathbb{R}_{new}$ is interpolated from four traced rays.

2.3 Calculating the distribution of wave properties

The purpose of this step is to record the wave information for those wave components propagating through a given target field line, in preparation for the pitch angle scattering calculation in the next step. The output of this step is a set of functions $\mathbb{W}(\lambda; f, t)$, where w can be various wave properties such as wave power (represented by the Poynting flux S_w), WNA, Stix functions like P, R, L, etc. (we can denote them as $\mathbb{W}[S_w], \mathbb{W}[\theta]$, etc.), as a function of f and t, recorded at EA locations at different latitude λ. In this step we first generate more rays using the traced rays so that the denser distribution of rays can better simulate the continuous wave distribution in reality. Then, using the obtained ray paths, we select the rays crossing the target field line and record their $\mathbb{W}(\lambda; f, t)$.

2.3.1 Ray interpolation method

The ray tracing initialization method described in Section 2.2.1 usually initializes several thousands rays, with $N_f \lesssim 100$ frequency components and $N_\theta \lesssim 100$ initial WNAs. Running more rays will result in excessive computational cost. However, several thousands rays is still highly discrete and is far from enough to be a good simulation of the realistic continuous wave field. Therefore, we have to find a method to generate much more ray paths using the already generated ray paths by the ray tracer.

Our method is to generate untraced rays by interpolating between the traced rays. Specifically, we trace $N_f \times N_\theta$ rays using ray tracing for frequencies $f_i, i = 1, 2, ...N_f$ and initial WNA $\theta_j, j = 1, 2, ...N_\theta$, and these rays is labeled as $\mathbb{R}_{i,j}(t)$, where $\mathbb{R}$ represents the ray properties such as location, power, WNA etc. (we can denote them as $\mathbb{R}[\mathbf{x}], \mathbb{R}[S_w], \mathbb{R}[\theta]$, etc.) at time t. To find a ray $\mathbb{R}_{new}$ with frequency f and initial WNA θ, we find the nearest two frequencies $f_i \leq f \leq f_{i+1}$ and two nearest WNAs $\theta_j \leq \theta \leq \theta_{j+1}$. Then $\mathbb{R}_{new}(t)$ can be linearly interpolated from $\mathbb{R}_{i,j}(t), \mathbb{R}_{i+1,j}(t), \mathbb{R}_{i,j+1}(t)$ and $\mathbb{R}_{i+1,j+1}(t)$ by:

$$\mathbb{R}_{new}(t) = \beta_{i,j}\mathbb{R}_{i,j}(t) + \beta_{i+1,j}\mathbb{R}_{i+1,j}(t) + \beta_{i,j+1}\mathbb{R}_{i,j+1}(t) + \beta_{i+1,j+1}\mathbb{R}_{i+1,j+1}(t), \tag{2.20}$$

where the four $\beta_{i,j}$ are the linear weight factor defined through the initial condition:

$$\begin{aligned} \beta_{i,j} &= \frac{(f - f_i)(\theta - \theta_j)}{(f_{i+1} - fi)(\theta_{j+1} - \theta_j)}, \beta_{i+1,j} = \frac{(f_{i+1} - f)(\theta - \theta_j)}{(f_{i+1} - fi)(\theta_{j+1} - \theta_j)}, \\ \beta_{i,j+1} &= \frac{(f - f_i)(\theta_{j+1} - \theta)}{(f_{i+1} - fi)(\theta_{j+1} - \theta_j)}, \beta_{i+1,j+1} = \frac{(f_{i+1} - f)(\theta_{j+1} - \theta)}{(f_{i+1} - fi)(\theta_{j+1} - \theta_j)}. \end{aligned} \tag{2.21}$$

The interpolation process is illustrated in Figure 2.3.

We usually interpolate $M_f \approx 200$ rays between each f_i and f_{i+1}, and $M_\theta \approx 200$ rays between each θ_i and θ_{i+1}. Therefore, after the interpolation we expand our ray number by $\times M_f M_\theta \sim \times 40,000$, from several thousands to around one million. We achieve a much better smooth, continuous coverage of ray paths with only very few extra computational resources via the ray interpolation method.

2.3.2 Generating the distribution of wave properties from ray tracing results

With the obtained one million rays, we now generate the wave information on the target field line $\mathbb{W}(\lambda; f, t)$. We divide the field line into small segment,s with each segment centered at latitude λ_i and intervals between λ_i being $\Delta\lambda$. We assign another small segment perpendicular to the target field line at each λ_i, and it is called an effective area (EA, also plotted in Figure 2.1 on the target field line). The EA has a width of ΔL_{EA}, which can be adjusted as needed. A larger ΔL_{EA} allows the EA to capture more rays so that the statistical error can be reduced, but the captured rays will be more far away from the target field line so that the rays are less representative, and vise versa for smaller ΔL_{EA}. We usually set $\Delta L_{EA} = 0.005$ to balance the number and quality of the captured rays.

The EAs are responsible for determining whether a ray propagates to the target field line near λ_i. If one ray $\mathbb{R}$ with frequency f crosses the λ_i's EA at time t_{cross}, the ray information will then be recorded into the $f - t$ spectrum at λ_i:

$$\begin{aligned} \mathbb{W}[S_w](\lambda_i; f, t_{cross}) &:+= \mathbb{R}[S_w](t_{cross}), \\ \mathbb{W}[other\,properties](\lambda_i; f, t_{cross}) &:+= \mathbb{R}[other\,properties](t_{cross}) \cdot \mathbb{R}[S_w](t_{cross}), \end{aligned} \tag{2.22}$$

where the wave power will be directly summed up, and other quantities such as WNA will be weighted by the wave power. After iterating over all rays with all crossing rays recorded, those other properties should be normalized by being divided by the total wave power:

$$\mathbb{W}[other\,properties](\lambda_i; f, t) :/= \mathbb{W}[S_w](\lambda_i; f, t). \tag{2.23}$$

This is equivalent to a weighted sum of these properties with their wave power serving as the weight.

After this step, a complete list of $\mathbb{W}(\lambda; f, t)$ for λ_is on the target field line is established.

2.4 Calculating the wave driven electron scattering

The purpose of this step is to calculate the $E-t$ spectrum of the scattered pitch angle at the both footpoints of the target field line, using the wave information $\mathbb{W}(\lambda; f, t)$ we obtained from Step 2. We start with the electron dynamic equation.

2.4.1 Integrating the scattered pitch angles due to chorus waves

The dynamic equation of the electron pitch angle α due to chorus waves is given by Bell [18]:

$$\frac{\mathrm{d}\alpha}{\mathrm{d}t} = -\frac{m_e\omega_{\tau m}^2}{k_\parallel p_\perp}\left(1+\frac{\cos^2\alpha}{m\frac{\Omega_e}{\omega}-1}\right)\sin\eta + \frac{p_\perp}{2\gamma m_e\Omega_e}\frac{\mathrm{d}\Omega_e}{\mathrm{d}s}, \tag{2.24}$$

where $\gamma = \frac{1}{\sqrt{1-\frac{v^2}{c^2}}}$ is the Lorentz factor, $p_\perp$ is the electron perpendicular momentum, η is the gyrophase of the electron, s is the field line length from the equator as a 1D curvature coordinate of the field line, and

$$\begin{gathered}
\omega_{\tau m}^2 = (-1)^{m-1}\omega_{\tau 0}^2[J_{m-1}(\beta) - \alpha_1 J_{m+1}(\beta) + \gamma\alpha_2 J_m(\beta)], \\
\beta = \frac{k_\perp p_\perp}{\gamma m_e\Omega_e}, \\
\omega_{\tau 0}^2 = \frac{\omega_1 k_\parallel p_\perp}{\gamma m_e}, \\
\omega_1 = \frac{e}{2m_e}(B_x^w + B_y^w);\ \omega_2 = \frac{e}{2m_e}(B_x^w - B_y^w), \\
\alpha_1 = \frac{\omega_2}{\omega_1};\ \alpha_2 = \frac{eE_z^w}{\omega_1 p_\perp},
\end{gathered} \tag{2.25}$$

where $\mathbf{E}^w$ and $\mathbf{B}^w$ are the chorus wave electric and magnetic fields, and the x, y, z coordinate is defined with $\hat{\mathbf{z}}$ aligned with $\mathbf{B}_0$, $\hat{\mathbf{x}}$ lying in the plane formed by $\mathbf{B}_0$ and $\mathbf{k}$, and $\hat{\mathbf{y}}$ completing the right handed Cartesian coordinates. Therefore, we need $\mathbf{E}^w$ and $\mathbf{B}^w$ components to integrate the dynamic equation 2.24. This can be inferred from the recorded wave Poynting flux $\mathbb{W}[S_w](\lambda; f, t)$ via cold plasma dispersion relation:

$$|B_y^w|^2 = \frac{2\mu_0\rho_2^2X^2\mu\cos\theta S_w}{c\sqrt{(\tan\theta - \rho_1\rho_2 X)^2 + (1+\rho_2^2X)^2}}, \tag{2.26}$$

where

$$
\begin{aligned}
X &= \frac{P}{P-\mu^2\sin^2\theta}, \\
\rho_1 = \frac{E_z^w}{E_y^w} &= \frac{(\mu^2-S)\mu^2\sin\theta\cos\theta}{D(\mu^2\sin^2\theta-P)}, \\
\rho_2 = \frac{E_x^w}{E_y^w} &= \frac{\mu^2-S}{D},
\end{aligned}
\tag{2.27}
$$

and the remaining components are given by:

$$
\begin{aligned}
E_x^w &= \frac{P-\mu^2\sin^2\theta}{P\mu\cos\theta}cB_y^w, \\
E_y^w &= \frac{D(P-\mu^2\sin^2\theta)}{P\mu\cos\theta(S-\mu^2)}cB_y^w, \\
E_z^w &= -\frac{\mu\sin\theta}{P}cB_y^w, \\
B_x^w &= -\frac{D(P-\mu^2\sin^2\theta)}{P(S-\mu^2)}B_y^w, \\
B_z^w &= \frac{D\sin\theta(P-\mu^2\sin^2\theta)}{P\cos\theta(S-\mu^2)}.
\end{aligned}
\tag{2.28}
$$

Using the equations above, given a $\mathbb{W}(\lambda_i)$ at a specific frequency f and time t, we obtain the expression for $\frac{\mathrm{d}\alpha}{\mathrm{d}t}$, and then it should be integrated over the small field line segment centered at λ_i:

$$
\Delta\alpha = \int_{t_1}^{t_2} \frac{\mathrm{d}\alpha}{\mathrm{d}t}dt, \tag{2.29}
$$

where t_1 and t_2 is the time when the electron travel to $\lambda = \lambda_i - \frac{\Delta\lambda}{2}$ and $\lambda = \lambda_i + \frac{\Delta\lambda}{2}$. We can change the integral variable to s for more convenient manipulation noting that $ds = v_\parallel dt$:

$$
\Delta\alpha = \frac{1}{v_\parallel}\int_{s_i-\frac{\Delta s}{2}}^{s_i+\frac{\Delta s}{2}} \frac{\mathrm{d}\alpha}{\mathrm{d}t}ds, \tag{2.30}
$$

where s_i is the s variable corresponding to latitude λ_i, and Δs is the length corresponding to $\Delta\lambda$. To conduct the integral, we note that Equation 2.24 can be expressed as

$$
\frac{\mathrm{d}\alpha}{\mathrm{d}t} = T_1\sin\eta + T_2, \tag{2.31}
$$

where

$$\begin{cases} T_1 = -\dfrac{m_e\omega_{\tau m}^2}{k_\parallel p_\perp}\left(1+\dfrac{\cos^2\alpha}{m\frac{\Omega_e}{\omega}-1}\right), \\ T_2 = \dfrac{1}{v_\parallel}\left(\dfrac{m\Omega_e}{\gamma}-\omega\right)-k_\parallel, \end{cases} \tag{2.32}$$

are slow varying within a small distance of Δs compared with gyrophase η, therefore can be considered as constant in Equation 2.30. Further, we note that the term T_2 represents the adiabatic motion of the electrons and does not involve the electron scattering process, so we can neglect this term and let the remaining T_1 part describe the scattering to the equatorial pitch angle α_{eq} where

$$\frac{\sin^2\alpha}{B(s)} = \frac{\sin^2\alpha_{eq}}{B(0)}, \tag{2.33}$$

and add the effect of T_2 term in the end by considering the field line contraction using Equation 2.33. Equation 2.30 can then be written as:

$$\Delta\alpha_{eq} = \frac{T_1}{v_\parallel}\int_{s_i-\frac{\Delta s}{2}}^{s_i+\frac{\Delta s}{2}} \sin\eta(s)ds. \tag{2.34}$$

We now derive the expression for $\eta(s)$, which is given also from the electron dynamic equation of [18]:

$$\frac{\mathrm{d}\eta}{\mathrm{d}t} = \frac{m\Omega_e}{\gamma} - \omega - k_\parallel v_\parallel, \tag{2.35}$$

We also substitute t into s:

$$\frac{\mathrm{d}\eta}{\mathrm{d}s} = \frac{1}{v_\parallel}\frac{\mathrm{d}\eta}{\mathrm{d}t} = \frac{1}{v_\parallel}\left(\frac{m\Omega_e}{\gamma}-\omega\right)-k_\parallel. \tag{2.36}$$

We linearize the integral by expanding Ω_e and $v_\parallel$ to first order around s_i, and after some algebra, we have

$$\frac{\mathrm{d}\eta}{\mathrm{d}s} = 2As + B, \tag{2.37}$$

where

$$\begin{cases} A = \dfrac{1}{2}\left(\dfrac{1}{v_\parallel^2}\dfrac{\mathrm{d}v_\parallel}{\mathrm{d}s}\left(\omega-\dfrac{m\Omega_e}{\gamma}\right)+\dfrac{m}{\gamma v_\parallel}\dfrac{\mathrm{d}\Omega_e}{\mathrm{d}s}\right), \\ B = \dfrac{p_\perp}{2\gamma m_e\Omega_e}\dfrac{\mathrm{d}\Omega_e}{\mathrm{d}s}, \end{cases} \tag{2.38}$$

Here A, B and T_1 should all take the value at s_i. The integral result is then

$$\eta(s) = A(s + \frac{B}{2A})^2 + \eta_0, \tag{2.39}$$

with η_0 being the initial gyrophase. Taking Equation 2.39 back into Equation 2.34 and after some derivation, we have:

$$\Delta\alpha_{eq}(\eta_0) = \frac{T_1}{v_\parallel}\sqrt{\frac{\pi}{2A}}(\cos\eta_0\Delta F_S + \sin\eta_0\Delta F_C), \tag{2.40}$$

where F_S and F_C are Fresnel integral defined as $F_S(x) = \int_0^x \sin\left(\frac{\pi}{2}t^2\right)dt$, $F_C(x) = \int_0^x \cos\left(\frac{\pi}{2}t^2\right)dt$, and ΔF_S and ΔF_C are defined as:

$$\begin{cases} \Delta F_S = F_S\left(\dfrac{B}{\sqrt{2\pi A}} + \sqrt{\dfrac{2A}{\pi}}\Delta s\right) - F_S\left(\dfrac{B}{\sqrt{2\pi A}}\right), \\ \Delta F_C = F_S\left(\dfrac{B}{\sqrt{2\pi A}} + \sqrt{\dfrac{2A}{\pi}}\Delta s\right) - F_C\left(\dfrac{B}{\sqrt{2\pi A}}\right). \end{cases} \tag{2.41}$$

Finally, Equation 2.40 only represents the α_{eq} scattered by chorus waves for one single electrons with initial gyrophase η_0. To account for the scattering effect of all electrons, we have to calculate the mean square value of $\Delta\alpha_{eq}$ which is cumulative according to quasi-linear theory:

$$< \Delta\alpha_{eq}^2 >= \frac{1}{2\pi}\int_0^{2\pi} \Delta\alpha_{eq}^2(\eta_0)d\eta_0. \tag{2.42}$$

Here we assume the electrons are gyrotropic also based on quasi-linear theory assumption. The final integrated result is:

$$< \Delta\alpha_{eq}^2 >= \frac{T_1}{2v_\parallel}\sqrt{\frac{\pi}{2A}}(\Delta F_S^2 + \Delta F_C^2). \tag{2.43}$$

2.4.2 Assigning $< \Delta\alpha_{eq}^2 >$ to $E - t$ bins

We have calculated the resultant $< \Delta\alpha_{eq}^2 >$ using Equation 2.43, which describes how much pitch angle scattering occurs for the electrons. We shall ask two more questions about the scattered electrons: what is their energy, and when will they be lost at the ionosphere after

the scattering? By addressing these two questions we can accurately distribute the $< \Delta\alpha_{eq}^2 >$ contributed by different waves into the correct bin in the $E - t$ spectrum of scattered pitch angle, thus obtaining the final product of this step, the $< \Delta\alpha_{eq}^2 > (E, t)$ spectrum for both footpoints.

The energy of the scattered electrons is relatively simple: it is the resonance energy. It can be easily derived from the resonance condition:

$$\omega - k_{\parallel} v_{\parallel} = m\frac{\Omega_e}{\gamma}. \tag{2.44}$$

Taking in the expression for γ:

$$\gamma = \frac{1}{\sqrt{1 - \frac{v^2}{c^2}}} = \frac{1}{\sqrt{1 - \frac{v_{\parallel}^2}{c^2 \cos^2 \alpha}}}, \tag{2.45}$$

where α is the pitch angle of the electron, we can simplify Equation 2.44 into a quadratic equation of $v_{\parallel}$, whose solution is:

$$v_{\parallel}^{res} = \frac{\pm\sqrt{\omega^2 k_{\parallel}^2 + [(m\Omega_e)^2 - \omega^2]\left[k_{\parallel}^2 + \left(\frac{m\Omega_e}{c\cos\alpha_{lc}}\right)^2\right]} - \omega k_{\parallel}}{k_{\parallel}^2 + \left(\frac{m\Omega_e}{c\cos\alpha_{lc}}\right)^2}. \tag{2.46}$$

Here the choice of $\pm$ sign is constrained by the requirement that $|\frac{v_{\parallel}^{res}}{\cos\alpha}| \leq c$. Specifically, for resonance mode $m > 0$, we choose counter-streaming solution with $+$ sign and for resonance mode $m \leq 0$, we choose co-streaming solution with $-$ sign. Also, we set $\alpha = \alpha_{lc}$, α_{lc} being the local loss cone angle, in Equation 2.46 because when calculating the precipitated flux, we assume that the electrons are scattered into the loss cone. Test runs have shown that the root mean square $\sqrt{< \Delta\alpha_{eq}^2 >}$ is usually much smaller than the loss cone angle, meaning that to be scattered into the loss cone, the trapped electrons have to be immediately close to the loss cone. Therefore, the meaningful scattered electrons producing precipitation have $\alpha \approx \alpha_{lc}$. After obtaining the $v_{\parallel}^{res}$ we can calculate the resonance energy of the scattered electrons by:

$$E_{res} = (\gamma_{res} - 1)m_e c^2 = \left(\frac{1}{\sqrt{1 - \frac{(v_{\parallel}^{res})^2}{c^2 \cos^2 \alpha_{lc}}}} - 1\right) m_e c^2. \tag{2.47}$$

The time when scattered electrons is lost into the ionosphere is delayed by the flight time τ_{flt} from interaction location λ_i to the ionosphere after it has resonated with waves at time t:

$$t_{lost} = t + \tau_{flt}. \tag{2.48}$$

The flight time τ_{flt} is given by $\tau_{flt} = \int \frac{\mathrm{d}s}{v_\parallel}$ where the elemental length of the field line $\mathrm{d}s$ can be derived from the dipole field line equation $r = LR_E \cos^2\lambda$:

$$\mathrm{d}s = \sqrt{\mathrm{d}r^2 + r^2 \mathrm{d}\lambda^2} = LR_E \sqrt{1 + 3\sin^2\lambda}\cos\lambda \mathrm{d}\lambda, \tag{2.49}$$

and $v_\parallel = v\cos\alpha$ noting that under adiabatic motion v is conserved and α follows Equation 2.33:

$$\begin{aligned} v_\parallel &= v\sqrt{1 - \sin^2\alpha} \\ &= v\sqrt{1 - \sin^2\alpha_{eq}\frac{B(\lambda)}{B(0)}} \\ &= v\sqrt{1 - \sin^2\alpha_{eq}\frac{\sqrt{1+3\sin^2\lambda}}{\cos^6\lambda}}, \end{aligned} \tag{2.50}$$

where the ratio $\frac{B(\lambda)}{B(0)}$ is derived from the dipole field model. Therefore, the flight time from λ_i to northern and southern hemisphere footpoints are:

$$\begin{cases} \tau_{flt}^{(N)} = \dfrac{LR_E}{v}\displaystyle\int_{\sin\lambda_i}^{\sin\lambda_{inv}} \sqrt{\frac{1+3x^2}{1 - \sin^2\alpha_{eq}\frac{\sqrt{1+3x^2}}{(1-x^2)^3}}}dx, \\ \tau_{flt}^{(S)} = \dfrac{LR_E}{v}\displaystyle\int_{-\sin\lambda_{inv}}^{\sin\lambda_i} \sqrt{\frac{1+3x^2}{1 - \sin^2\alpha_{eq}\frac{\sqrt{1+3x^2}}{(1-x^2)^3}}}dx, \end{cases} \tag{2.51}$$

where we substitute λ into $x = \sin\lambda$, and λ_{inv} is the latitude of the footpoint, also called the invariant latitude of a field line. Equation 2.51 does not have simple analytical solution and is integrated numerically.

To sum up for Step 3, for each $f-t$ bin in each $\mathbb{W}(\lambda_i)$, we can calculate the mean square of the scattered electron pitch angle $< \Delta\alpha_{eq}^2 >$, the energy of the scattered electrons E_{res}, and the time precipitated electrons arrive at ionosphere and are lost $t_{lost} = t + \tau_{flt}$, then we add $< \Delta\alpha_{eq}^2 >$ into the $E_{res} - t_{lost}$ bin in the $< \Delta\alpha_{eq}^2 > (E, t)$ spectrum of the northern

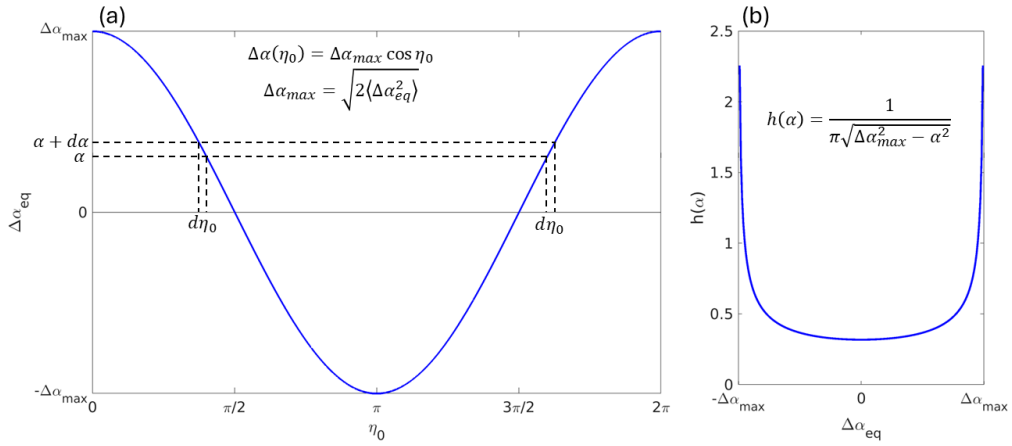

Figure 2.4: Panel (a) shows the function $\Delta\alpha_{eq}(\eta_0)$, and Panel (b) shows the resultant probability function $h(\alpha)$.

or southern hemisphere footpoint, depending on whether the precipitated electrons are co-streaming or counter-streaming. After iterating through all data in $\mathbb{W}(\lambda_i; f, t)$ we obtained from Step 2, we establish the complete $< \Delta\alpha_{eq}^2 > (E, t)$ spectrum for both hemisphere footpoints.

2.5 Calculating the precipitated flux

The purpose of this step is to convert the previously obtained $< \Delta\alpha_{eq}^2 > (E, t)$ spectrum for both hemisphere footpoints into the final result, the precipitated flux spectrum $J_{precip}(E, t)$ for both hemisphere footpoints. This requires additional knowledge of the trapped flux, as $< \Delta\alpha_{eq}^2 >$ describes the amount of electron scattered from trapped state into loss cone. The detailed process is as followed.

Combining Equation 2.40 and Equation 2.43 yields the following expression for $\Delta\alpha_{eq}(\eta_0)$:

$$\Delta\alpha_{eq}(\eta_0) = \Delta\alpha_{max}\cos\eta_0, \tag{2.52}$$

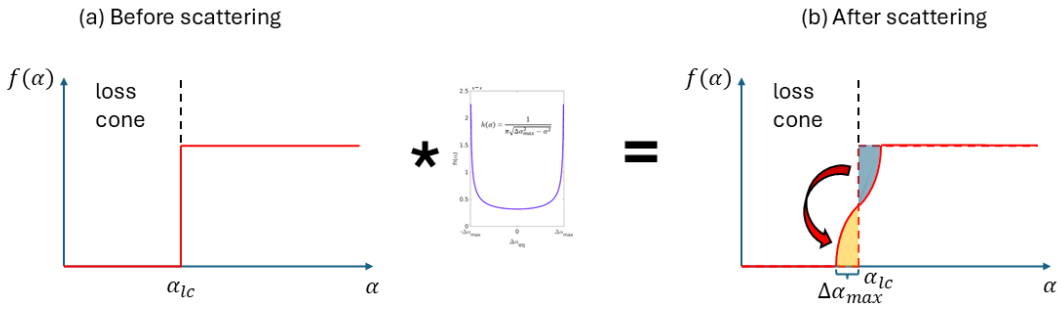

Figure 2.5: Illustration of how trapped flux is converted into precipitated flux. Panel (a) shows the trapped PSD in a square loss cone form, and Panel (b) is the scattered PSD derived from the convolution between the trapped PSD and $h(\alpha)$.

where $\Delta\alpha_{max} = \sqrt{2 < \Delta\alpha_{eq}^2 >}$, and η_0 can be redefined to avoid any extra constant within the cosine function in Equation 2.52. Assuming the electron phase space density is gyrotropic (independent on η_0) following quasi-linear theory, we ask the question that what is the probability for an electron to be scattered by $\Delta\alpha_{eq} = \alpha$, or equivalently, what is the probability density function of the electron scattered pitch angle $h(\alpha)$?

The derivation of $h(\alpha)$ is shown in Figure 2.4. Panel (a) shows the $\Delta\alpha_{eq}(\eta_0)$ function. Based on the gyrotropic assumption, the probability of electron being scattered by $\alpha < \Delta\alpha_{eq} < \alpha + \mathrm{d}\alpha$ is

$$h(\alpha)d\alpha = \frac{2|\mathrm{d}\eta_0|}{2\pi}, \tag{2.53}$$

where the factor 2 in the numerator reflects the two different η_0 values that map to the same α value, as indicated in Panel (a) of Figure 2.4. From Equation 2.52 we can easily derive the function $\left|\frac{\mathrm{d}\eta_0}{\mathrm{d}\alpha}\right|$, therefore obtain the expression for the probability density function $h(\alpha)$:

$$h(\alpha) = \frac{1}{\pi\sqrt{\Delta\alpha_{max}^2 - \alpha^2}}. \tag{2.54}$$

We now discuss how we convert trapped flux data into precipitated flux using $h(\alpha)$.

Consider the trapped electron phase space density $f(\mathbf{r}, E, \alpha) = f_0 g(\alpha)$, where f_0 is function of location and energy. We assume a simple square loss cone model , which means the loss cone is empty and outside the loss cone the phase space density is independent of pitch angle α:

$$g(\alpha) = \begin{cases} 0, \alpha < \alpha_{lc}, \\ 1, \alpha \geq \alpha_{lc}, \end{cases} \tag{2.55}$$

as shown in Panel (a) of Figure 2.5. The phase space density after scattering $\tilde{f}(\alpha) = f_0 \tilde{g}(\alpha)$ can be divided into three part. For pitch angle $\alpha \leq \alpha_{lc} - \Delta\alpha_{max}$, the phase space density remains 0 because the scattered electrons with lowest possible pitch angle comes from the trapped electrons with lowest pitch angle (the loss cone angle α_{lc}) scattered by the largest possible pitch angle change ($\Delta\alpha_{max}$), which leads to $\alpha_{min} = \alpha_{lc} - \Delta\alpha_{max}$. The second part is for pitch angle $\alpha \geq \alpha_{lc} - \Delta\alpha_{max}$, where the phase space density remains unchanged. We note that $h(\alpha)$ is symmetric for both $\alpha > 0$ and $\alpha < 0$ and $f(\alpha)$ is constant for $\alpha > \alpha_{lc}$, therefore for any pitch angle $\alpha \geq \alpha_{lc} + \Delta\alpha_{max}$, accompanied by a small portion of electron $f(\alpha)h(\delta\alpha)\mathrm{d}\alpha$ scattered and lost from α into $\alpha + \delta\alpha$ is always the same amount of electrons $f(\alpha + \delta\alpha)h(-\delta\alpha)\mathrm{d}\alpha = f(\alpha)h(\delta\alpha)\mathrm{d}\alpha$ scattered from $\alpha + \delta\alpha$ and refilling back into α. The final part is for pitch angle $\alpha_{lc} - \Delta\alpha_{max} < \alpha < \alpha_{lc} + \Delta\alpha_{max}$, where the phase space density alters. This can be calculated via the following formula:

$$\tilde{g}(\alpha) = \int_{-\Delta\alpha_{max}}^{\Delta\alpha_{max}} g(\alpha - \beta)h(\beta)\mathrm{d}\beta. \tag{2.56}$$

This equation can be understood as summing up electron scattered to pitch angle α contributed by all possible source $\alpha - \beta$. This equation has an analytical solution, which is listed in the below final results for the scattered $\tilde{g}$:

$$\tilde{g}(\alpha) = \begin{cases} 0, \alpha \leq \alpha_{lc} - \Delta\alpha_{max}, \\ \dfrac{1}{\pi}\left[\dfrac{\pi}{2} + \arcsin\left(\dfrac{\alpha - \alpha_{lc}}{\Delta\alpha_{max}}\right)\right], \alpha_{lc} - \Delta\alpha_{max} < \alpha < \alpha_{lc} + \Delta\alpha_{max}, \\ 1, \alpha \geq \alpha_{lc} + \Delta\alpha_{max}. \end{cases} \tag{2.57}$$

Finally, we observe that the relation between flux and phase space density is a linear relationship of $J = \frac{v^2}{m_e} f$, and v^2 is a constant during the pitch angle scattering process, therefore we can also write the flux as $J(\mathbf{r}, E, \alpha) = J_\perp(\mathbf{r}, E) g(\alpha)$ with $g(\alpha)$ being identical to the one in phase space density and $J_\perp = \frac{v^2}{m_e} f_0$, and the pitch angle distribution $g(\alpha)$ also follows the rule described by Equation 2.57 after the scattering. Therefore, the flux distribution after scattering is

$$\tilde{J}(\mathbf{r}, E, \alpha) = J_\perp(\mathbf{r}, E) \tilde{g}(\alpha). \tag{2.58}$$

The total precipitated flux J_{precip} (in unit $cm^{-2}s^{-1}keV^{-1}$) can then be derived by integrating $\tilde{J}$ over the loss cone:

$$\begin{aligned} J_{precip} &= \frac{1}{\sin^2 \alpha_{lc}} \int_0^{\alpha_{lc}} \tilde{J} \cos\alpha 2\pi \sin\alpha \mathrm{d}\alpha \\ &= \frac{\pi}{\sin^2 \alpha_{lc}} \int_0^{\alpha_{lc}} \tilde{J} \sin(2\alpha) \mathrm{d}\alpha, \end{aligned} \tag{2.59}$$

where the $\cos\alpha$ accounts for the area adjustment perpendicular to $\mathbf{B}_0$, $2\pi \sin\alpha \mathrm{d}\alpha$ is the small solid angle element, and since the integral is completely conducted in equatorial values, to convert the precipitated flux into the ionospheric precipitation location, we add an extra $\frac{1}{\sin^2 \alpha_{lc}}$ to account for the field line contraction, thus mapping the equatorial value of precipitated flux into the ionospheric area. Further, if we want the precipitated flux in units $cm^{-2}s^{-1}sr^{-1}keV^{-1}$, we just divide an extra loss cone solid angle at the ionosphere of 2π in Equation 2.59.

We apply the method above to each bin in the $< \Delta\alpha_{eq}^2 > (E, t)$ spectrum we obtained in Step 3, and then we derive the final product of the CIPP code, the $E - t$ spectrum of precipitated flux $J_{precip}(E, t)$ at both footpoints of a given target field line.

CHAPTER 3

Spatiotemporal characteristics of a single chorus driven microburst

3.1 Introduction

This chapter will present an event-based modeling of microbursts induced by a single chorus wave element using the CIPP code we introduced in the previous chapter. We will demonstrate the CIPP code's capability of providing detailed information of the microburst's dependence on energy, time and location. We will also reveal the connection between propagation effect of chorus waves and the spatiotemporal characteristics of the relativistic microburst through the analysis of our modeling results. By utilizing this powerful tool we will be able to investigate an important spatiotemporal characteristic, the spatial scale size of the microburst, which has been an open question due to the difficulties in measuring through in situ observations.

Despite of the numerous observations of microbursts through various LEO satellites for example SAMPEX [91, 92], the observational methods are limited by the in situ nature of the instruments. Because of the very short duration of around $0.1s$ [132] of each microburst peak, the distance traveled by the LEO satellite is so short ($\approx 790m$ estimated from the first orbital velocity $v_1 = 7.9km/s$) that it should be considered stationary during each observed microburst event. Therefore, the measured precipitation flux variation should be understood as a temporal signature, and obtaining the spatial signatures of the microburst directly from a single spacecraft is extremely difficult.

Very few observational works have attempted to study the scale size of microburst due to the difficulties we mentioned above. Crew et al. [43] uses two spatially separated FIREBIRD II CubeSat to conduct simultaneous observation of the same microburst, and thus estimated the scale size to be $\approx 10km$. Shumko et al. [135] also uses FIREBIRD II with the same method but estimates a slightly larger scale size of $29 \pm 1km$ in the latitudinal direction and $51 \pm 11km$ in the longitudinal direction. Blake et al. [19] analyze the condition to observe a bouncing microburst based on the sampling period of SAMPEX spacecraft and give a lower limit of a few tens of km for the scale size. Shumko et al. [134] apply probabilistic tools to analyze the AeroCube-6 CubeSat data and derive the most probable range of scale size to be $12 - 47km$. In general, limited special cases yields a rough range of microburst scale size of several tens km.

The scale size of microbursts near the Earth's surface is important for both understanding the impact of microbursts on the atmosphere and estimating the total energetic electron loss from the outer radiation belt. Therefore, our ability of modeling the spatial signature of microburst is valuable and important in better understanding the radiation belt dynamics. In this work, we will model the microburst induced by an observed chorus event using our CIPP code, and the modeling results will reveal physical insights in the generation mechanism of chorus wave driven microburst. We will also focus on analyzing the microburst spatiotemporal characteristic to address the scientific question of microburst scale size.

3.2 Model setup

We initialize a chorus waves at equatorial source region located at $L = 4.75, MLT = 9$. The chorus waves have frequency components between $0.1 - 0.5 f_{ce,eq}$, where $f_{ce,eq}$is the electron gyrofrequency at the equator, and the wave power follows a sinusoidal distribution. We also assume the chorus waves are mostly field aligned by following a Gaussian WNA distribution with a characteristic width $\Delta\theta = 15°$, which confines the wave power to low WNA range

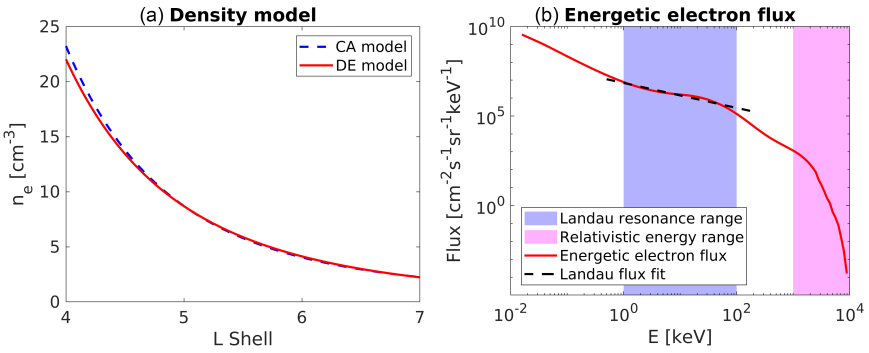

Figure 3.1: The environmental model setup. (a) Electron density model. The blue dashed line is the Carpenter-Anderson model, which is chosen as our statistical ground truth. The red solid line is the Diffusive Equilibrium model, which is used in our ray tracing code. (b) Energetic electron flux model. This is taken from RBSP's statistical results. The blue shaded area represents the rough Landau resonance energy range $(1-100keV)$, and the black dashed line shows the linear fit of this part which serves as the Landau damping calculation input. The red shaded part represents the relativistic electron flux.

consistent with statistical works [38, 84]:

$$b_{w0}^2 = B_{w0}^2 \frac{8.463}{f_{ce,eq}} \sin\left(\pi \frac{f - 0.1 f_{ce,eq}}{0.4 f_{ce,eq}}\right) \exp\left(-\frac{\theta^2}{\Delta\theta^2}\right), \tag{3.1}$$

where b_{w0}^2 is the power density function for initial wave power, $\frac{8.463}{f_{ce,eq}}$ is a normalization factor, and B_{w0} is the total wave amplitude and is set to a typical value of $\approx 80pT$ [88]. We will assume a perfect point source for the chorus wave source region, and as we will show later, even a point source can lead to a finite sized microburst, therefore revealing that the chorus wave propagation effect is the main controller of the microburst spatial characteristics.

The environmental model required for ray tracing is shown in Figure 3.1. Panel (a) shows the electron density model at $MLT = 9$. We use the empirical model of Carpenter and Anderson [35] as the reference density model (CA model), and change the parameters controlling the Diffusive Equilibrium model (DE model) used in our code so that the DE model will be as close to the reference CA model as possible. Panel (b) shows the statistical results of the energetic electron flux at $L = 4.75, MLT = 9$ by RBSP. The blue shaded

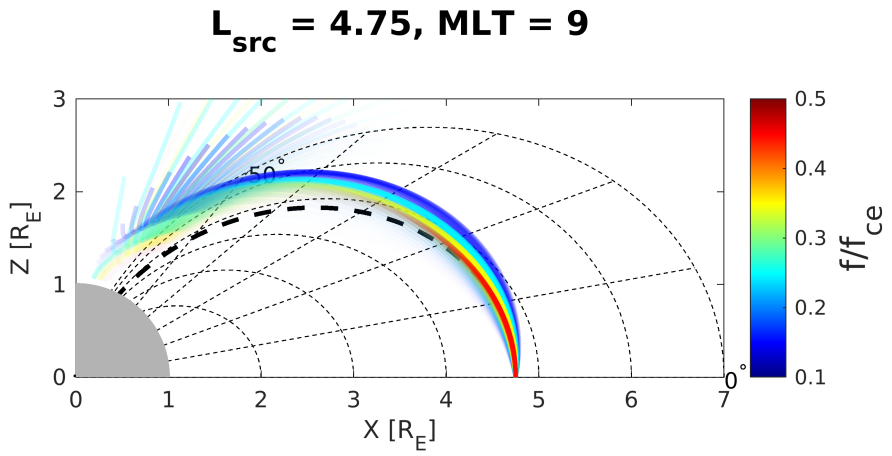

Figure 3.2: Ray paths of different frequencies for all modeled runs. Different frequencies are marked by different colors as shown by the color bar in the top right corner. The transparency of the rays indicates the ray power.

area represents the rough Landau resonance energy range $(1 - 100keV)$, within which the flux data will be used for Landau damping calculation. This is done following the linear fit method of [24], and the linear fit results are marked with the black dashed line. The red shaded part represents the equatorially trapped relativistic electron flux, which will be used as the seed electron when doing the scattering calculation.

3.3 Ray tracing simulation analysis

3.3.1 Ray paths

Figure 3.2 shows the ray trajectories for different frequencies, marked by the color bar on the right. The rays with the same frequency have different trajectories because their initial WNAs are different. The ray path transparency is set to be $\frac{b_w^2}{b_{w0}^2}$, where b_w^2 is the power density function at the ray's current location. Thus the rays fade out as they propagate away from the source region representing rays continually experiencing Landau damping. Several points that would be important to the discussion later should be made from these

results.

First, even though the chorus wave source region is assumed to be a single point here, the waves are still able to cover a wide range of L-shells, which produces a spatial distribution of precipitation flux on the ground. This is because there are different frequency modes and different initial WNAs in the chorus wave element, therefore their propagation behavior will also be different. Another interesting point is that although the wave trajectories diverge to L-shells both lower and higher than $L = 4.75$, most wave power actually propagates to higher L-shells. Some final minor points about the ray tracing result are that chorus waves with higher frequency tend to experience heavier damping according to the Landau damping calculation based on the observed electron distribution (therefore fade out quicker within shorter distance) and have more converged ray trajectories. This frequency dependence may indicate lower frequency chorus waves produce a microburst with higher flux and larger scale size but this trend needs further investigation to confirm.

3.3.2 Resonance energies

To understand where the relativistic electrons are scattered to produce relativistic microbursts, we calculate the resonance energy of chorus waves along their ray paths. The resonance condition is given by

$$\omega - k_{\parallel} v_{\parallel} = m \frac{\Omega_e}{\gamma}, \tag{3.2}$$

where ω and $k_{\parallel}$ are the angular frequency and parallel wave number, $v_{\parallel}, \Omega_e$ and γ are the parallel velocity, unsigned gyrofrequency and relativistic Lorentz factor of the resonant electron, and m is the order of resonance which takes the value of any integer. The value of m determines the characteristic of the resonance. For $m > 0$, the resonance is counter-streaming, and for $m \leq 0$, the resonance is co-streaming. The most important resonance types are those with smallest $|m|$, which are cyclotron resonance ($m = 1$), anomalous cyclotron resonance

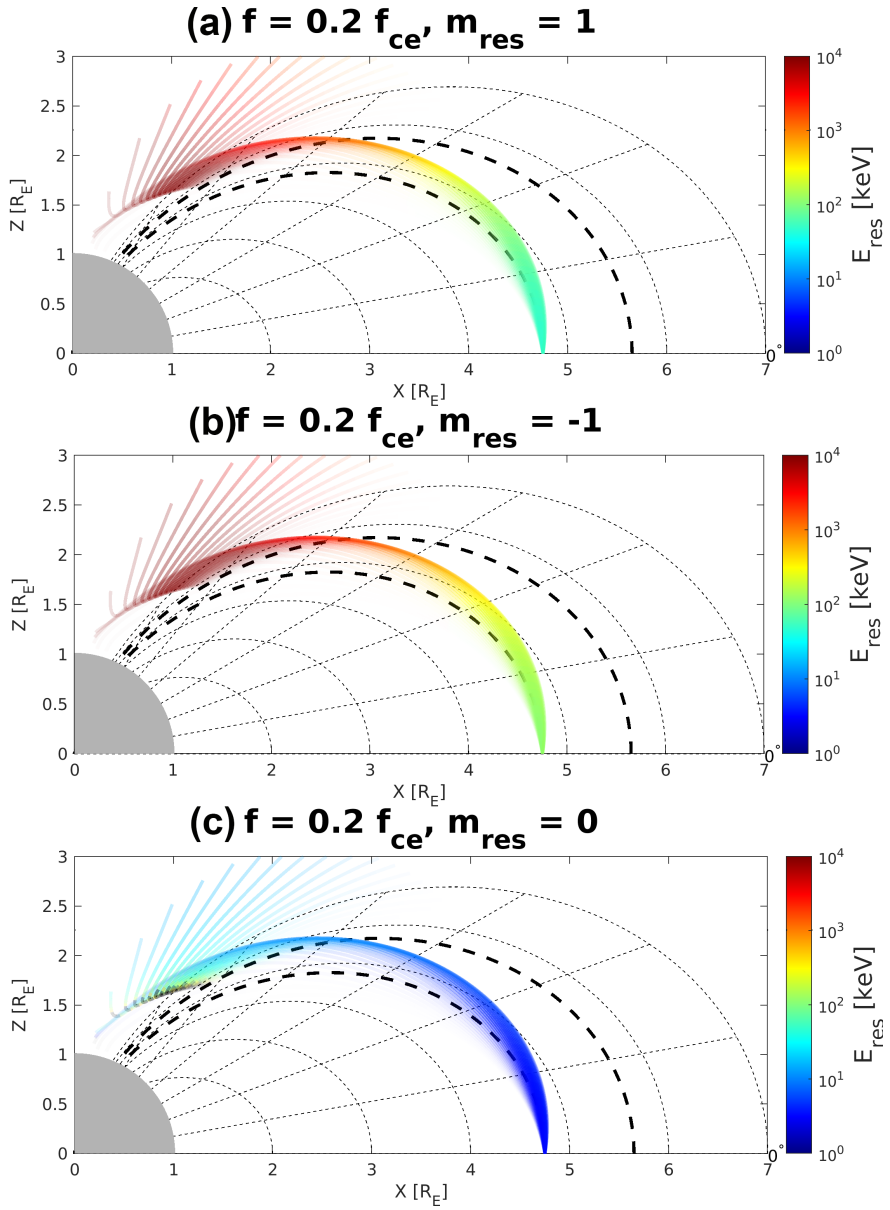

Figure 3.3: Resonance energy along ray paths. The three panels are for resonance energy through different resonance types (cyclotron, anomalous cyclotron and Landau resonance). The resonance energy is color coded as indicated by the color bar in the top right corner. The transparency of the rays indicates the ray power. The thick black dashed lines indicate the field line of $L = 4.75$ and 5.65, whose precipitation flux E-t spectrum is shown in Figure 3.4 and 3.5.

($m = -1$) and Landau resonance ($m = 0$). The resonance energy E_{res} is determined by

$$E_{res} = (\gamma - 1)m_e c^2, \tag{3.3}$$

where m_e is the mass of electron and c is the speed of light. γ is determined from Equation 3.2 noticing that $\gamma = 1/\sqrt{1 - \frac{v_\parallel^2}{c^2 \cos^2(\alpha)}}$, where α is the pitch angle of the electron. Thus E_{res} can be expressed as a function of $\omega, k_\parallel, \Omega_e, \alpha$ and m.

Figure 3.3 shows the resonance energy along the ray paths. We calculate the resonance energy for rays with $f = 0.2 f_{ce,eq}$ by the normal cyclotron resonance, anomalous cyclotron resonance and Landau resonance. The transparency of the ray paths represents the ray power, and the resonance energy is color coded according to the color bar on the right.

From Figure 3.3 we see that the relativistic electron microburst is only generated due to the cyclotron and anomalous cyclotron resonance. Landau resonance is almost unable to scatter electrons with energies $> 1MeV$ into the loss cone. Furthermore, even for cyclotron and anomalous cyclotron resonances, scattering the MeV electrons is only possible after chorus waves propagate to latitudes higher than 25°. Near the equatorial source region, the chorus waves can only scatter electrons with energy up to several hundred keV. In other words, relativistic electron microbursts are produced at high latitudes through cyclotron or anomalous cyclotron resonance. Ray tracing results shows that such resonances almost always occur at a higher L shell relative to the causative chorus wave source region.

3.4 Precipitation flux E-t spectrum on a single field line

Before examining the spatial distribution of the relativistic microburst over multiple L-shells, we first focus on the precipitation flux signature on both the L-shell of the wave source $L = 4.75$ and at a higher L-shell $L = 5.65$. Figure 3.4 shows the precipitation flux spectra seen at both the northern and southern foot points of these two field lines. The x-axis is the time span of 2 seconds, where $t = 0$ is the time the chorus waves are launched from the source location, and the y-axis is the energy of precipitated electrons.

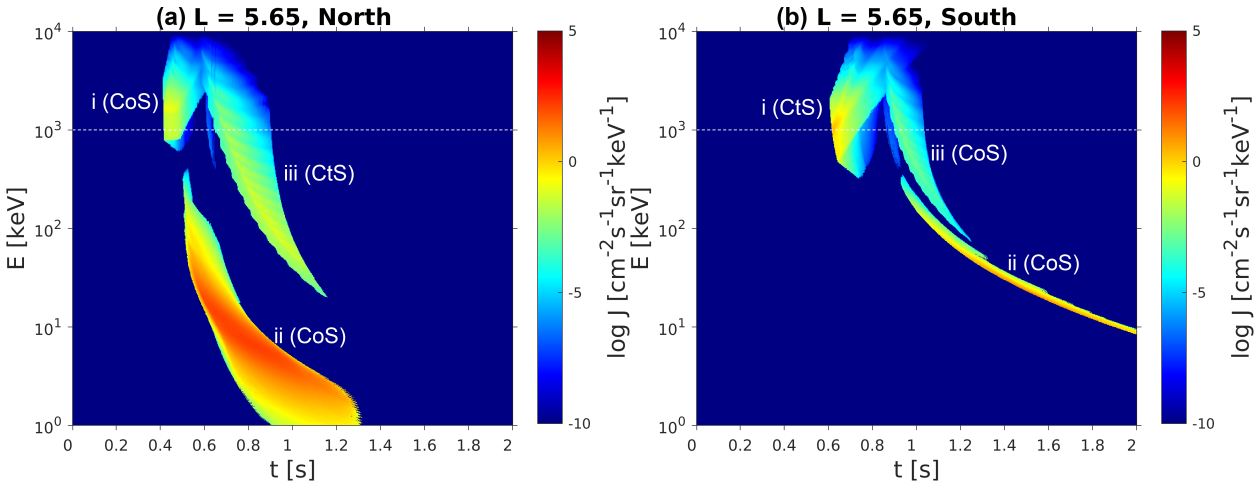

Figure 3.4: Energy-time spectrum of (a) northern and (b) southern hemisphere precipitation flux on the field line at $L = 5.65$. The white dashed line marks $1MeV$ energy. Several numbers are added to indicate different parts of the precipitation signature spectra, with notations "CoS" representing the co-streaming nature and "CtS" representing counter-streaming nature of the precipitation.

We mainly focus on the field line at $L = 5.65$, because Figure 3.2 and 3.3 indicate relativistic precipitation should mainly occur on a higher L-shell than the chorus wave source region $L = 4.75$. The spectra seen on northern and southern hemisphere are Figure 3.4 (a) and (b), respectively. We address a very important point that all the precipitations occurring on this field line are due to chorus waves that have propagated to high latitudes and turned oblique, as indicated in Figure 3.2. Clear relativistic precipitation near $1MeV$ energies (white horizontal dashed line) is observed in both hemispheres (feature labelled (i) in both panels). Because the waves propagate northward, the precipitated electrons in the southern hemisphere are counter-streaming with the waves (marked with "CtS"), and therefore are scattered due to first order cyclotron resonance with chorus waves, whilst the precipitated electrons on northern hemisphere are co-streaming (marked with "CoS") and scatter due to anomalous cyclotron resonance. The precipitation flux in the southern hemisphere is several times higher than the northern hemisphere, as would be expected since cyclotron resonance

is stronger than anomalous cyclotron resonance. The duration of part (i) is about 0.2 second, which is a typical timescale for a microburst.

A much weaker precipitation signature also around the $1MeV$ energy range and lagging behind part (i) by about 0.2 second (feature labelled (ii) in both panels) is observed on both hemispheres. These parts are induced by the magnetospherically reflected, equatorward traveling chorus waves as can be observed in Figure 3.3. Those waves are already highly damped after travelling to a very high latitude and experiencing a magnetospheric reflection, therefore the induced precipitation flux is also much weaker. Part (ii) is 1 to 2 orders of magnitude weaker than part (i), which suggests their contribution is negligible for overall radiation belt loss and may not generally be reflected in microburst observations.

Apart from the relativistic precipitation parts, there is also a very significant sub-relativistic $(1 - 100keV)$ precipitation signature in the northern hemisphere (feature (iii) in panel (a)). Considering the energy range and the co-streaming nature of this part of electrons, this feature of the precipitation is due to Landau resonance with the chorus waves. This is consistent with recent studies showing that Landau resonance with oblique chorus waves can induce intense sub-relativistic microburst precipitation [13]. Note that such strong sub-relativistic precipitation is not seen in the southern hemisphere because of the co-streaming nature of Landau resonance, which, in this case would only show up in the northern hemisphere, whereas the southern hemisphere will only exhibit the energetic electron precipitation portion. This may explain why microbursts near $1MeV$ and $150keV$ are not always correlated (Blake et al. [19], Figure 10). There exists, however, a part of the sub-relativistic precipitation in the southern hemisphere (part (iii) in panel (b)), but the flux is 4 orders of magnitude weaker than part (iii) in panel (a) because this part of precipitation is induced by Landau resonance with the magnetospherically reflected, highly damped chorus waves (the co-streaming condition is satisfied because the propagation direction reverses after bouncing).

The overall features of the spectra for the source region $L = 4.75$ (Figure 3.5 (c) and (d) for northern and southern hemisphere footpoint, respectively) are the same as discussed

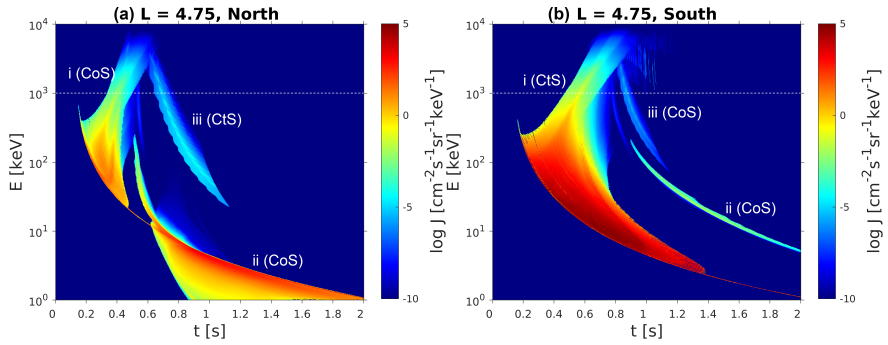

Figure 3.5: Energy-time spectrum of (a) northern and (b) southern hemisphere precipitation flux on the field line at $L = 4.75$. The white dashed line marks $1MeV$ energy. Several numbers are added to indicate different parts of the precipitation signature spectra, with notations "CoS" representing the co-streaming nature and "CtS" representing counter-streaming nature of the precipitation.

earlier for $L = 5.65$. The corresponding features are also labeled i, ii and iii in the plot. The major difference is the energy range. On the wave source field line, electrons resonate with quasi-parallel chorus waves near the equatorial source region, therefore the energy of electrons scattered by normal/anomalous cyclotron resonance is mainly in 10s-100s keV range (we remind readers there is anomalous cyclotron resonance in the source region because we introduce a spread in the WNA distribution). Their contribution to the relativistic microburst above $1MeV$ is limited to a weak high-energy tail of the spectrum, which is consistent with recent observation studies [133, 72], and the spectrum feature is also consistent with recent modeling works [107]. In contrast, the minimum resonance energy with oblique chorus waves on $L = 5.65$ is as high as several keV, therefore their contribution to relativistic microburst is significant even though the waves experience damping after travelling to higher latitudes.

3.5 Spatiotemporal distribution of precipitation flux

A precipitation $E-t$ spectrum such as the one shown in Figure 4 provides detailed temporal information about the precipitation along a single field line, or equivalently, temporal precipitation information at only two single points on the ground (which are the two foot points of the field line in each hemisphere). By integrating the precipitation flux of one field line above $1MeV$ (the white dashed lines in Figure 4), we can obtain the temporal variation of the total relativistic precipitation flux $J(t;\lambda_{inv})$ for one ionosphere location with the corresponding invariant latitude λ_{inv}. In this work, we calculate the precipitation flux signatures for 82 field lines whose invariant latitudes are evenly spaced between 62.1° and 66.1°, thus constructing a complete spatiotemporal distribution $J(t;\lambda_{inv})$ of the relativistic precipitation induced by a single chorus wave element.

The results are shown in panels (a)-(f) of Figures 3.6. The panels on the left column are for precipitation occurring in the northern hemisphere, and panels on the right column are for southern hemisphere. The first row is the precipitation spatiotemporal distribution. The y-axis is the total relativistic precipitation flux, and the x-axis is the location represented both by the invariant latitude λ_{inv} and the L-shell of the field line. Curves with different colors are the precipitation flux spatial distributions at different times, shown color coded by the color bar at the top right, with the chorus wave element launched from the equatorial source region defined as t=0. The vertical black dashed line in each panel marks the invariant latitude of the chorus wave source region.

Several properties can be observed and understood from these precipitation flux spatiotemporal distributions. First, it is seen that the relativistic electron microburst was successfully reproduced in each panel, with the flux profile taking the form of a single peak that grows and decays within $\approx 0.2s$, consistent with the typical time duration of a microburst [63, 150]. The microburst occurs poleward of the foot point of the chorus wave source region (marked by the vertical black dashed line in Panel (a) and (d)), and the microburst peak

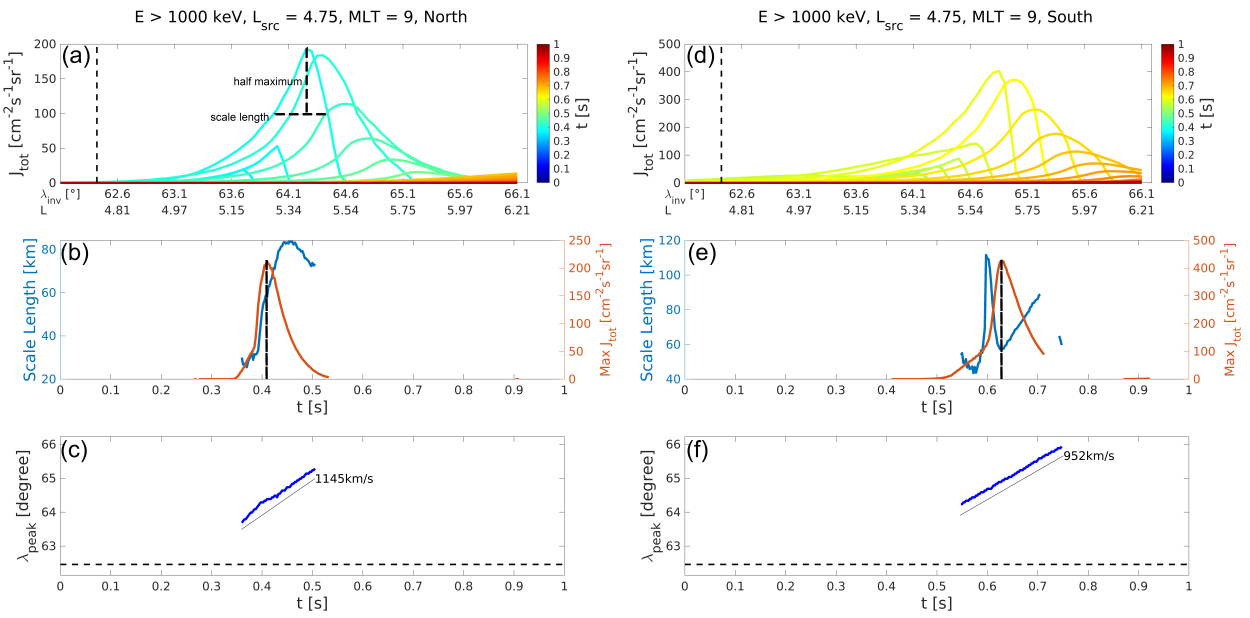

Figure 3.6: Relativistic $> 1MeV$ Microburst precipitation flux evolution on the ground surface as a function of latitude and time for (a) northern and (d) southern hemisphere. The black dashed vertical line marks the location of wave source L shell of 6. An illustration of how the scale length is defined is shown in (a). (b) and (e) show the time evolution of instantaneous maximum flux and scale length for northern and southern hemisphere, respectively. The red lines are the instantaneous maximum fluxes corresponding to the y axis on the right, and the blue lines are the scale lengths corresponding to the y axis on the left. (c) and (f) show the time evolution of the location of instantaneous peak fluxes of northern and southern hemisphere, respectively, with reference lines of different velocities. The black dashed horizontal line marks the location of wave source L shell of 6.

keeps moving poleward throughout the entire duration of the event. Panels (c) and (f) of Figures 3.6 show the latitude of the maximum precipitated flux as a function of time. We see that the peak of the microburst keeps moving poleward, and the ground velocity estimated by $R_E \frac{\mathrm{d}\lambda_{inv}}{\mathrm{d}t}$ is $\approx 1000 km/s$. This is a consequence of the chorus wave propagation effect, namely that the chorus wave power propagates to higher L-shells, as we discussed in Sections 3.3. The microburst in the southern hemisphere occurs later than those in the northern hemisphere because the chorus waves propagate only northward. As a result, the wave-particle interactions occur in the northern hemisphere, and thus more flight distance is required for electrons to travel from the interaction location to southern hemisphere foot point than northern hemisphere resulting in a longer delay to the onset of the precipitation signature. However, the precipitation flux in the southern hemisphere is stronger than the northern hemisphere because the counter-streaming cyclotron resonance (which results in precipitation occurring in the southern hemisphere) leads to more efficient pitch angle scattering than the co-streaming anomalous cyclotron resonance.

To describe the spatial scale size of the microburst, we define the scale size as the full width at half maximum (FWHM) of the precipitation flux spatial profile, as illustrated in Figure 3.6(a). The results are plotted in the blue curves in panel (b) and (e), corresponding to the left y-axis. We see that the relativistic microburst scale size in the southern hemisphere varies between 40 and $100 km$, and the scale size in the northern hemisphere varies between 20 and $80 km$. This suggests that the co-streaming microbursts have a smaller scale size than the counter-streaming, cyclotron-resonance-induced microburst. Despite the wide range of scale sizes, the typical scale size of microbursts that occurs when they are strongest, is usually small. For example, when the integrated flux in the southern hemisphere reaches its maximum value at $0.62 s$ (marked by the vertical dashed black line in Figure 3.6(e)), the simultaneous scale size is at a minimum value of $\approx 60 km$. For the northern hemisphere, the scale size at maximum flux is also $\approx 60 km$, as inferred from Figure 3.6(b).

3.6 Discussion and Summary

The scale size values of $\approx 60km$ agree well with previous observations. This not only gives us confidence in our modeling results, but also reveals some deeper physical insights. It's important to keep in mind that the scale size we obtain should be understood as a minimum possible value due to the modeling setting up in this work. We neglect the spatial extent of chorus wave packet on the equator and simplify it as a point source, and we neglect the chirping rate of the chorus wave element and assume all waves with different frequencies are launched simultaneously at $t = 0$. This means that the chorus wave source is shrunk on both spatial and temporal extent to its minimum possible value, therefore we expect the obtained scale size to be smaller than what it is in reality. Nevertheless, our event-based modeling yields a very reasonable scale size consistent with previous observations, which implies that the spatial and temporal extent of the chorus wave source might be a second order factor and the scale size of the precipitation is mainly due to the wave spreading during their propagation.

This finding provides an entirely new view than the traditional assumption that the relativistic microburst should be in conjunction with equatorial chorus waves. Specifically, two new understanding is revealed from this work. Previously we assume that the scale size of the microburst is related to the scale length of chorus wave elements at the equatorial (for example, Shumko et al. [135, 134]; Crew et al. [43]). In these works, the measured microburst scale size on the ground is mapped to the magnetic equator and compared with the chorus wave correlation length, which is claimed to be evidence that chorus waves are one possible source of microbursts. However, as we mention in the previous paragraph, it is the propagation effects of chorus waves that are the primary factor controlling the microburst scale size instead of the chorus wave element size, therefore allowing a point-sourced chorus wave element to produce a finite-sized microburst. As we mentioned in Section 3.3, the trajectories of chorus waves can diverge and cover a wide range of L-shell if

there are multiple frequency modes and initial WNAs in the chorus element, even if the source is a point. It is this L-shell coverage that constructs the spatial distribution of microburst flux on the ground. Another traditional view that is challenged by this work is that relativistic microburst should be in conjunction with the equatorial chorus waves [135, 134, 43], while our modeling indicate that the microburst is displaced poleward from the source L-shell, and exhibits a very high poleward-moving speed. Our analysis shows that this is because chorus waves needs to propagate to higher latitudes to reach the relativistic resonance energy, and in the unducted mode the chorus waves also propagate to higher L-shells as it propagate away from the equator, which maps to higher latitude on the ionosphere. In contrast, the resonance energy analysis shows that relativistic resonance energy near the source region is impossible. Therefore, such conjunction is possible only if there are mechanisms that constrain the chorus wave propagation to be field aligned, for example a density duct. We present one such case in Chapter 6. This may also raise an alarm for future conjugation observation studies of microbursts suggesting that other than a rigorous field line conjugation, a low-Earth-orbit spacecraft poleward of the equatorial spacecraft might also bring new insights.

CHAPTER 4

Global distribution of the characteristics of chorus driven microbursts

4.1 Introduction

In this chapter, following the single event modeling workflow we established in the previous chapter, we conduct simulations under different wave and plasma conditions at different L-shells and MLTs, thus attempting to construct a global distribution of the spatial characteristics of chorus wave induced relativistic microbursts. Recently there have been some statistical works focusing on the relativistic microburst features [47, 46, 132]. Douma et al. [47, 46] comprehensively analyze the occurrence rate and amplitude of relativistic microburst, but do not involve the spatiotemporal characteristics. The recent work of Shumko et al. [132], however, provides a very interesting statistical results on the global distribution of the duration of relativistic microburst. One interesting results revealed from this work is that the duration of relativistic microburst is similar in the dawn and night sectors ($\approx 80ms$), but significantly larger in the noon sector ($\approx 150ms$). Shumko et al. provide a hypothesis for this trend in MLT that it might be related to the chorus wave chirping rate asymmetry over MLT but without further investigation. This is the first clear evidence that microbursts possess different temporal feature on the noon sector than on the dawn and night sectors. However, no study has been done to investigate the global distribution of the spatial features. The study on the microburst scale size has been limited to a few case studies [43, 135, 134, 19].

This work will fill the gap in our understanding on the global distribution of the spatial characteristics of relativistic microburst. We have demonstrated that utilizing our code, we can obtain the microburst features given the information of chorus wave and plasma conditions. A natural extension is that we can use the statistic-based wave and plasma condition at different locations in the magnetosphere as model input, thus modeling the microburst features at different locations which yields a global distribution of microburst scale size. Better understanding the global distribution of the relativistic microburst spatial characteristics is not only an important open question that has not been answered, but also an essential middle-step for our ultimate goal of estimating the role microburst plays in the global relativistic electron loss. Moreover, this work can also provides a theoretical comparison for recent statistical works on relativistic microburst of Shumko et al. [132]. This chapter will be devoted to achieve this goal.

4.2 The finite sized chorus wave source region

In the single event modeling in previous chapter, we assumed a point source for chorus waves to address that it is the propagation effect that mainly controls the scale size of microburst instead of the source region size. From this chapter, however, we shall include the finite chorus wave source region size into consideration, therefore we can better simulate the realistic physical processes. To take the finite size of chorus wave source region into consideration, we use the fact that the size of chorus wave source region is usually only several hundred kilometers or $< 0.1R_E$ ($R_E = 6370km$ is the Earth radius), which is much smaller than the L-shell range covered by the ray paths (see the ray tracing results in Figure 3.2 for example). We also assume that the ray paths of two rays are almost parallel to each other if their equatorial source points are close enough. In other words, if their equatorial source points are separated by $d \ll R_E$, then one of the ray paths can be well approximated by another which is displaced by d. This assumption is valid because we expect the ray

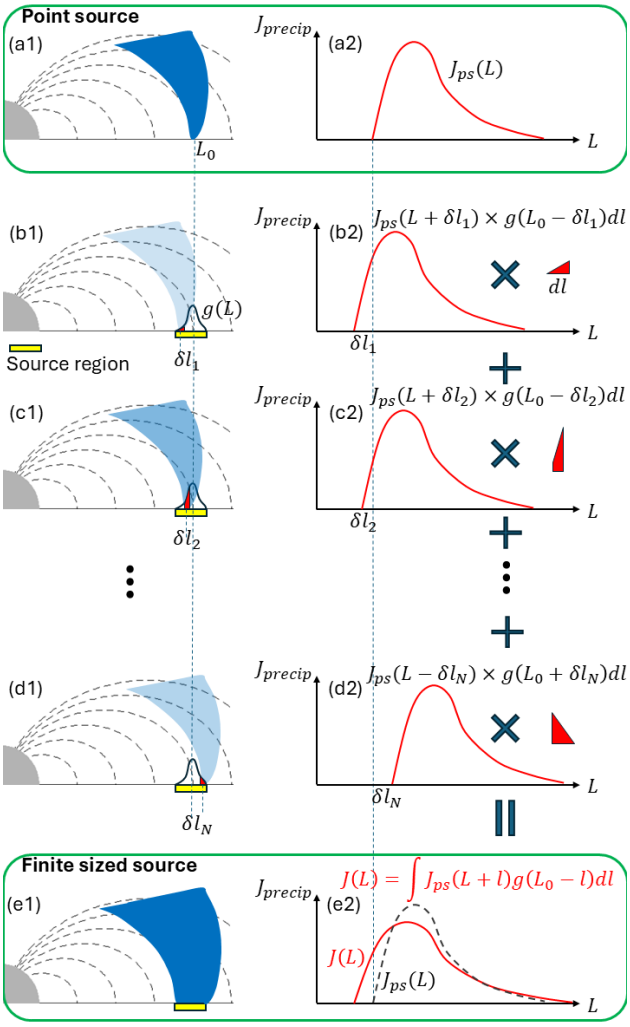

Figure 4.1: An intuitive graphic explanation of the convolution method that calculate the precipitation flux spatial distribution induced by a finite sized source region from those by a point source and the power density function of source region. Panels on the left show the ray paths, and Panels on the right show the precipitation flux spatial distribution. Panel (a) is the original point source case, and Panels (b)-(d) show how we decompose the finite sized source region to many small point source, and how the precipitation flux distribution is derived for each cases. Panel (e) shows how to add all decomposed cases up to derive the finite sized case.

paths in a smooth magnetosphere to be smooth and continuous. Therefore, if we have the precipitation flux distribution on different field lines ($J_{ps}(L)$) that is calculated from a point source whose L-shell is L_0, and the normalized wave power density function ($g(L)$ which satisfies $\int g(L)dL = 1$) over a small radial range of source region around L_0, we can directly calculate the precipitation flux distribution $J(L)$ considering the finite sized source region via a convolution:

$$J(L) = \int J_{ps}(L + l)g(L_0 - l)\mathrm{d}l \tag{4.1}$$

An intuitive grapgic explanation of the convolution method Equation 4.1 is given in Figure 4.1. Panel (a1) shows the ray paths originated from a point source at $L = L_0$, and Panel (a2) shows the corresponding precipitation flux distribution $J_{ps}(L)$ at one certain moment. The small yellow region in the rest panels represents the finite sized source region, which is characterized by a normalized power density function $g(L)$ shown in Panel (b1). Panels (b)-(d) shows how we can decompose the finite sized source region to many small point-like regions which are displaced from L_0 by δl_i, and how the resultant precipitation flux distribution is displaced by the same amount δl_i based on the assumption we discussed above, meanwhile linearly correlated with the corresponding wave power portion $g(L_0 - \delta l_i)dl$. Summing up the contributions from all point-like regions yields the precipitation flux distribution $J(L)$ for a finite sized source region, which turns out to be a convolution between $J_{ps}(L)$ and $g(L)$.

This simple convolution method can help us extend our results from the point source case to the finite size source region case. When we choose the power density function $g(L) = \delta(L - L_0)$, Equation 4.1 will reduce to the point source case $J(L) = J_{ps}(L)$. In this work, we assume the wave power distribution at the equatorial source region is a Gaussian function peaked at L_0 with a width given by ΔL:

$$g(L) = \frac{1}{\Delta L\sqrt{2\pi}} exp(-\frac{(L - L_0)^2}{\Delta L^2}) \tag{4.2}$$

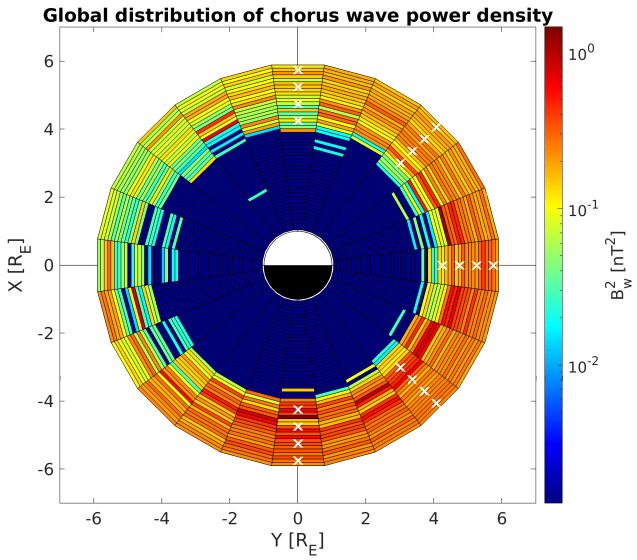

Figure 4.2: L-MLT distribution of chorus wave power density based on RBSP statistical results. The white crosses are the modelled chorus wave source points.

so Equation 4.1 becomes

$$J(L) = \frac{1}{\Delta L\sqrt{2\pi}} \int J_{ps}(L+l)exp(-\frac{l^2}{\Delta L^2})\mathrm{d}l \tag{4.3}$$

We adopt a chorus source size of $500km$ according to Agapitov et al. [2], and use twice of the standard variation (ΔL) of the Gaussian distribution as the scale length, thus setting the value of $\Delta L = 250km$.

4.3 Statistical models

To investigate the global distribution characteristics of the relativistic microburst spatial scale size, we separately run the simulation at 5 different MLTs (0, 3, 6, 9 and 12) and 4 different L shells (4.25, 4.75, 5.25 and 5.75) giving 20 different locations. These 20 locations are marked in Figure 4.2 by white crosses, in which the contours are the statistical results of lower band chorus wave power density near the magnetic equator during disturbed times, first presented by Ma et al. [96]. From Figure 4.2 we see that the chosen L shells cover

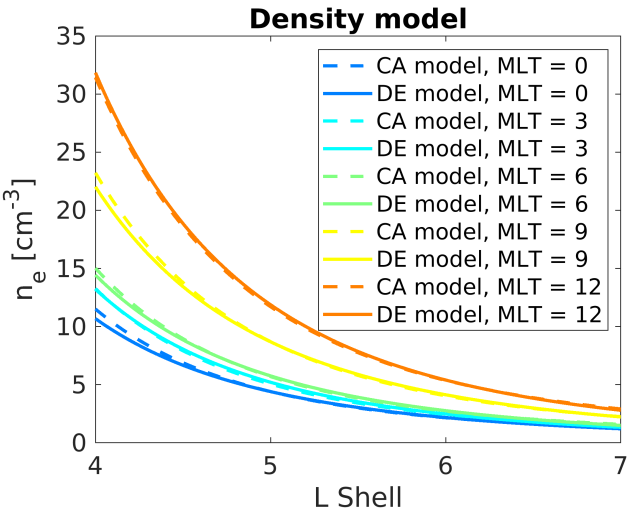

Figure 4.3: Equatorial density model. The dashed lines are the Carpenter-Anderson model, and the solid lines are the diffusive equilibrium model. Different colors are for different MLTs.

the most important L-shells where lower band chorus waves occur. Meanwhile, the MLT values (0, 3, 6, 9 and 12) are chosen to represent the 3 sectors (midnight, dawn and noon) where lower band chorus waves typically occur. These 20 locations reveal the general L-MLT distribution of relativistic microburst characteristics and spatial scale sizes.

Figure 4.3 shows the density models we use. 5 DE models are adopted for the simulation of the meridional plane density distribution for the 5 MLTs. The solid lines are the DE models for the 5 MLTs that are used in the ray tracing, and the dashed lines are the CA models for each MLT. We can see that our DE model fit agrees well with the CA model, especially for $L > 5$ where the ray paths are mostly located in this study. We use a dipole magnetic field model in ray tracing.

Both the Landau damping calculation and the conversion of the scattered pitch angle into a precipitation flux need an energetic electron flux spectrum, as we described in previous chapters. Here we use the statistical result based on the data from Ma et al. [96] to find the electron energy spectrum for the 5 different MLTs, which is shown in Figure 4.4. As done in

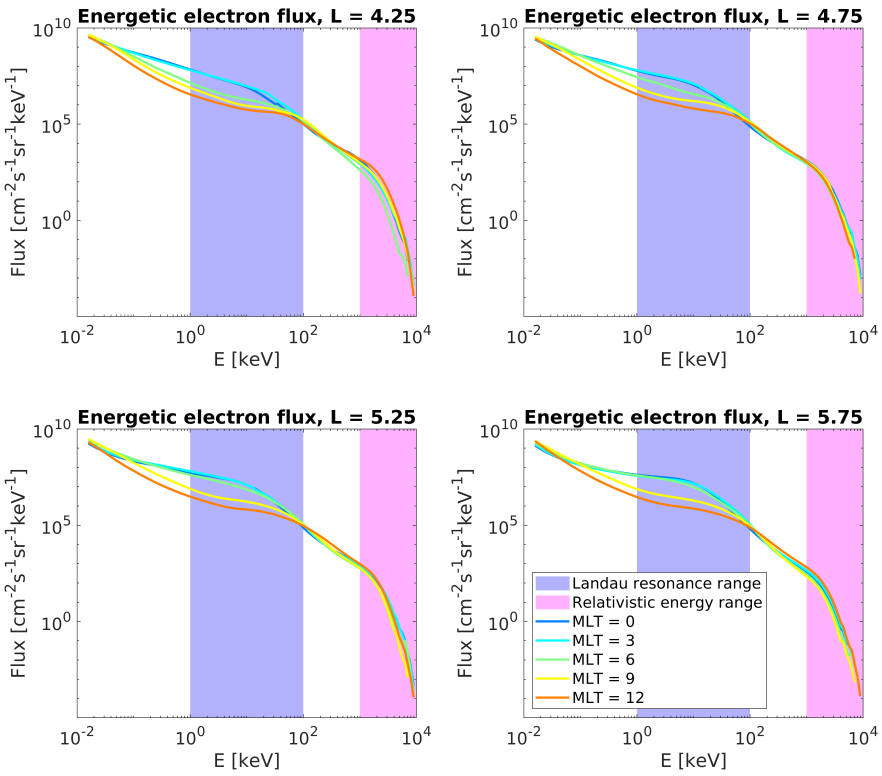

Figure 4.4: Energetic electron flux models at different locations from global statistical results by RBSP. Panels (a)-(d) are for locations at different L-shells, and in each panel, curves with different colors are for different MLTs. The blue shaded area represents the rough Landau resonance energy range $(1 - 100keV)$, and the black dashed line shows the linear fit of this part which serves as the Landau damping calculation input. The red shaded part represents the relativistic electron flux.

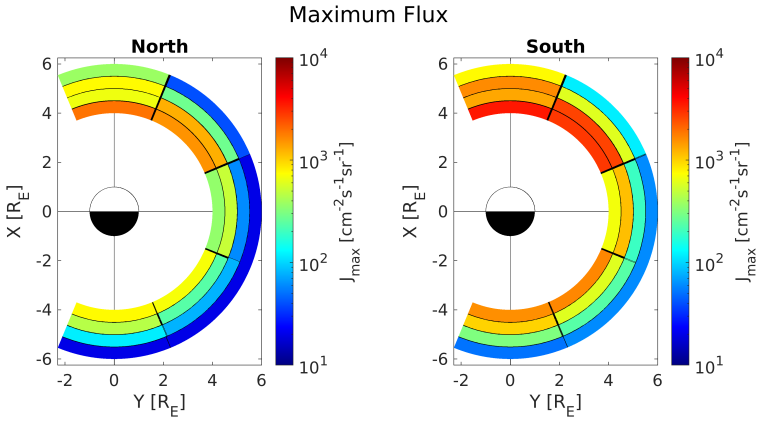

Figure 4.5: The maximum total precipitation flux in each run. The centers of bins in each panel represent the locations of the chorus wave source point. Color coded is the maximum total precipitation flux as indicated by the color bar.

Ma et al. [96], the trapped electron flux data are selected only when the chorus waves are observed to obtain the statistical electron flux distribution. These flux spectra are used as the equatorial trapped fluxes in the precipitation flux calculation. Following Kang et al. [69] and Bortnik et al. [25], the flux PA distribution is assumed to be empty inside the loss cone and isotropic outside as the first-order assumption. The flux spectra in the energy range of $1 < E < 100keV$ (which is the major Landau resonance range, see for example Figures 3.3) are converted into an electron velocity distribution using the method of Bortnik et al. [24], which is further used for Landau damping calculation.

We assume the initial chorus wave power at each source point follows a sine-shaped frequency distribution between $0.1 - 0.5 f_{ce}$, and a Gaussian WNA distribution, the same as Equation 3.1 we used in the previous chapter.

4.4 Modeling results and discussion

Before presenting the global distribution of microburst scale size from our modeling results, we first quickly recap how we define the microburst scale size. For each run, we can derive

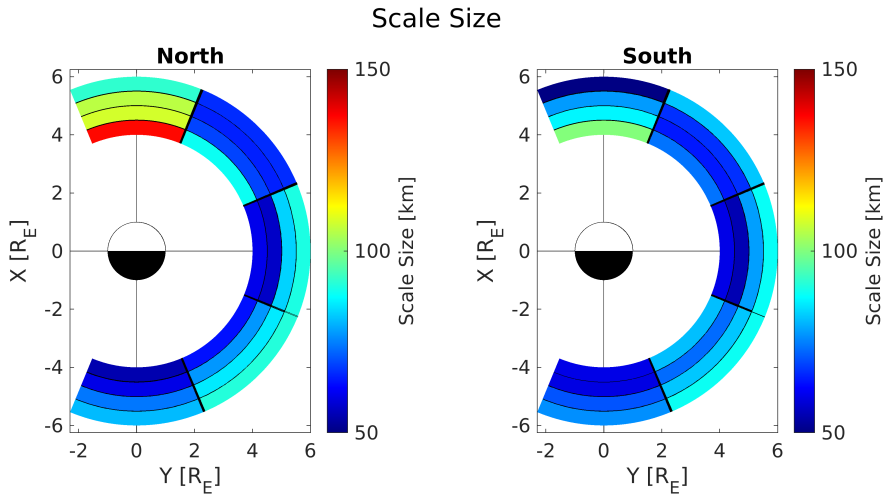

Figure 4.6: The microburst scale sizes in each run. The centers of bins in each panel represent the locations of the chorus wave source point. Color coded is the scale size as indicated by the color bar.

the spatiotemporal distribution of relativistic precipitation flux $J_{tot}(\lambda_{inv}, t)$, as shown in Figure 3.6 (a) and (d). We derive two important variables from $J_{tot}(\lambda_{inv}, t)$: the maximum flux at each moment $J_{tot,max}(t) = \max(J_{tot}(\lambda_{inv}, t)\big|_t)$, and the scale size at each moment $s(t) = FWHM(J_{tot}(\lambda_{inv}, t)\big|_t)$, where $FWHM(\cdot)$ represent the Full Width at Half Maximum of the input function. An example of these two quantities are shown in Figure 3.6 (b) and (e). In this study, we wish to derive a most representative value of $J_{tot,max}(t)$ and $s(t)$ for the 20 runs, thus obtaining a global distribution of these two quantities. We use $\max(J_{tot,max}(t))$, the peak value of $J_{tot,max}(t)$ (equivalently, the maximum precipitation flux during the whole event), as the representative precipitation flux value, and use the scale size corresponding to $\max(J_{tot,max}(t))$ as the representative scale size of this event, as marked by the black vertical dashed line in Figure 3.6 (b) and (e).

The global distributions of the maximum total relativistic precipitation flux and the scale length are shown in Figure 4.5 and 4.6, respectively. Note that the centers of bins in each panel represent the locations of chorus wave source point instead of the microburst. As we analyzed in previous chapter, relativistic microburst occurs at higher L-shells of chorus

wave source. From Figure 4.5 and 4.6 we can clearly see that the noon sector has distinct characteristics than the dawn and midnight sectors. The dawn and midnight sectors ($0 < MLT < 9$) have little differences in terms of maximum fluxes and scale sizes and share the same trends that the precipitation flux is stronger in the inner L shells and the scale size is larger in the outer L shells. However, for the noon sector (≈ 12), the maximum flux is overall stronger than the dawn and midnight sectors, and the scale size is also significantly larger compared with the other two sectors.

The unique features of the noon sector might be due to the low Landau damping rate. From Figure 4.4 we can see that for every L-shell, the noon sector ($MLT = 12$) has the lowest flux value in Landau resonance energy range, which means it has the lowest Landau damping rate. Therefore, it can account for the stronger maximum flux at noon sector than dawn and midnight sectors because the chorus waves power remains higher due to low damping rate. The reason why the low Landau damping rate also leads to larger scale size might be more subtle. As we mentioned in previous chapter, the chorus waves will diverge to a wider L-shell range as they propagate to higher latitudes (see Figure 3.2). Therefore, a lower damping rate means that chorus wave power can propagate further to higher latitudes, thus covering a wider L-shell range where the scattering of relativistic electrons occurs. This can be clearly seen from Figure 4.7. The ray power at $MLT = 12$ can be maintained to higher L-shells compared with $MLT = 9$, and thus the precipitation shown in Panels (b2) has much wider L-shell range than (a2).

In this chapter, we include the impact of finite sized chorus wave source region. We introduce a convolution method to deal with it. We find that the scale size under finite sized source region is almost the same but slightly larger compared with the point source case we show in the previous chapter, just as we illustrated in Figure 4.1 (e2). This result again address the important insight that the scale size of microbursts is primarily controlled by the propagation effect of chorus waves rather than the equatorial source region size.

One chorus wave feature that is not included in the present work is the chirping of

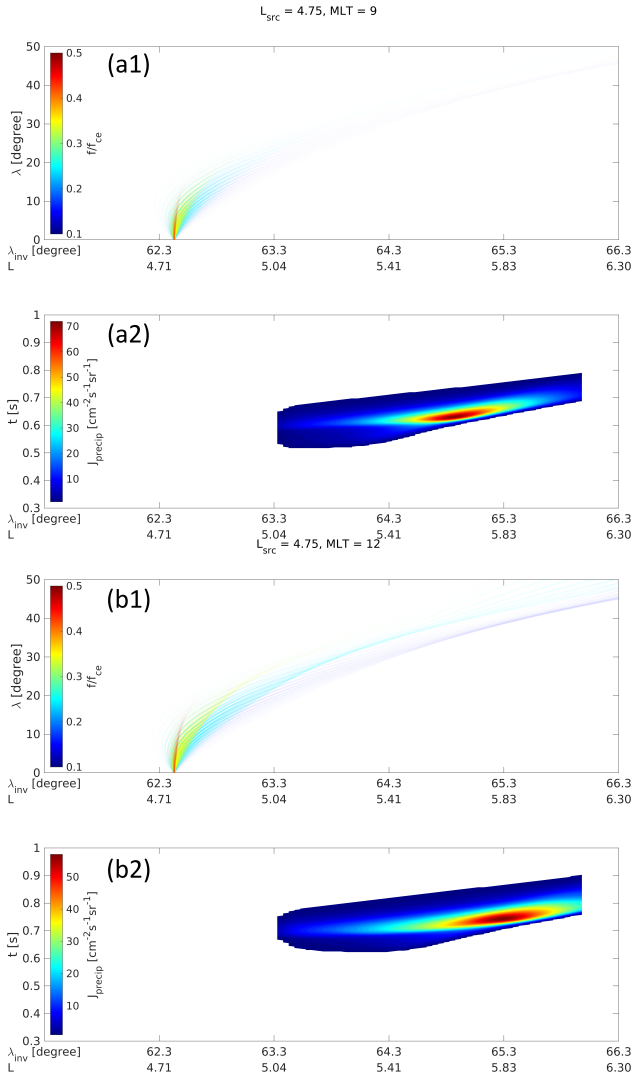

Figure 4.7: Comparing the precipitation signature of noon and dawn sector. Panels (a1) and (a2) are for case $L_{src} = 4.75, MLT = 9$, and Panels (b1) and (b2) are for case $L_{src} = 4.75, MLT = 12$. Panels (a1) and (b1) are the ray paths with the same format as Figure 3.2 but in the $L(\lambda_{inv}) - \lambda$ coordinates. Panels (a2) and (b2) are the spatiotemporal distribution of the relativistic precipitation flux, with x axis being the spatial coordinate $L(\lambda_{inv})$ and y axis being time.

the chorus wave element which would tend to increase the duration of the precipitation signature to some extent. In the ray tracing modeling, all rays with different frequencies are launched simultaneously, thus in effect assuming an infinitely large chirping rate in order to focus only on the wave propagation and electron time-of-flight aspects. Test runs show that finite chirping rates do have some impacts on the spatial precipitation flux distribution [106, 120, 40, 37] but that it is a less important factor compared with other factors, especially the effects of MLT. This might be due to the fact that the scale size is a spatial characteristic and will be less affected by the temporal characteristics like the chirping rate. Therefore, we neglect the wave frequency chirping in this work to focus solely on propagation effects, eliminate one variable from consideration to reduce the complexity of the analysis, and leave the chirping rate effects for future detailed study.

Both our present study and Shumko et al. [132] indicate that the dayside is very special in terms of the spatiotemporal characteristics of relativistic electron microbursts. However, there is potential to misinterpret the results of these two works since Shumko et al. finds that the duration of relativistic microbursts is larger on the dayside while our work suggests that the scale size is larger, which may lead to the incorrect conclusion that our modeling results provide direct theoretical support for existing observational results. It is important to note that we analyze purely the spatial characteristics in this work, while in the work of Shumko et al., their method of directly analyzing the in situ time history of precipitation flux implies that they analyze almost purely temporal characteristics. To support this statement, we estimate the distance traveled by the LEO satellite during one microburst by multiplying the orbital speed ($7.9km/s$ for LEO) and a typical microburst time duration ($0.2s$), which gives only $1.6km$, a value that is one or two orders of magnitude smaller than the typical scale size of the microburst (several tens to more than one hundred of kilometers, from Figure 4.6). Therefore, the spacecraft can be assumed to be essentially stationary during the entire microburst measurement, so the time duration calculated by Shumko et al. is a purely temporal signature observed from a fixed location, and cannot be directly compared

with our purely spatial signature. However, both works indicate the uniqueness of dayside for relativistic microburst, although one from the time perspective [132] and one from the space perspective (this work). The more detailed and complex temporal dimension modeling and comparison with observation is ongoing in future works.

4.5 Summary

In summary, following the method for modeling the chorus-induced precipitation flux spatial characteristics developed in the previous chapter, we extended the modeling work to several chorus wave source locations distributed over L-shells and MLTs, thus trying to model the global distribution of the relativistic microburst spatial characteristics. The model setup is based on statistical results of chorus wave characteristics and electron populations. The relativistic microburst was successfully reproduced for all runs. The maximum precipitation flux and the scale size of the relativistic microburst are defined and compared among different L shells and MLTs. We found that the characteristics of microburst in the dawn and midnight sectors have little difference, but microbursts in the noon sector have larger precipitation fluxes and larger scale sizes. This is attributed to the much weaker 1-100 keV trapped electron fluxes in the dayside, which lead to a much weaker Landau damping and resultant wave propagation to higher latitudes which have access to resonate with MeV electrons. Thus, our results indicate a controlling effect of keV electron populations on the MeV electron precipitation. This work serves as a theoretical reference for future observational and statistical studies dealing with the relativistic electron microburst scale size, and is also an important step to a global modeling of quantifying the total contribution of chorus wave induced relativistic microburst.

CHAPTER 5

Lifetime of the relativistic electrons due to chorus-driven microbursts

5.1 Introduction

In this chapter, we will address the ultimate goal of this series of researches: understand how chorus waves contribute to relativistic electron loss and to assess their overall significance in this process. Specifically, we seek to evaluate the lifetime of global relativistic electron loss due to microburst precipitation driven by chorus waves.

Many previous works indicate that microbursts play a key role in the dynamics of the outer radiation belt. Previous studies have shown that microbursts act as a major loss mechanism for the relativistic ($> 1MeV$) electrons in the outer radiation belt by estimating the loss rate or lifetime using the observed microburst precipitation fluxes [92, 46, 30, 145, 54]. Although the estimated lifetime in these studies varies between several hours to several days due to different estimation methods, assumptions and trapped flux values, they all infer that during storm time, microburst can potentially empty the entire the radiation belt's relativistic electrons within a few days. Therefore, it is crucial to better understand the contribution of microburst to the relativistic electron loss in the outer radiation belt.

It is now generally accepted that microbursts are primarily triggered by chorus waves. Both statistical and event observation studies have demonstrated the connection between chorus waves and relativistic microbursts [47, 30, 92, 91, 110, 77], and many modeling works have also focused on the mechanisms of how chorus waves drive relativistic microbursts

[37, 40, 106, 107, 120, 69, 68, 66]. However, although we have established a connection between single chorus event and microburst precipitation signature, and connection between global microburst and the total outer radiation belt relativistic electron loss, our current understanding still has a gap to directly connect chorus wave activities with global relativistic electron loss. No attempt has been made to investigate the contribution of global chorus waves to the global relativistic electron loss via individual microbursts, which leaves a gap in our understanding of the importance of chorus waves in global relativistic electron loss.

The scientific goal of the present study is to establish the relationship between chorus waves and relativistic electron loss and evaluate the importance of electron loss contributed by chorus waves. We achieve this goal by addressing the following scientific question: what is the outer radiation belt relativistic electron lifetime due to chorus wave driven microburst loss? This means that we evaluate only the loss contributed by chorus waves, and our modeling is based on chorus wave information instead of directly working with microburst precipitation data. We will start with chorus waves and plasma parameter global distribution, from which we model the loss rate with a wave-particle interaction code and calculate the total electron content, thus finally obtaining the lifetime.

5.2 Estimation method

The detailed workflow is illustrated in Figure 5.1. The blue boxes represent data input/output, and the green boxes represent data processing methods. We need the following data as input: magnetospheric density model, chorus wave amplitude global distribution as a function of L-MLT (unless otherwise specified, distribution will refer to global distribution as a function of L-MLT in the remaining text), equatorial trapped electron flux distribution, and chorus element occurrence rate distribution. The first three datasets are fed into the Chorus Induced particle Precipitation (CIPP) code which calculates how many relativistic electrons can be precipitated by a single chorus element. Combining with the chorus element

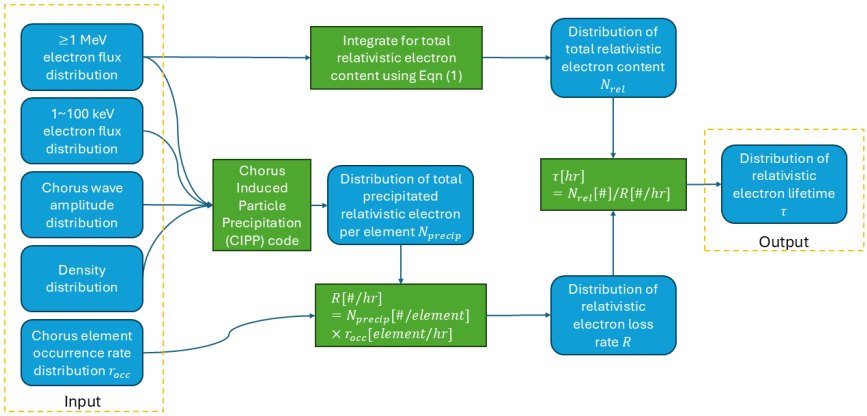

Figure 5.1: The workflow diagram of our modeling. The blue round-corner boxes represent the input or output datasets, and the green rectangular boxes represent the data processing methods.

occurrence rate (the average number of chorus element per unit time) we can calculate the relativistic electron loss rate R. This process is introduced in more detail in the following subsection.

5.2.1 Loss rate

In this subsection, we demonstrate how we calculate the loss rate through one example run: $L_{src} = 4.25, MLT = 9$. In Chapter 3 we have extensively demonstrate how we calculate the spatiotemporal distribution of the relativistic precipitation flux $J_{precip}(\lambda_{inv}, t)$, and Panels (a)-(c) in Figure 5.2 shows the familiar modeling results we have seen in previous two chapters. Using J_{precip} we can integrate for the total number of precipitated relativistic electrons N_{precip} to obtain:

$$\frac{\mathrm{d}N_{precip}}{\mathrm{d}\lambda_{inv}} = 2\pi \cdot (R_E + h) \cdot \delta s_{lon} \int J_{precip}(\lambda_{inv}, t)\mathrm{d}t, \tag{5.1}$$

where 2π represents the loss cone solid angle at the ionosphere, $h = 100km$ is the height of the ionosphere, $\delta s_{lon} = 50km$ is the longitudinal scale size of a typical microburst, as estimated

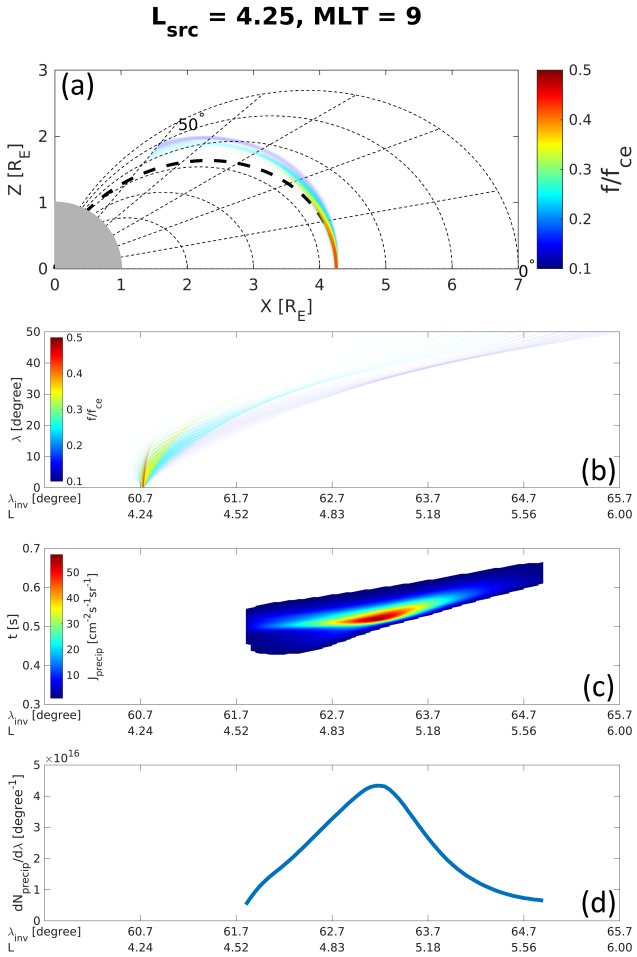

Figure 5.2: An example of a single CIPP run, whose chorus waves are launched from source region $L_{src} = 4.25, MLT = 9$. Panel (a) shows the ray paths of rays with different initial frequencies, which is color coded by the color bar on the right. The transparency of rays represents the ray power. Panel (b) shows the same ray paths as in Panel (a) but in the L-latitude coordinate. Panel (c) shows the spatiotemporal distribution of the relativistic ($> 1MeV$) precipitated flux. Panel (d) shows the total precipitated electron number per latitude as a function of latitude.

by Shumko et al. [135]. We use observed empirical value for $\delta s_{lon} = 50km$ because as a 2D model considers evolution only in a meridional plane, and the model needs to be extrapolated in longitude since it does not have the ability to obtain longitudinal variation. The validity of Equation 5.1 can be observed by noting that the precipitation area at the ionosphere $\mathrm{d}A = \delta s_{lat}\delta s_{lon} = (R_E + h)\mathrm{d}\lambda_{inv} \cdot \delta s_{lon}$ and $\mathrm{d}N_{precip} = J_{precip}\mathrm{d}\Omega\mathrm{d}A\mathrm{d}t$. $\frac{\mathrm{d}N_{precip}}{\mathrm{d}\lambda_{inv}}$ in this run is plotted in Figure 5.2 (d).

The final step is to convert the N_{precip} into the loss rate R, which will involve the occurrence rate of chorus wave element r_{occ} to convert the precipitation per element into loss rate (i.e., the precipitation per unit time). We denote the $\frac{\mathrm{d}N_{precip}}{\mathrm{d}\lambda_{inv}}$ as n_{precip}, which is a function of chorus wave source region L-shell L_{src} and MLT, and λ_{inv} which represents the precipitation location on the ionosphere. $n_{precip}(L_{src}, MLT, \lambda_{inv})$ represents the λ_{inv} distribution of the number of precipitated relativistic electrons per λ_{inv} induced by a single chorus element originated from (L_{src}, MLT). Since a single chorus wave element propagating in an unducted mode typically results in precipitation at a range of λ_{inv} in the same meridional plane, calculating the loss rate at λ_{inv} should include the contributions of all chorus waves from different L_{src}:

$$\frac{\mathrm{d}R(\lambda_{inv}, MLT)}{\mathrm{d}\lambda_{inv}} = \int n_{precip}(L_{src}, MLT, \lambda_{inv}) r_{occ}(L_{src}, MLT)\mathrm{d}L_{src}, \tag{5.2}$$

and the loss rate at any L-shell bin can be obtained by $R(\lambda_{inv}, MLT) = \frac{\mathrm{d}R(\lambda_{inv}, MLT)}{\mathrm{d}\lambda_{inv}}\Delta\lambda_{inv}$. Hereafter we shall denote the field line with L-shell instead of λ_{inv} to be consistent with the common practice in magnetospheric statistical studies.

5.2.2 Total relativistic electron content

The relativistic ($> 1MeV$) equatorial electron flux is also used to calculate the relativistic total electron content (TEC) using the following formula, according to the method in Thorne et al. [145]:

$$\frac{\partial^2 N_{rel}}{\partial L \partial \phi} = \frac{1}{c}\int_{1MeV}^{\infty} \mathrm{d}E \int_0^{\pi} \mathrm{d}\alpha \sin^{n_L+1}(\alpha) j_{\perp}(L, E) \frac{E + mc^2}{\sqrt{E(E + 2mc^2)}} \frac{\partial^2 V}{\partial L \partial \phi}, \tag{5.3}$$

where $j_\perp$ is the trapped equatorial electron flux, α is the pitch angle, E is the energy, L and ϕ are the L-shell and azimuthal angle, n_L is the pitch angle index under the assumption that the electron flux pitch angle distribution takes the form $j(L, E, \alpha) = j_\perp(L, E)\sin^{n_L}(\alpha)$. $\frac{\partial^2 V}{\partial L \partial \phi}$ is the flux tube volume per L-shell per azimuthal angle under a dipole model, and can be derived from

$$\frac{\partial V}{\partial \phi} = \frac{2R_E^3}{105}\sqrt{1-\frac{1}{L}}(16L^3 - 8L^2 + 6L - 30), \tag{5.4}$$

with $\frac{\partial^2 V}{\partial L \partial \phi} = \frac{\partial}{\partial L}\frac{\partial V}{\partial \phi}$, where $R_E = 6371km$ is the Earth radius. After obtaining the total relativistic electron content, we can divide it with the loss rate to obtain the relativistic electron lifetime due to chorus waves:

$$\tau = \frac{N_{rel}}{R}. \tag{5.5}$$

5.2.3 Model setup

We use the results of the 20 runs over different L-shells and MLTs in Chapter 4 to calculate the electron lifetime. The statistical models used are the same as we show in Figure 4.2, 4.3 and 4.4. We show the new dataset we mentioned in Section 5.2.1, the chorus element occurrence rate, defined as the total chorus element count/total RBSP flight time in each L-MLT bin, based on the dataset in He et al. [58].

The 20 runs over 4 L_{src} and 5 MLTs are used as "sample" runs. To increase the L-MLT resolution of the $\frac{\mathrm{d}R(\lambda_{inv},MLT)}{\mathrm{d}\lambda_{inv}}$, for any other source region location between $4.25 \leq L_{src} \leq 5.75, 0 \leq MLT \leq 12$, its $\frac{\mathrm{d}N(\lambda_{inv},MLT)}{\mathrm{d}\lambda_{inv}}$ function is then linearly interpolated from the $\frac{\mathrm{d}N(\lambda_{inv},MLT)}{\mathrm{d}\lambda_{inv}}$ functions of its nearby "sample" locations. The interpolation method is shown in Figure 5.4.

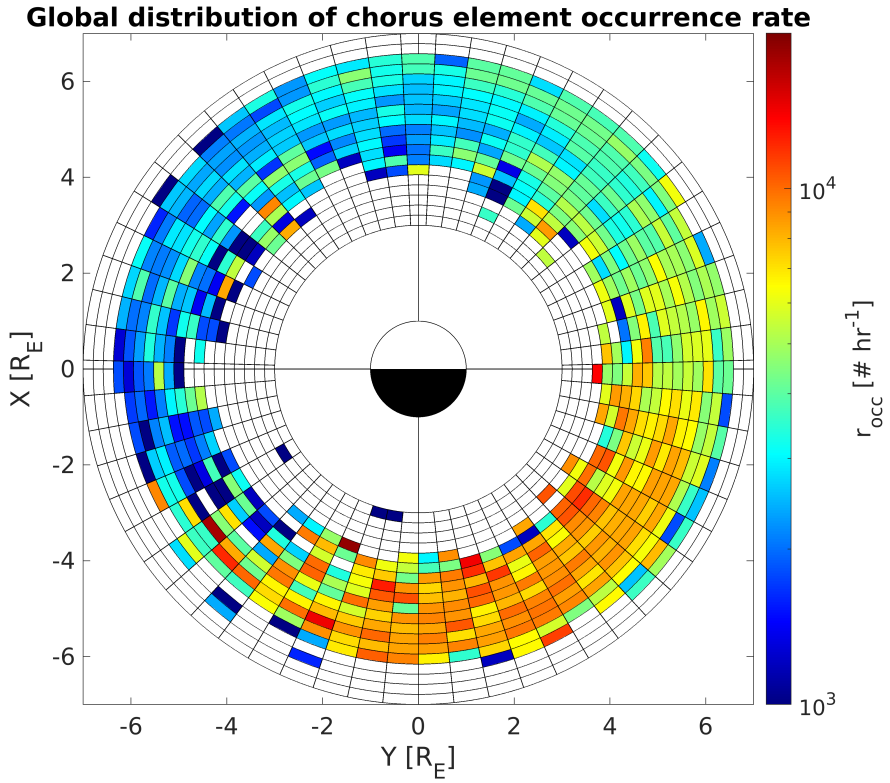

Figure 5.3: The global distribution of chorus wave element occurrence rate from RBSP.

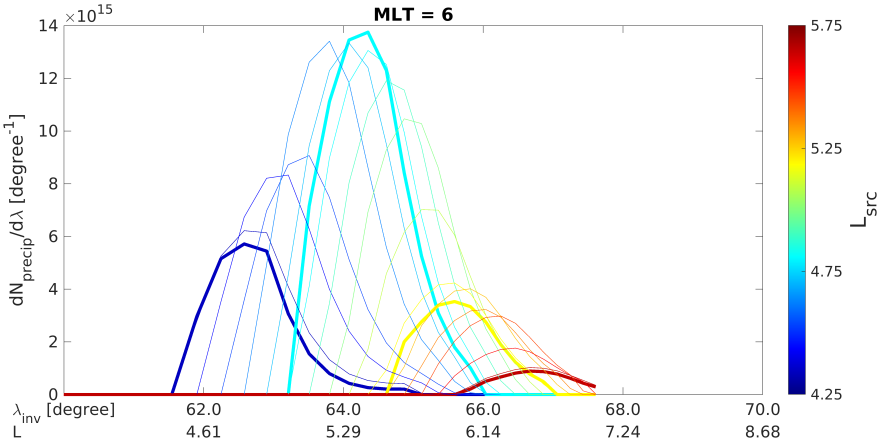

Figure 5.4: Illustration of the method interpolating $\frac{\mathrm{d}N(\lambda_{inv},MLT)}{\mathrm{d}\lambda_{inv}}$ on $MLT = 6$. Different colors represents $\frac{\mathrm{d}N(\lambda_{inv},MLT)}{\mathrm{d}\lambda_{inv}}$ for different L_{src}. The 4 thick lines represents the "sample" curves from the runs $L_{src} = 4.25, 4.75, 5.25$ and 5.75, and the thin lines are the interpolated results.

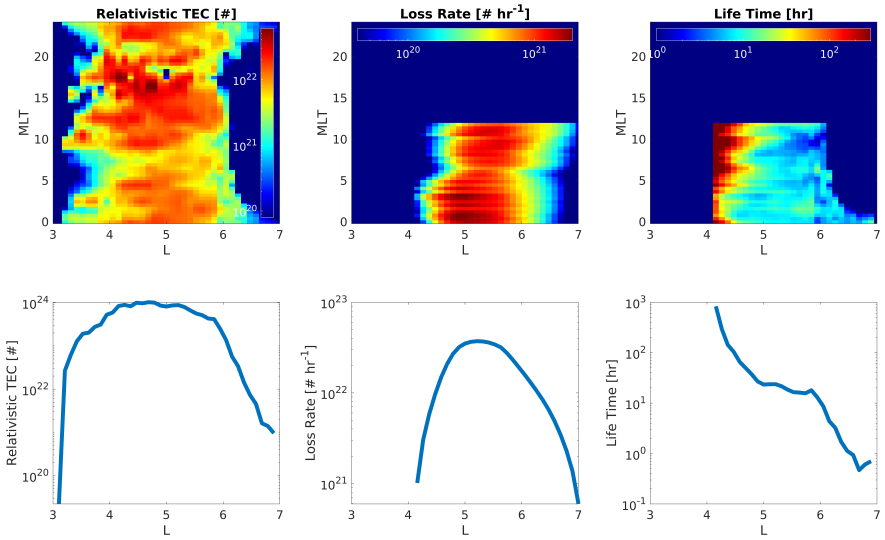

Figure 5.5: The modeling results of the relativistic TEC (Panel (a) and (d)), loss rate (Panel (b) and (e)) and lifetime (Panel (c) and (f)). Panels (a)-(c) are shown in L-MLT bins, and Panels (d)-(f) show the total quantity of these values within each L-shell, as a function of L-shells.

5.3 Lifetime results and discussion

Figure 5.5 shows the modeling results of the total relativistic electron content, loss rate and relativistic electron lifetimes. The statistical results are shown in an L-shell-MLT grid with bin width of $\Delta L = 0.1, \Delta MLT = 0.4$. Panels (a)-(c) show the relativistic TEC, loss rate and lifetime within each L-shell-MLT bins, and Panel (d)-(f) show the relativistic TEC, loss rate and lifetime for each L-shell, where relativistic TEC and loss rate are calculated by summing over all MLT bins at the same L-shells, and lifetime is calculated by the summed relativistic TEC divided by the summed loss rate.

We now can compare our results with previous estimates. Figure 4(d) indicates that the relativistic TEC is around $10^{24} - 10^{25}$ electrons per L-shell (considering a width of $\Delta L = 0.1$) between $4 \leq L \leq 6$, which agrees very well with Selesnick and Kanekal [124] who also provides $\frac{\partial^2 N}{\partial L \partial E} = 10^{24} - 10^{25} MeV^{-1}$. Figure 5.5 (f) shows that the relativistic electron

lifetime ranges from several hours near geosynchronous orbit, up to 100 hours at $L \approx 5$ which is roughly consistent with the estimated lifetime of 10 100 hours by Thorne et al. [145]. This means that during chorus wave active times, the relativistic electrons in the outer radiation belt can be depleted within a few days in the outer radiation belt.

We estimate a lifetime of several hundred hours up to 1 thousand hours at lower shells, in the range $4 \leq L \leq 5$, which is an extremely large value that exceed previous estimates. For example, Thorne et al. gave an estimated lifetime of around 10 hours in this L-shell range, which is almost 3 orders of magnitude smaller than our estimate. We consider our value to be an overestimate of the realistic lifetime due to two reasons: a) The lowest chorus wave source region L-shell we choose is $L_{src} = 4.25$, and because the relativistic precipitation occurs at higher L-shells compared to the chorus wave source region, we omit precipitation induced by chorus waves from $L_{src} < 4.25$, which mainly occur between $4 \leq L \leq 5$; b). Additionally in the case of a density duct, the relativistic precipitation will occur on the same field line as chorus wave source region and have stronger precipitation fluxes [66, 40]. Considering this is the near-plasmapause region where density ducts are frequently observed [139, 109, 101, 45], we might underestimate the chorus driven precipitation flux because we do not consider density ducts. We estimate a lifetime of just a few hours for $L > 6.5$, which might have been underestimated because the L-shell volume calculated by a dipole model is an underestimation of the realistic stretched field at the high L-shells, therefore the relativistic TEC might be underestimated.

The goal of this work is to establish a connection between chorus waves and relativistic electron lifetimes with a start point of chorus wave related statistical results, where the chorus driven microbursts are a proxy that connects chorus waves and relativistic electron lifetime. Meanwhile, in Thorne et al. [145], they directly established the relation between microbursts and relativistic electron lifetime with a start point of microburst statistics. Therefore, our modeling yields a lifetime of several tens of hours between $5 < L < 6.5$ which is consistent with Thorne et al. [145] implying that the extended connection from microburst to chorus

waves is reasonable, and chorus waves are the dominant driver of microburst electron loss in this region.

5.4 Summary

In this study, we investigated the relativistic electron lifetimes due to chorus driven microburst precipitation using a modeling approach. Using our CIPP code, we estimated the chorus driven relativistic electron loss rates at different L-shell-MLT bins based on statistically averaged chorus wave distributions of and chorus wave element occurrence rate. We also obtained the relativistic TEC at different L-shell-MLT bins from a statistical relativistic electron flux global distribution. We then calculated both the total relativistic TEC and the electron loss rate within each L-shell bin, whose quotient yields the relativistic electron lifetime. The resulting lifetimes of relativistic radiation belt electrons as a function of L-shell was shown in Figure 5.5 (f). Our modeling results indicate a lifetime of several tens of hours at the core region of the outer radiation belt ($5 \leq L \leq 6.5$), which is consistent with previous observational studies (Thorne et al. [145]) and much larger lifetimes at lower L-shells. We conclude from our modeling results that during geomagnetically active times, when chorus wave intensity and occurrence rate peaks the relativistic electrons in the outer radiation belt can be depleted by chorus waves within a few days under the present assumptions. This work establishes a theoretical relationship between chorus wave and relativistic electron lifetime via individual microbursts, and confirms the important role that chorus waves play in the loss process of the outer radiation belt.

CHAPTER 6

The principal role of chorus ducting for night-side relativistic electron precipitation: a special case study

6.1 Introduction

In the previous 3 chapters, we have completed the series of modeling works on chorus wave driven relativistic microburst using our CIPP code, from microscopic physical process investigation through single event modeling to macroscopic global distribution and global impact studies. In this chapter, we will present a "bonus" research focusing on what the role the ducting effect plays in the chorus wave driven relativistic microburst. In the previous works, we all assume a smooth magnetospheric density distribution so that the chorus waves all propagate in the unducted mode, and the impact of density duct has not been considered yet. In this work, inspired by a strong relativistic microburst event observed on the nightside by ELFIN, we conduct an event-based modeling to investigate the role of chorus ducting for relativistic electron precipitation.

It has been shown in observations via many spacecrafts (e.g. THEMIS, CRRES, Cluster, Dynamic Explorer 1, Double Star TC1 etc.) that the night-side chorus waves are usually confined around the equatorial plane, whereas dayside waves can propagate to middle or even high latitudes [102, 3, 123]. For the most intense field-aligned chorus waves, this difference in the wave latitudinal extent directly leads to their different contributions to electron losses and acceleration [103]: night-side, near-equatorial waves are mostly responsible for the precipitation of $< 100keV$ electrons and effective in electron acceleration up to relativistic

energies [5], whereas dayside waves are responsible for relativistic electron losses [145]. Indeed, the distribution of the most intense precipitation events, microbursts, have confirmed the prevalence of electron losses on the dayside [47, 133, 36, 129]. However, all the statistical works mentioned above also indicated the presence of relativistic electron precipitation on the night-side. Recent observations from the low-Earth-orbit (LEO) ELFIN CubeSats have also shown these very intense relativistic electron precipitation signatures on the night-side [12]. These evidences of non-rare, night-side, strong relativistic precipitation is in contrast with our theoretical understanding we mentioned above, and there is no good theoretical explanation for these relativistic electron precipitation on the night-side. Considering the occurrence rate of night-side relativistic microbursts is comparable in dawn and day side [47, 133, 36, 129], and their important contributions to relativistic electron losses is confirmed [148], it is crucial to explore the mechanism that drives the night-side relativistic precipitation in order to better understand the dynamics of radiation belts.

Two potential mechanisms can lead to relativistic electron losses in the night-side inner magnetosphere. First, after being generated around the equator, whistler waves may propagate along curved magnetic field lines, become very oblique and resonate with relativistic electrons through high-order resonances (see discussions in [91]). Indeed, this mechanism for relativistic electron precipitation has been confirmed in the dawn-flank magnetosphere [49], but it is unclear whether the same mechanism can work on the night-side, where enhanced suprathermal electrons damp oblique waves much more effectively (e.g., [38]). Second, these equatorially generated waves can be trapped into local density ducts (e.g., [56, 40]) and propagate to middle latitudes or all the way to the ionosphere without damping [131]. At middle latitude, these intense field-aligned chorus waves may provide effective scattering and precipitation of relativistic electrons. This mechanism was proposed to explain relativistic electron losses on the dusk-side and dayside (e.g., [10, 39]), but has not been verified for the night-side.

In this study we examine ELFIN [9] observations of very intense, relativistic (up to

$1-2MeV$) electron precipitation in the night-side inner magnetosphere. Using ELFIN electron measurements with high energy resolution, we separate the chorus-driven precipitation from the plasma sheet precipitation due to electron scattering by the magnetic field line curvature (see discussions of this mechanism in [161, 34]). Then we simulate electron resonant interactions with chorus waves traced in a realistic magnetosphere configuration (see the model details in [69]), in order to evaluate the relative importance of unducted (oblique) and ducted (field-aligned) wave scattering. As shown in simulations, the observed relativistic electron precipitation at the strong diffusion limit (completely filled loss cone; see [74]) can only be explained by the scattering of ducted waves. These results imply the importance of incorporating realistic plasma density structures and wave distributions into global radiation belt models.

6.2 Event description and model setup

We analyze in details ELFIN CubeSat observations recorded during the two-day interval 11–12 June 2021. These observations were captured during a prolonged interval of elevated geomagnetic activity, with the auroral index, SML, remaining below $-300nT$ and ring current index, SMR, below $-20nT$ [52] for the majority of the time, due to a series of plasma injections (see Fig. 6.1(a)). The ELFIN energetic particle detector, EPDe, measures electron energy, pitch-angle distributions over $50-6000keV$ in 16 logarithmically distributed energy channels [9]. ELFIN's polar, low-altitude ($\sim 450km$) orbit allows it to quickly traverse a wide range of magnetic field lines, in the inner magnetosphere to the plasma sheet, within $\sim$ 5min. The temporal resolution of EPDe measurements is $3s$, i.e. the ELFIN spin rate. To examine the precipitation from the equatorial magnetosphere, we mainly use two data products: the energy spectrum of locally trapped electrons (outside the bounce loss-cone), j_{trap}, and the energy spectrum of precipitating electrons (inside the bounce loss-cone), j_{prec} [7]. Their ratio, j_{prec}/j_{trap}, signifies the intensity of electron scattering around the equator

[75, 87].

Figure 6.1 (b1-d3) shows ELFIN observations during three orbits on 11 June 2021: the trapped spectra in panels (b), precipitating-to-trapped flux ratios in panels (c), and ELFIN MLT and L-shell (calculated using the model [153]) in panels (d). Note that there can be large uncertainties for the night-side in projecting ELFIN to the equator to estimate L-shell, especially during substorms when magnetic field lines are very deformed in the magnetotail region (see discussions in [136, 11]). Thus, we only trust the low L values in the inner magnetosphere, and use j_{trap} and j_{prec}/j_{trap} to identify different magnetospheric regions in ELFIN measurements. Let us illustrate this identification procedure using panels (b1, c1). Before 02:50:10 UT, ELFIN measures locally trapped fluxes below 200keV with a strong flux anisotropy, $j_{prec}/j_{trap} < 0.1$. This is consistent with the plasmasphere, which is often replenished by freshly injected electrons in the night-side. Between 02:50:10 and 02:50:25 UT, ELFIN observed enhanced relativistic electron fluxes, mostly trapped with sporadic precipitation bursts, $j_{prec}/j_{trap} > 0.1$ and j_{prec}/j_{trap} decreases with energy. This is the outer radiation belt region, whereas precipitation bursts are due to electron scattering by whistler-mode (chorus) waves: for these waves, the pitch-angle diffusion coefficient decreases with the energy increase (e.g., [140, 111]), in agreement with the observed j_{prec}/j_{trap}. Around 02:50:30 UT, ELFIN traversed the isotropy boundary – transitioning between the outer radiation belt with $j_{prec}/j_{trap} < 1$ and the plasma sheet with $j_{prec}/j_{trap} \approx 1$. Such strong energetic electron precipitation is due to curvature scattering in the magnetotail current sheet [62, 127, 126]. The plasma sheet region is characterized by $< 200keV$ electron fluxes, usually isotropic, $j_{prec}/j_{trap} \approx 1$ [11]. A characteristic feature of the isotropy boundary is the energy/L-shell dispersion (for an excellent example see Figure 2 in [159]): electrons at higher energies start to experience the curvature scattering at lower L-shells (with larger curvature radius) and hence show $j_{prec}/j_{trap} \approx 1$ closer to the Earth [126]. The high energy and pitch-angle resolution of ELFIN EPDe allows us to distinguish precipitation due to curvature scattering and due to the whistler-mode wave scattering (see discussions in [149, 11]). As shown in Fig.

6.1 (b1-d1), ELFIN measurements were captured during the substorm growth phase, where the absence of plasma injections explains the lack of intense chorus waves, but the very thin magnetotail current sheet can drive strong curvature scattering and electron precipitation below $200keV$.

Figures 6.1 (b2-d3) show ELFIN observations during two orbits after a substorm injection: the plasma sheet is only captured fragmentally, likely due to near-Earth dipolarization that prevents electron curvature scattering (see discussions in [130, 94]); the outer radiation belt is filled by hot injected electrons as a viable source for chorus wave generation (e.g., [142, 98]). Electron precipitation due to chorus wave scattering has a very clear energy dispersion, with the precipitating-to-trapped flux ratio decreasing with energy increase (panels (c2, c3)). This precipitation pattern exhibits several spatially localized bursts (likely associated with the chorus wave generation regions around plasma injections, see discussions in [162, 12]). Energies of precipitating electrons can reach 500–$700keV$, and in panel (c3) $700keV$ precipitating electrons show precipitating-to-trapped flux ratio around one, i.e., relativistic electrons are precipitated at the strong diffusion limit.

Figures 6.1 (b4-d6) show ELFIN observations during three orbits on 12 June 2021. Similar to the three orbits in 6.1 (b1-d3), the first orbit during substorm growth phase shows a very clear isotropy boundary reaching $1MeV$ in energy (panel (c4)). Two subsequent orbits show electron precipitation bursts in the outer radiation belt after the injections. This precipitation is likely due to electron scattering by chorus waves. As shown in the observations, these electron precipitation, likely driven by chorus waves at the strong diffusion limit, can reach $1-2MeV$. Therefore, Fig. 6.1 demonstrates multiple examples of unusually strong precipitation bursts of relativistic electrons observed on the night-side.

Although the ELFIN measurements in Fig. 6.1 were not in conjunction with equatorial spacecraft measurements, there is a good coverage of equatorial plasma and wave dynamics by MMS [32], Arase [108], THEMIS [8], and GOES-16. Based on their observation, injection (measured by energetic particle detector, see [70, 20]), cold plasma density structures (derived

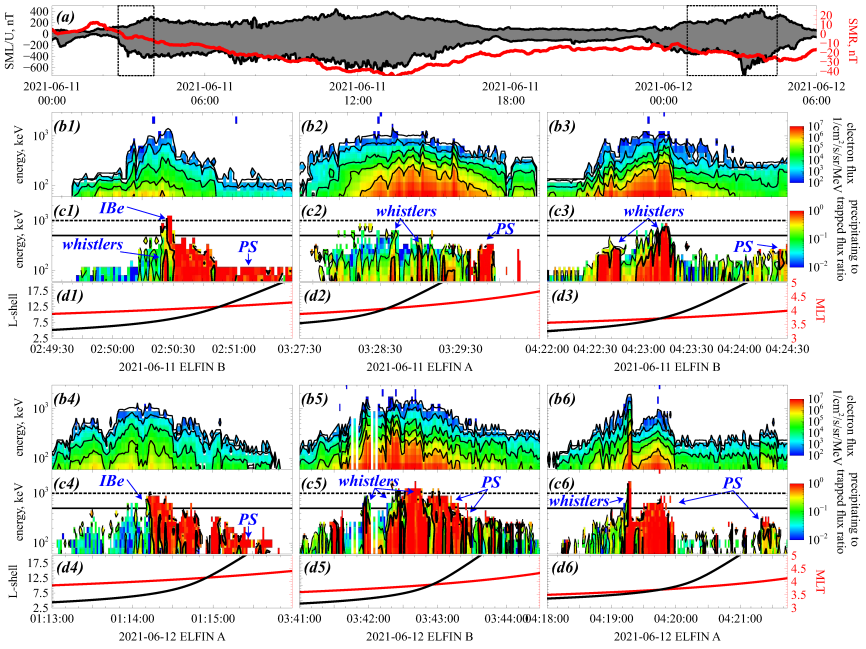

Figure 6.1: Overview of ELFIN A&B observations during two substorms on 11–12 June 2021. Panel (a) shows SuperMAG indices. Panels (b1–d3) show ELFIN observations during three orbits during the first substorm at 02:00–05:00 UT on June 11: locally trapped fluxes (b1, b2, b3), precipitating-to-trapped flux ratio (c1, c2, c3), and ELFIN L-shell and MLT (d1, d2, d3). Panels (b4–d6) show ELFIN observations during three orbits during the second substorm at 00:00–05:00 UT on June 12: locally trapped fluxes (b4, b5, b6), precipitating–to-trapped flux ratio (c4, c5, c6), and ELFIN L-shell and MLT (d4, d5, d6). Horizontal lines in panels (c) mark two key energy levels: 500keV (solid line) and 1MeV (dashed line). In panels (c), we also indicate precipitation patterns as identified by their location and energy dispersion: isotropic fluxes at large L-shell are due to electron curvature scattering in the plasma sheet (PS); L-shell/energy dispersion with higher-energy electron precipitation at lower L-shell is a signature of the electron isotropy boundary (IBe); precipitation bursts with a lower precipitating-to-trapped ratio at higher energies are due to electron scattering by whistler-mode waves.

from spacecraft potential, see [112]), and whistler-mode chorus wave activities (measured by electric field instruments and search-coil magnetometers, see [14, 81, 21, 71]) are confirmed during the events from Figure 6.1. Therefore, ELFIN observations of strong electron precipitation are associated with periods of multiple plasma sheet injections, which serves as the free energy source for chorus wave generation [142, 48, 98] and reduces the f_{pe}/f_{ce} ratio [1] that plays an important role for scattering and precipitating relativistic electrons (see discussions in [148]).

6.3 Modeling results

To probe the mechanism driving the observed night-side relativistic electron precipitation within the strong diffusion regime, we conduct event-based modeling for ducted and unducted chorus waves, respectively. The chorus wave-particle interaction model employed in this study follows the same methodology as in [69, 68], whose basic procedure is described below. Utilizing ray tracing techniques, we trace the ray paths of chorus waves originating from an equatorial chorus wave source, with Landau damping included which yields the amplitude attenuation of waves. From the ray paths and wave amplitudes along ray paths, we can reconstruct the latitudinal distribution of wave amplitude along a certain field line from all the rays that cross the field line. Subsequently, quasi-linear electron scattering calculations are performed on the field lines, yielding the energy-time (E–t) spectrum for the j_{prec}, and thus the j_{prec}/j_{trap} ratio at each field line's footpoint. (For technical details about this model see discussions in [69, 68, 25].)

We establish our model based on the observations discussed in the preceding section, with a particular focus on the precipitation signature at $L = 8.7$, where ELFIN has detected significant relativistic electron precipitation (whistler mode wave induced precipitation is between $7.5 < L < 10$, and the precipitation due to isotropic boundary occurs beyond $L = 10$, e.g. Figure 1 (c,d3) and (c,d5)). For the unducted case, we adopt an empirical

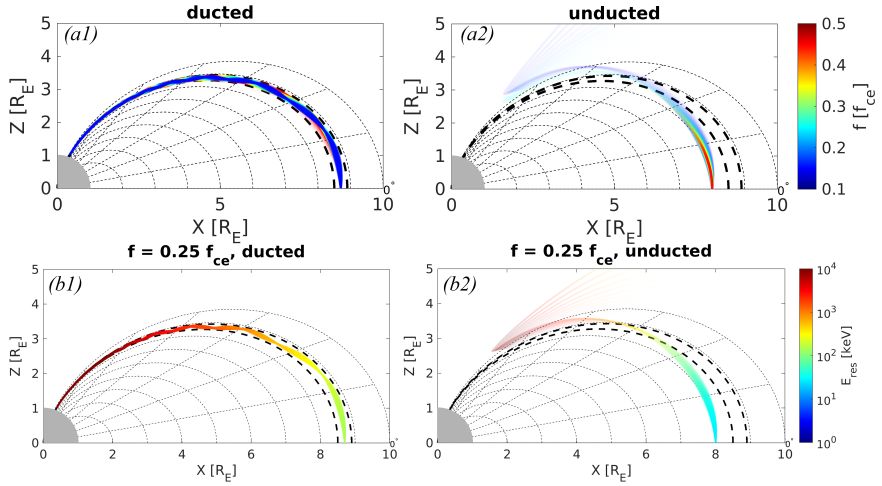

Figure 6.2: Overview of ray paths and resonance energies for both ducted (left) and unducted (right) cases. Panels (a1) and (a2) show the ray paths of waves with different frequencies, color-coded as indicated in the top-right color bar. Panels (b1) and (b2) illustrate the (cyclotron) resonance energy along the ray paths of waves at a fixed frequency of $0.25 f_{ce}$, with colors denoting the resonance energy as shown in the bottom-right color bar. Panels (a1) and (b1) are for the ducted case, whereas panels (a2) and (b2) are for the unducted case. The transparency of ray paths in all panels reflects their wave power, with fading rays illustrating damping. Thin dashed lines denote field lines with an L shell interval of 1 and latitude lines with a latitude interval of 10°; the two thick dashed lines represent field lines for $L = 8.5$ and $L = 8.9$, which, in the ducted case, mark the half-width boundary for the enhanced density duct.

night-side density model [35], adjusting it to ensure that the equatorial density at $L = 8.7$ maintains $f_{pe}/f_{ce} \approx 3$, consistent with observations from THEMIS (further insights on the role of f_{pe}/f_{ce} are provided in the Discussion section). For the ducted case, we introduce a relatively large (yet realistic, see [144, 55, 41, 73, 85]) density-enhanced duct with a 50% enhancement factor and a half-width of $0.2R_E$ centered around the field line $L = 8.7$, expressed as $n_{ducted} = n_{unducted}(0.5e^{-\frac{(L-8.7)^2}{0.2^2}} + 1)$ (see observations and simulations of similar ducts in [131, 73, 40, 55]). Considering the parallel propagation characteristics of chorus waves within such ducts (e.g., [41]), we position the equatorial chorus wave source region at the center of the duct ($L = 8.7$). In contrast, unducted chorus waves, while propagating to higher latitudes and attaining relativistic resonance energies, also extend to higher L shells (see Figure 3 of [69]). Hence, for the unducted case, we initialize the chorus wave source region at $L = 8$, ensuring that as the wave rays propagate to the target field line at $L = 8.7$, they have already reached relativistic resonance energy (see Figure 6.2 (b2)). We initialize the chorus waves with a frequency span of $0.1f_{ce} < f < 0.5f_{ce}$ and an initial quasi-parallel wave normal angle (WNA) distribution with a bandwidth of 15° (Equation 4 of [68]). During the ray tracing process, the electron velocity distribution utilized for Landau damping calculations (see [38, 31]) is derived from electron flux data obtained by THEMIS during the event. Since there is no direct conjugate observation of equatorial chorus wave amplitude, we assume a relatively large value of $B_w = 200pT$ for the chorus wave amplitude (e.g., [85]). It is worth noting that the wave amplitude B_w scales linearly with the amplitude of electron pitch-angle scattering rate, $\Delta\alpha$, in the quasi-linear regime. Thus, this parameter should be viewed as a normalization factor for $j_{prec}/j_{trap} \propto \Delta\alpha \propto B_w$.

Figure 6.2 shows the ray tracing results for the ducted (panels (a1) and (b1)) and unducted (panels (a2) and (b2)) cases. Panels (a1) and (a2) depict the ray paths with varying frequencies (color-coded according to the top-right color bar), while panels (b1) and (b2) display the cyclotron resonance energy along the ray paths at a fixed frequency of $f = 0.25f_{ce}$. Power reduction due to Landau damping is indicated by the fading of ray paths, i.e., increas-

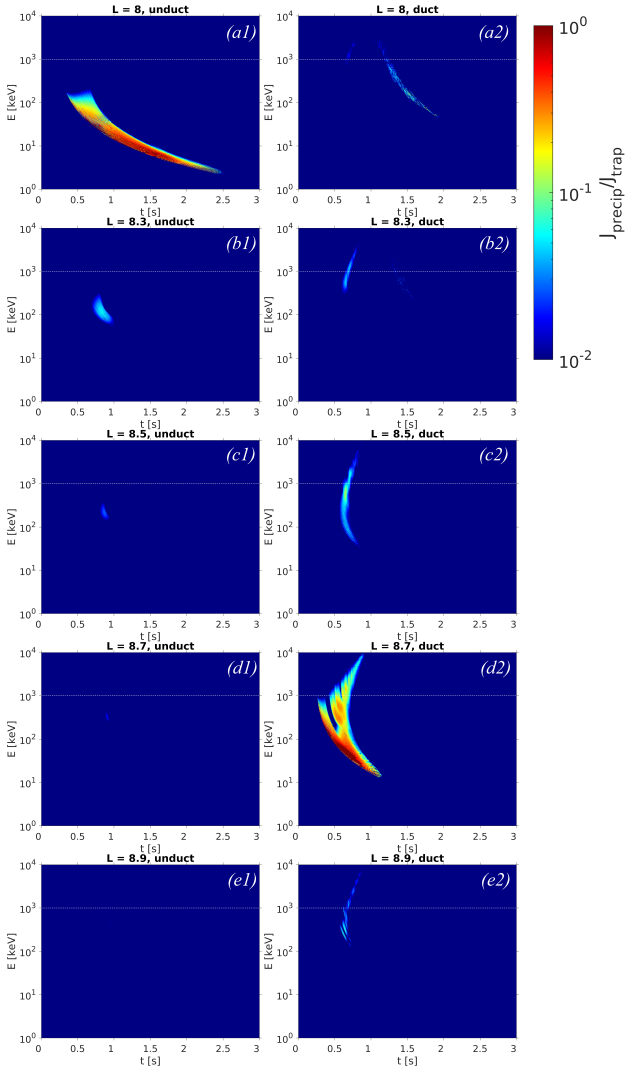

Figure 6.3: Panels (a) to (e) are E–t spectra of the j_{prec}/j_{trap} ratio at different field line footpoints for the ducted and unducted cases, respectively. Panels (a1)–(e1) represent field line footpoints at $L = 8$, 8.3, 8.5, 8.7, and 8.9, respectively, for the unducted case, whereas panels (a2)–(e2) depict the same for the ducted case. The ratio contour is color-coded according to the top-right color bar, with the horizontal white dashed line marking the 1 MeV energy.

ing transparency of the ray paths. From panel (a1), we can see that all waves are effectively guided by the duct, with only minor leakage of high-frequency waves. Ducted waves experience minimal damping as they remain quasi-parallel within the duct [41, 93], retaining significant wave power even at high latitudes ($> 50°$). In contrast, panel (a2) reveals that unducted waves undergo substantial damping [41], with the majority of wave power lost after propagating above a latitude of 20°. This difference in the latitudinal extent of the strong-wave-power region between ducted and unducted cases is crucial for their distinct j_{prec}/j_{trap} ratios in the $\sim MeV$ energy range. From panels (b1) and (b2), we can see that in both cases, chorus waves do not attain $\sim MeV$ resonance energy until they propagate beyond 20° in latitude [91, 69, 39, 107]. Therefore, it is crucial for chorus waves to convey sufficient wave power to the high-latitude, MeV-resonance region to enable strong diffusion at the MeV energy range, thereby making ducting the only plausible explanation for the observed night-side strong $\sim MeV$ precipitation, as demonstrated later.

Figure 6.3 shows the energy-time (E–t) spectra of j_{prec}/j_{trap} ratio at various field line footpoints for both ducted and unducted cases. Panels in the left column depict results for the unducted case, while those on the right represent the ducted case. We examine the precipitation signatures at five different field lines: $L = 8, 8.3, 8.5, 8.7$ and 8.9. Note that $L = 8$ is the chorus wave source region for the unducted case, whereas $L = 8.7$ is the source region for the ducted case. It is evident that the unducted and ducted waves exhibit their strongest precipitation at distinct locations and energy ranges. In the unducted case, strong precipitation is solely observed at $L = 8$, around the wave source region, at energies below $100keV$, typical of night-side chorus waves (e.g., [5]). By comparing the energy range with Figure 6.2 (b2), we can further determine that the scattering occurs below latitudes of 20°. Conversely, in the ducted case, intense scattering is only observed at $L = 8.7$, the center of the duct. Here, precipitation spans a wide energy range from several tens of keV up to several MeV. Combining with Figure 6.2 (b1), we discern efficient scattering that occurs from the equator all the way up to latitudes of 50°. From Figure 6.3, we can see that relativistic

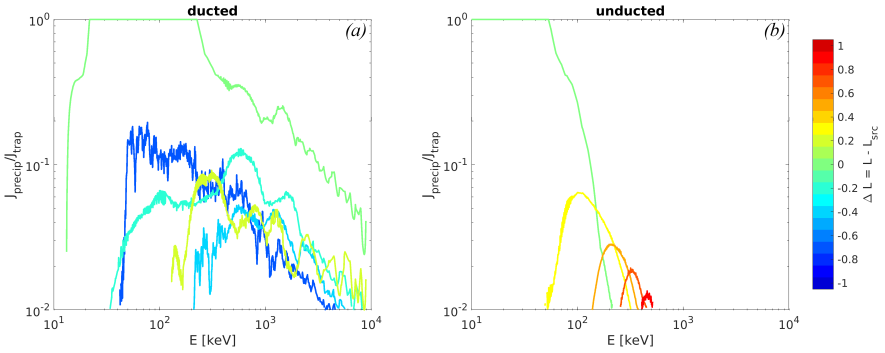

Figure 6.4: Panels (a) and (b) show the max(j_{prec}/j_{trap})–E curves at different L-shells for both the ducted and unducted cases. Panel (a) presents the ducted case, while panel (b) presents the unducted case. Curves at different L-shells are color-coded based on their distance ΔL from the L-shell of the chorus wave source region, as indicated by the color bar on the right. Note that $L_{src} = 8.7$ for the ducted case and $L_{src} = 8$ for the unducted case.

precipitation ($E \gtrsim 1MeV$) is only possible in the ducted case, and relativistic precipitation near strong diffusion limit is solely attainable at the duct's center.

To examine the locations and energy ranges where the strong diffusion limit can be attained, and to depict how the j_{prec}/j_{trap} ratio–E relation evolves with L-shells, we present in Figure 6.4 (a) and (b) the maximum j_{prec}/j_{trap} over the entire time period (max(j_{prec}/j_{trap})) versus energy at different L-shells for both the ducted and unducted cases. Panel (a) shows the results for the ducted case, while panel (b) shows the unducted case, with curves of varying colors corresponding to different L-shell distance ΔL to chorus wave source region L_{src} as delineated by the color bar on the right. Panel (b) shows that in the unducted case, the strongest precipitation occurs near the source region ($\Delta L = 0$, or $L = 8$) within a lower energy range of $< 100keV$; at field lines farther from the source region, precipitation at increasingly higher energies is observed, albeit with a dramatic decrease in intensity. This is because unducted chorus waves reach higher L-shells at higher latitudes, where the waves resonate with higher energy electrons but much weaker wave amplitude due to strong Landau damping on the night-side (see Figure 6.2(b2)). Conversely, in the ducted case (panel (a)),

the center of the duct ($\Delta L = 0$, or $L = 8.7$) exhibits the highest precipitation intensity compared to all other field lines (as indicated by the orange curve); the strong diffusion limit is achieved between $20 \sim 200keV$ and maintains a significant j_{prec}/j_{trap} ratio of > 0.1 up to several MeV. Field lines near the duct boundary ($\Delta L = \pm 0.2$, or $L = 8.5, 8.9$) show similar relativistic precipitation energy range, although with lower intensity, indicative of very effective wave power guiding within the duct. This ducting effect traps almost all wave power at the duct's center, where weak Landau damping allows a significant amount of the wave power to persist to high latitudes, producing the scattering of relativistic electrons and thus generating strong relativistic precipitation at the duct's center.

6.4 Discussion and summary

We show that only ducted wave propagation enables chorus waves to reach sufficiently high latitudes to scatter and precipitate relativistic electrons close to the strong diffusion limit. However, the efficiency of ducting and wave–particle resonant interactions relies on the characteristics of cold plasma density, which are not directly measured during these events and must be inferred from statistical models. The background density magnitude (determining $f_{pe}/f_{ce} = 3$) under the assumed duct amplitude of 50% deviates from typical values: empirical models suggest $f_{pe}/f_{ce} \sim 8$ for $L \sim 8$ [128]. Nevertheless, the modeled events of relativistic electron precipitation occur during strong substorm activity (see Fig. 6.1 (a)), which is usually associated with a decrease in the night-side f_{pe}/f_{ce} to 2–4 [1], likely due to enhanced earthward transport of cold plasma. For $L \sim 8$, $f_{pe}/f_{ce} = 3$ indicates that the background density is only 0.4cm^{-3} and 0.6cm^{-3} within the duct. Although these density differences may seem substantial in relative terms, they are not uncommon for the night-side inner magnetosphere during plasma sheet injections (e.g., [53, 90]). The local f_{pe}/f_{ce} is more important when we focus on the resonance energy, especially in the ducted case where waves propagate within a narrow L-shell range, and we ensure that by scaling down the density

model to make $f_{pe}/f_{ce} = 3$ at $L = 8$. Therefore, the density profile at a wider range of L-shells is relatively less important, thus although we have to extrapolate the density model (because the reference CA model gives density profile up to $L \approx 7$) which may potentially lead to extra error, the impact should be of second-order.

Our modeling results indicate that strong chorus-driven, night-side relativistic precipitation can only occur in the presence of a density duct. Interestingly, considering that night-side relativistic precipitation is not rare at all [12, 132, 36, 129], and that relativistic microbursts are either dominated by the night-side or have a comparable occurrence rate as those on the dawn and day sides—if we acknowledge that chorus waves are a main driver of relativistic microbursts [30, 150, 91, 77]—it naturally leads to the implication that ducts should exist on the night-side and be potentially quite common, so that they can account for the high occurrence rate of night-side relativistic precipitation. This is aligned with the statistical results on density irregularities [144, 55], where both works report a non-negligible occurrence rate on the night-side.

In this study, utilizing data from the ELFIN CubeSats, we examine a night-side relativistic precipitation event that reaches the strong diffusion limit ($j_{prec}/j_{trap} \sim 1$). By analyzing the energy dispersion and spatial burst signatures, we identify the presence of whistler-mode chorus wave–driven precipitation. Concurrent observations from multiple spacecraft (MMS, THEMIS, Arase, and GOES) reveal that this event is accompanied by substorm activity, hot electron injection, a low f_{pe}/f_{ce} ratio, and chorus wave activity. To elucidate the potential mechanism whereby night-side chorus waves produce relativistic precipitation at the strong diffusion limit, we conduct simulations modeling the chorus wave–driven precipitation for both the unducted and ducted cases. The model is event-based, with the density model and electron flux model configured based on observations during this event. The modeling results indicate that unducted night-side chorus waves are quickly damped before reaching relativistic resonance energies, and thus are unlikely to be responsible for strong relativistic precipitation; conversely, when chorus waves are effectively guided by a duct, they are able

to produce very intense precipitation ($j_{prec}/j_{trap} > 0.1$) across the relativistic energy range. Therefore, strong relativistic precipitation driven by chorus waves on the night-side can only be accompanied by the ducting effect. These results underline the critical role of density ducts in the dynamics of substorm radiation belts.

CHAPTER 7

Summary and conclusions

7.1 Summary

In this dissertation, we developed a new powerful tool for chorus wave driven electron precipitation modeling, and used it to investigate various questions of chorus wave driven relativistic electron microbursts, from microscopic wave-particle interaction mechanisms and single event features to macroscopic aspects such as global distribution of microburst features and global impact to the radiation belts.

Chapter 2 introduced the theoretical background of our modeling code, the Chorus Induced Particle Precipitation (CIPP) code. We introduced the workflow of the code in detail, demonstrating its ability to simulate the precipitation signature on arbitrary field lines due to equatorially generated chorus waves.

Chapter 3 presented the modeling of the spatial scale of relativistic electron microbursts induced by chorus waves, finding a representative scale size of approximately 60 km—consistent with previous observations. The modeling setup minimized the spatial and temporal extent of the chorus wave source, showing that the microburst scale is primarily governed by wave propagation rather than the physical size of the excitation region. The results further reveal that microbursts can be significantly displaced poleward from the chorus source L-shell and exhibit rapid poleward motion when observed on the ground or low Earth orbit. This displacement arises because chorus waves must reach higher latitudes and L-shells to satisfy relativistic resonance conditions. As a result, the traditionally assumed strict field-line con-

jugacy between chorus sources and microbursts is not necessary, underscoring the need to consider non-conjugate geometries in observational studies.

Chapter 4 presented the extended modeling framework to multiple chorus source regions distributed over L-shell and magnetic local times, enabling a global assessment of relativistic microburst spatial characteristics. Using statistically derived wave and electron properties as inputs, the model reproduced microbursts at all simulated locations. The results show that microbursts in the dawn and midnight sectors are comparable in intensity and scale, whereas those in the noon sector are significantly stronger and broader. This enhancement is attributed to reduced Landau damping in the dayside magnetosphere, where weaker keV electron populations permit chorus waves to reach higher latitudes and interact efficiently with MeV electrons. The findings highlight the controlling influence of lower-energy electrons on relativistic precipitation and provide a foundation for global quantification of microburst-driven losses.

Chapter 5 presented an investigation of the lifetimes of relativistic electrons in the outer radiation belt under the influence of chorus-driven microburst precipitation. Using the CIPP model and incorporating statistical distributions of chorus wave power and relativistic electron content, the study calculated loss rates and total electron content in each L-shell–MLT bin. The resulting lifetimes are on the order of tens of hours in the core outer belt region ($L = 5$–6.5), in agreement with prior observational studies, and extend to significantly longer durations at lower L-shells. The analysis demonstrates that chorus waves, during periods of elevated activity, can effectively deplete relativistic electrons within a few days. These results confirm the dominant role of chorus-driven microbursts in shaping outer belt electron lifetimes.

Chapter 6 presented a demonstration showing that strong relativistic precipitation on the night-side can only occur when chorus waves are guided by cold plasma density ducts. Using multi-spacecraft observations and event-based modeling informed by ELFIN measurements, the study showed that unducted chorus waves are rapidly damped before reaching

energies needed for relativistic electron resonance. In contrast, ducted waves retain sufficient amplitude during propagation and are able to precipitate relativistic electrons at intensities approaching the strong diffusion limit ($j_{prec}/j_{trap} \sim 1$). The modeled plasma conditions during the event—specifically a reduced f_{pe}/f_{ce} ratio consistent with substorm-driven cold plasma transport—support the feasibility of duct formation on the night-side. These results confirm that night-side chorus-driven relativistic electron precipitation requires ducted wave propagation, and they provide strong evidence that such ducts play a critical role in facilitating efficient wave-particle interactions at relativistic energies. The frequent observation of night-side microbursts suggests that density ducts may be more common than previously assumed, and their presence is essential to account for the observed occurrence rates of relativistic precipitation events in this region.

7.2 Discussion

The research presented in this dissertation has greatly advanced our understanding of the characteristics and significance of chorus wave driven relativistic microbursts. We explored the spatiotemporal characteristics of relativistic microbursts and revealed their close relationship to the chorus wave propagation effect, and inferred the global distribution and global impact of relativistic microbursts based on chorus wave data. These results have important implications that are discussed below.

Previous studies examining the relationship between relativistic microburst and chorus waves all focus on strict field line conjunction, which implies that either only equatorial chorus waves are involved in electron scattering, or chorus waves are assumed to be strictly field aligned propagating. We have demonstrated that neither implication is valid in general. To reach relativistic resonance energies, high latitude chorus waves are required and equatorial chorus waves cannot interact with relativistic electrons. Meanwhile, ray tracing results also indicate that chorus waves are usually not field aligned propagating, but instead mostly

shift to outer L-shells as they propagate to higher latitudes. Our study results indicate that relativistic microbursts occur at higher L-shell than the L-shell of the chorus waves which drive the microburst. These results provide new insights and suggestions for future observational studies: provided an observed relativistic microburst event by LEO spacecraft, we should look at equatorial regions at lower L-shell or high-latitude region at the same L-shell to find the conjugate chorus event that drives the observed microburst.

To the author's knowledge, current studies have not discussed the evolution of the location of the relativistic microbursts. The relativistic microbursts have been treated as a phenomenon of pure temporal evolution at a fixed location, maybe due to the limitation of single in situ spacecraft observations. However, we showed that microbursts are not a localized phenomenon. Instead, the microburst peak moves poleward with a very significant velocity $\approx 1000km/s$, and during the whole microburst event, the microburst peak can swipe over a large region spanning over $\approx 300km$, corresponding to a latitude interval of $\approx 3°$. The movement of relativistic microburst has not been proposed before, and therefore requires a lot of further observational investigation to confirm such prediction. The predicted poleward movement of relativistic microburst should leave a precipitation trajectory on the ionosphere, which might be observable by ground-based or balloon-based X-ray detector array.

Our estimation of relativistic electron lifetime due to chorus driven microburst is based completely on chorus wave data, therefore we only consider the precipitation related to chorus waves. Moreover, even though chorus waves play a dual role of both scattering relativistic electrons and acceleration of seed electrons to relativistic energy, our method only consider the scattering loss. It should be clearly noted that the acceleration occurs at large pitch angles $\alpha \approx 90°$, while the scattering loss occurs at pitch angles near the loss cone $\alpha \approx \alpha_{lc}$. Our code only consider the dynamic processes near the loss cone, therefore the acceleration role of the chorus waves are not considered.

In reality, multiple source and loss processes are always occurring simultaneously in the radiation belts, therefore our estimated lifetime of several tens hours only reflects the

importance of the certain process of chorus driven microburst loss, and does not necessarily match the realistic electron lifetime as other processes also simultaneously contribute. For example, the chorus acceleration might refill the radiation belt as the same chorus wave population scattering the relativistic electrons, thus the relativistic electron might lose slower or even be populated, depending on the lifetime related to each source or loss processes.

One of the key factors missing in the work of this dissertation, however, is that we have been neglecting the chirping rate of the chorus waves. All of our modeling assumes all wave frequency components are launched simultaneously from the equatorial source region. In reality, however, the chorus wave elements are always characterized by a frequency chirping rate, and such chirping rate is modulated by L-shell and MLT [141]. Preliminary modeling efforts have shown that a large chirping rate of $\gtrsim 5000Hz/s$ has minor impact on the modeling results. However, more detailed analysis on the role of chirping rate is still needed.

7.3 Proposed future studies

Following the discussion above, we propose a few future directions this dissertation naturally leads to, and may complete the arguments of current dissertation or extend to areas that have not been explored by current works.

7.3.1 The effect of chorus chirping rate

One straightforward but important work is to carefully analyze the impact of the chorus wave chirping rate on the microburst spatiotemporal distribution. Although preliminary attempts have shown that a large chirping rate of $\gtrsim 5000Hz/s$ has only negligible impact, previous studies of the chorus wave chirping rate [141, 58] also show that a large fraction of chorus waves have average chirping rate lower than $5000Hz/s$, especially the dawn and noon sectors where the chirping rate can be as low as only several hundreds Hz/s. Therefore a better understanding of the controlling effect of chirping rate on electron precipitation

signature is crucial. By simply setting the same modeled event with different chirping rate, we can investigate the impact of chirping rate on the microburst duration, scale size and amplitude, with an expectation that the duration of the microburts might be prolonged with lower chirping rate.

7.3.2 Optimize Landau damping calculation

Our studies presented in Chapters 4 and 6 both highlight the critical role of Landau damping on controlling the relativistic microburst, either through the Landau energy flux level difference or ducting effect. Landau damping controls the access of chorus wave to high latitude regions and hence the balance between chorus as a loss or source mechanism for the radiation belts. It is therefore imperative to optimize the Landau damping calculation procedure in our code so that our modeling results can be more reliable. Currently we adopt a very rough model where each ray's Landau damping rate is solely computed according to the electron flux model at its source region. Such calculation can be accurate for the near-equatorial propagation, but may lead to error when rays propagate away from the source region, i.e. to other L-shells and to higher latitudes. A more reasonable Landau damping model should be developed which calculate the Landau damping rate based on the ray's *local* electron flux.

7.3.3 The effect of chorus ducting

We had a preliminary attempt of studying the effect of density duct in Chapter 6, but only for a single event. With a single event approach established, it is plausible to combine the statistical results of density duct and include the density duct effect in predicting global distribution (Chapter 4) and estimating relativistic electron lifetime (Chapter 5), therefore obtaining more realistic and reliable results. It is also worth mentioning that the results we obtained in Chapter 4 and 5, despite of the overall agreement, still have minor but notable deviation with existing statistical works ([46, 145], etc.). The missing ducting effect

and the previously mentioned oversimplified Landau damping model might be major factors contributing to the deviations.

7.3.4 Observational comparison

The final and the most exciting work proposal is the observational validation of our modeling works. We predict the poleward movement of relativistic microburst for the first time, which requires observational confirmation. The major difficulty is to obtain a spatial resolution of the relativistic microburst. We propose two possible observation work plans. The first is to use the balloon based X-ray detector array to obtain the spatial resolution. The second and more promising solution is to use high time resolution twin LEO spacecrafts such as FIREBIRD II [65] and AeroCube-6 [116], and search for an event where two spacecrafts are separated by $\approx 1^\circ$ of latitude on their polar orbit and subsequently observe identical relativistic precipitation flux peak with the more poleward spacecraft lagged out by a small time interval. With such event not only we can demonstrate the poleward movement of the relativistic microburst, but also we can measure the velocity of the poleward movement by dividing the separated length of the two spacecrafts with the lagged time interval, and see if the measured velocity matches with the prediction of our modeling.

The proposed future studies not only refine and complete the current modeling framework developed in this dissertation but also open new directions for understanding the physics of wave–particle interactions in Earth's radiation belts. By addressing the unresolved factors such as chirping rate dependence, ducting effects, and more realistic damping models, and by pursuing observational validation, these works contribute to a more comprehensive and predictive description of relativistic electron precipitation. This is essential for quantifying radiation belt loss processes, assessing space weather impacts, and advancing our fundamental understanding of magnetospheric dynamics—key goals in space physics research.

REFERENCES

[1] O Agapitov, D Mourenas, A Artemyev, G Hospodarsky, and JW Bonnell. Time scales for electron quasi-linear diffusion by lower-band chorus waves: The effects of $\omega pe/\omega ce$ dependence on geomagnetic activity. *Geophysical Research Letters*, 46(12):6178–6187, 2019.

[2] O Agapitov, D Mourenas, A Artemyev, FS Mozer, JW Bonnell, V Angelopoulos, V Shastun, and V Krasnoselskikh. Spatial extent and temporal correlation of chorus and hiss: Statistical results from multipoint themis observations. *Journal of Geophysical Research: Space Physics*, 123(10):8317–8330, 2018.

[3] Oleksiy Agapitov, Anton Artemyev, Vladimir Krasnoselskikh, Yuri V Khotyaintsev, Didier Mourenas, Hugo Breuillard, Michael Balikhin, and Guy Rolland. Statistics of whistler mode waves in the outer radiation belt: Cluster staff-sa measurements. *Journal of Geophysical Research: Space Physics*, 118(6):3407–3420, 2013.

[4] JM Albert. Nonlinear interaction of outer zone electrons with vlf waves. *Geophysical research letters*, 29(8):116–1, 2002.

[5] Hayley J Allison, Yuri Y Shprits, Irina S Zhelavskaya, Dedong Wang, and Artem G Smirnov. Gyroresonant wave-particle interactions with chorus waves during extreme depletions of plasma density in the van allen radiation belts. *Science Advances*, 7(5):eabc0380, 2021.

[6] KA Anderson and DW Milton. Balloon observations of x rays in the auroral zone: 3. high time resolution studies. *Journal of Geophysical Research*, 69(21):4457–4479, 1964.

[7] V Angelopoulos, X-J Zhang, AV Artemyev, D Mourenas, E Tsai, C Wilkins, A Runov, J Liu, DL Turner, W Li, et al. Energetic electron precipitation driven by electromagnetic ion cyclotron waves from elfin's low altitude perspective. *Space Science Reviews*, 219(5):37, 2023.

[8] Vassilis Angelopoulos. *The THEMIS mission*. Springer, 2009.

[9] Vassilis Angelopoulos, E Tsai, L Bingley, C Shaffer, DL Turner, A Runov, Wen Li, J Liu, AV Artemyev, X-J Zhang, et al. The elfin mission. *Space science reviews*, 216:1–45, 2020.

[10] Anton V Artemyev, AG Demekhov, X-J Zhang, V Angelopoulos, D Mourenas, Yu V Fedorenko, J Maninnen, E Tsai, C Wilkins, S Kasahara, et al. Role of ducting in relativistic electron loss by whistler-mode wave scattering. *Journal of Geophysical Research: Space Physics*, 126(11):e2021JA029851, 2021.

[11] AV Artemyev, AI Neishtadt, and Vassilis Angelopoulos. On the role of whistler-mode waves in electron interaction with dipolarizing flux bundles. *Journal of Geophysical Research: Space Physics*, 127(4):e2022JA030265, 2022.

[12] AV Artemyev, X-J Zhang, AG Demekhov, X Meng, V Angelopoulos, and Yu V Fedorenko. Relativistic electron precipitation driven by mesoscale transients, inferred from ground and multi-spacecraft platforms. *Journal of Geophysical Research: Space Physics*, 129(2):e2023JA032287, 2024.

[13] AV Artemyev, X-J Zhang, Y Zou, D Mourenas, V Angelopoulos, D Vainchtein, E Tsai, and C Wilkins. On the nature of intense sub-relativistic electron precipitation. *Journal of Geophysical Research: Space Physics*, 127(6):e2022JA030571, 2022.

[14] HU Auster, KH Glassmeier, W Magnes, O Aydogar, W Baumjohann, D Constantinescu, D Fischer, KH Fornacon, E Georgescu, P Harvey, et al. The themis fluxgate magnetometer. *Space science reviews*, 141:235–264, 2008.

[15] Daniel N Baker. Satellite anomalies due to space storms: The effects of space weather on spacecraft systems and subsystems. *Space storms and space weather hazards*, pages 285–311, 2001.

[16] Daniel N Baker. How to cope with space weather. *Science*, 297(5586):1486–1487, 2002.

[17] DN Baker, SG Kanekal, VC Hoxie, MG Henderson, X Li, Harlan E Spence, SR Elkington, RHW Friedel, J Goldstein, MK Hudson, et al. A long-lived relativistic electron storage ring embedded in earth's outer van allen belt. *Science*, 340(6129):186–190, 2013.

[18] Timothy F Bell. The nonlinear gyroresonance interaction between energetic electrons and coherent vlf waves propagating at an arbitrary angle with respect to the earth's magnetic field. *Journal of Geophysical Research: Space Physics*, 89(A2):905–918, 1984.

[19] JB Blake, MD Looper, DN Baker, R Nakamura, B Klecker, and D Hovestadt. New high temporal and spatial resolution measurements by sampex of the precipitation of relativistic electrons. *Advances in Space Research*, 18(8):171–186, 1996.

[20] JB Blake, BH Mauk, DN Baker, P Carranza, JH Clemmons, J Craft, WR Crain, A Crew, Y Dotan, JF Fennell, et al. The fly's eye energetic particle spectrometer (feeps) sensors for the magnetospheric multiscale (mms) mission. *Space Science Reviews*, 199:309–329, 2016.

[21] JW Bonnell, FS Mozer, GT Delory, AJ Hull, RE Ergun, CM Cully, V Angelopoulos, and PR Harvey. The electric field instrument (efi) for themis. *The THEMIS mission*, pages 303–341, 2009.

[22] J Bortnik, L Chen, W Li, RM Thorne, and RB Horne. Modeling the evolution of chorus waves into plasmaspheric hiss. *Journal of Geophysical Research: Space Physics*, 116(A8), 2011.

[23] J Bortnik and RM Thorne. The dual role of elf/vlf chorus waves in the acceleration and precipitation of radiation belt electrons. *Journal of Atmospheric and Solar-Terrestrial Physics*, 69(3):378–386, 2007.

[24] J Bortnik, RM Thorne, and NP Meredith. Modeling the propagation characteristics of chorus using crres suprathermal electron fluxes. *Journal of Geophysical Research: Space Physics*, 112(A8), 2007.

[25] Jacob Bortnik, Umran S Inan, and Timothy F Bell. Temporal signatures of radiation belt electron precipitation induced by lightning-generated mr whistler waves: 1. methodology. *Journal of Geophysical Research: Space Physics*, 111(A2), 2006.

[26] Jacob Bortnik, Umran S Inan, and Timothy F Bell. Temporal signatures of radiation belt electron precipitation induced by lightning-generated mr whistler waves: 2. global signatures. *Journal of Geophysical Research: Space Physics*, 111(A2), 2006.

[27] Jacob Bortnik, Wen Li, RM Thorne, Vassilis Angelopoulos, Christopher Cully, John Bonnell, Olivier Le Contel, and Alain Roux. An observation linking the origin of plasmaspheric hiss to discrete chorus emissions. *Science*, 324(5928):775–778, 2009.

[28] Jacob Bortnik, Richard M Thorne, and Nigel P Meredith. The unexpected origin of plasmaspheric hiss from discrete chorus emissions. *Nature*, 452(7183):62–66, 2008.

[29] Jacob Bortnik, RM Thorne, and Umran S Inan. Nonlinear interaction of energetic electrons with large amplitude chorus. *Geophysical Research Letters*, 35(21), 2008.

[30] AW Breneman, Alex Crew, John Sample, David Klumpar, Arlo Johnson, Oleksiy Agapitov, Mykhaylo Shumko, DL Turner, O Santolik, John R Wygant, et al. Observations directly linking relativistic electron microbursts to whistler mode chorus: Van allen probes and firebird ii. *Geophysical Research Letters*, 44(22):11–265, 2017.

[31] AL Brinca. On the stability of obliquely propagating whistlers. *Journal of Geophysical Research*, 77(19):3495–3507, 1972.

[32] JL Burch, TE Moore, RB Torbert, and BL-https Giles. Magnetospheric multiscale overview and science objectives. *Space Science Reviews*, 199:5–21, 2016.

[33] WJ Burtis and RA Helliwell. Banded chorus—a new type of vlf radiation observed in the magnetosphere by ogo 1 and ogo 3. *Journal of Geophysical Research*, 74(11):3002–3010, 1969.

[34] L Capannolo, W Li, R Millan, D Smith, N Sivadas, J Sample, and S Shekhar. Relativistic electron precipitation near midnight: Drivers, distribution, and properties. *Journal of Geophysical Research: Space Physics*, 127(1):e2021JA030111, 2022.

[35] DL Carpenter and RR Anderson. An isee/whistler model of equatorial electron density in the magnetosphere. *Journal of Geophysical Research: Space Physics*, 97(A2):1097–1108, 1992.

[36] Huayue Chen, Xinliang Gao, Quanming Lu, and Bruce T Tsurutani. Global distribution of relativistic electron precipitation and the dependences on substorm injection and solar wind ram pressure: Long-term poes observations. *Journal of Geophysical Research: Space Physics*, 128(11):e2023JA031566, 2023.

[37] Lunjin Chen, Aaron W Breneman, Zhiyang Xia, and Xiao-jia Zhang. Modeling of bouncing electron microbursts induced by ducted chorus waves. *Geophysical Research Letters*, 47(17):e2020GL089400, 2020.

[38] Lunjin Chen, Richard M Thorne, Wen Li, and Jacob Bortnik. Modeling the wave normal distribution of chorus waves. *Journal of Geophysical Research: Space Physics*, 118(3):1074–1088, 2013.

[39] Lunjin Chen, Xiao-Jia Zhang, Anton Artemyev, Vassilis Angelopoulos, Ethan Tsai, Colin Wilkins, and Richard B Horne. Ducted chorus waves cause sub-relativistic and relativistic electron microbursts. *Geophysical Research Letters*, 49(5):e2021GL097559, 2022.

[40] Lunjin Chen, Xiao-Jia Zhang, Anton Artemyev, Liheng Zheng, Zhiyang Xia, Aaron W Breneman, and Richard B Horne. Electron microbursts induced by nonducted chorus waves. *Frontiers in Astronomy and Space Sciences*, 8:745927, 2021.

[41] Rui Chen, Xinliang Gao, Quanming Lu, Lunjin Chen, Bruce T Tsurutani, Wen Li, Binbin Ni, and Shui Wang. In situ observations of whistler-mode chorus waves guided by density ducts. *Journal of Geophysical Research: Space Physics*, 126(4):e2020JA028814, 2021.

[42] Ho-Sung Choi, Jaejin Lee, Kyung-Suk Cho, Young-Sil Kwak, Il-Hyun Cho, Young-Deuk Park, Yeon-Han Kim, Daniel N Baker, Geoffrey D Reeves, and Dong-Kyu Lee. Analysis of geo spacecraft anomalies: Space weather relationships. *Space weather*, 9(6), 2011.

[43] Alexander B Crew, Harlan E Spence, J Bernard Blake, David M Klumpar, Brian A Larsen, T Paul O'Brien, Shane Driscoll, Matthew Handley, Jason Legere, Stephen Longworth, et al. First multipoint in situ observations of electron microbursts: Initial results from the nsf firebird ii mission. *Journal of Geophysical Research: Space Physics*, 121(6):5272–5283, 2016.

[44] Nelson Henriques Dantas. *OGO4 SATELLITE OBSERVATIONS OF WHISTLER-MODE PROPAGATION EFFECTS ASSOCIATED WITH CAUSTICS IN THE MAGNETOSPHERE*. Stanford University, 1973.

[45] F Darrouzet, PME Décréau, J De Keyser, A Masson, DL Gallagher, O Santolik, BR Sandel, Jean-Gabriel Trotignon, Jean-Louis Rauch, E Le Guirriec, et al. Density structures inside the plasmasphere: Cluster observations. In *Annales Geophysicae*, volume 22, pages 2577–2585. Copernicus GmbH, 2004.

[46] E Douma, CJ Rodger, LW Blum, TP O'Brien, MA Clilverd, and JB Blake. Characteristics of relativistic microburst intensity from sampex observations. *Journal of Geophysical Research: Space Physics*, 124(7):5627–5640, 2019.

[47] Emma Douma, Craig J Rodger, Lauren W Blum, and Mark A Clilverd. Occurrence characteristics of relativistic electron microbursts from sampex observations. *Journal of Geophysical Research: Space Physics*, 122(8):8096–8107, 2017.

[48] Xiangrong Fu, Misa M Cowee, Reinhard H Friedel, Herbert O Funsten, S Peter Gary, George B Hospodarsky, Craig Kletzing, William Kurth, Brian A Larsen, Kaijun Liu, et al. Whistler anisotropy instabilities as the source of banded chorus: Van allen probes observations and particle-in-cell simulations. *Journal of Geophysical Research: Space Physics*, 119(10):8288–8298, 2014.

[49] Longzhi Gan, Anton Artemyev, Wen Li, Xiao-Jia Zhang, Qianli Ma, Didier Mourenas, Vassilis Angelopoulos, Ethan Tsai, and Colin Wilkins. Bursty energetic electron precipitation by high-order resonance with very-oblique whistler-mode waves. *Geophysical Research Letters*, 50(8):e2022GL101920, 2023.

[50] Xinliang Gao, Lunjin Chen, Wen Li, Quanming Lu, and Shui Wang. Statistical results of the power gap between lower-band and upper-band chorus waves. *Geophysical Research Letters*, 46(8):4098–4105, 2019.

[51] S Peter Gary and Joseph Wang. Whistler instability: Electron anisotropy upper bound. *Journal of Geophysical Research: Space Physics*, 101(A5):10749–10754, 1996.

[52] JW Gjerloev. The supermag data processing technique. *Journal of Geophysical Research: Space Physics*, 117(A9), 2012.

[53] Matina Gkioulidou, AY Ukhorskiy, DG Mitchell, T Sotirelis, BH Mauk, and LJ Lanzerotti. The role of small-scale ion injections in the buildup of earth's ring current pressure: Van allen probes observations of the 17 march 2013 storm. *Journal of Geophysical Research: Space Physics*, 119(9):7327–7342, 2014.

[54] AD Greeley, SG Kanekal, DN Baker, B Klecker, and Q Schiller. Quantifying the contribution of microbursts to global electron loss in the radiation belts. *Journal of Geophysical Research: Space Physics*, 124(2):1111–1124, 2019.

[55] Wenyao Gu, Xu Liu, Zhiyang Xia, and Lunjin Chen. Statistical study on small-scale (less than 1,000 km) density irregularities in the inner magnetosphere. *Journal of Geophysical Research: Space Physics*, 127(7):e2022JA030574, 2022.

[56] Miroslav Hanzelka and Ondřej Santolík. Effects of ducting on whistler mode chorus or exohiss in the outer radiation belt. *Geophysical Research Letters*, 46(11):5735–5745, 2019.

[57] J. Haselgrove. Ray theory and a new method for ray tracing. *Report of the Physical Society Conference on Physics of the Ionosphere*, 1954.

[58] Jiabei He, Zhiyang Xia, and Lunjin Chen. Statistical properties of lower band rising tone chorus waves. *Journal of Geophysical Research: Space Physics*, 128(9):e2023JA031528, 2023.

[59] Mitsuru Hikishima, Yoshiharu Omura, and Danny Summers. Microburst precipitation of energetic electrons associated with chorus wave generation. *Geophysical Research Letters*, 37(7), 2010.

[60] Richard B Horne and Richard M Thorne. Potential waves for relativistic electron scattering and stochastic acceleration during magnetic storms. *Geophysical Research Letters*, 25(15):3011–3014, 1998.

[61] Richard B Horne, Richard M Thorne, Yuri Y Shprits, Nigel P Meredith, Sarah A Glauert, Andy J Smith, Shrikanth G Kanekal, Daniel N Baker, Mark J Engebretson, Jennifer L Posch, et al. Wave acceleration of electrons in the van allen radiation belts. *Nature*, 437(7056):227–230, 2005.

[62] WL Imhof, JB Reagan, and EE Gaines. Studies of the sharply defined l dependent energy threshold for isotropy at the midnight trapping boundary. *Journal of Geophysical Research: Space Physics*, 84(A11):6371–6384, 1979.

[63] WL Imhof, HD Voss, J Mobilia, DW Datlowe, EE Gaines, JP McGlennon, and US Inan. Relativistic electron microbursts. *Journal of Geophysical Research: Space Physics*, 97(A9):13829–13837, 1992.

[64] Umran S Inan and Timothy F Bell. The plasmapause as a vlf wave guide. *Journal of Geophysical Research*, 82(19):2819–2827, 1977.

[65] AT Johnson, Mykhaylo Shumko, B Griffith, David M Klumpar, John Sample, Larry Springer, N Leh, HE Spence, S Smith, A Crew, et al. The firebird-ii cubesat mission: Focused investigations of relativistic electron burst intensity, range, and dynamics. *Review of Scientific Instruments*, 91(3), 2020.

[66] Ning Kang, Anton V Artemyev, Jacob Bortnik, Xiao-Jia Zhang, and Vassilis Angelopoulos. The principal role of chorus ducting for night-side relativistic electron precipitation. *Geophysical Research Letters*, 51(17):e2024GL110365, 2024.

[67] Ning Kang, Jacob Bortnik, Xin An, and Seth G Claudepierre. Propagation of chorus waves generated in minimum-b pockets. *Geophysical Research Letters*, 48(24):e2021GL096478, 2021.

[68] Ning Kang, Jacob Bortnik, Qianli Ma, and Seth Claudepierre. Modeling the global distribution of chorus wave induced relativistic microburst spatial characteristics. *Journal of Geophysical Research: Space Physics*, 129(3):e2023JA032250, 2024.

[69] Ning Kang, Jacob Bortnik, Xiaojia Zhang, Seth Claudepierre, and Xiaofei Shi. Relativistic microburst scale size induced by a single point-source chorus element. *Geophysical Research Letters*, 49(23):e2022GL100841, 2022.

[70] Satoshi Kasahara, Shoichiro Yokota, Takefumi Mitani, Kazushi Asamura, Masafumi Hirahara, Yasuko Shibano, and Takeshi Takashima. Medium-energy particle experiments—electron analyzer (mep-e) for the exploration of energization and radiation in geospace (erg) mission. *Earth, Planets and Space*, 70(1):1–16, 2018.

[71] Yoshiya Kasahara, Yasumasa Kasaba, Hirotsugu Kojima, Satoshi Yagitani, Keigo Ishisaka, Atsushi Kumamoto, Fuminori Tsuchiya, Mitsunori Ozaki, Shoya Matsuda, Tomohiko Imachi, et al. The plasma wave experiment (pwe) on board the arase (erg) satellite. *Earth, Planets and Space*, 70:1–28, 2018.

[72] Miki Kawamura, Takeshi Sakanoi, Mizuki Fukizawa, Yoshizumi Miyoshi, Keisuke Hosokawa, Fuminori Tsuchiya, Yuto Katoh, Yasunobu Ogawa, Kazushi Asamura, Shinji Saito, et al. Simultaneous pulsating aurora and microburst observations with ground-based fast auroral imagers and cubesat firebird-ii. *Geophysical Research Letters*, 48(18):e2021GL094494, 2021.

[73] Yangguang Ke, Lunjin Chen, Xinliang Gao, Quanming Lu, Xueyi Wang, Rui Chen, Huayue Chen, and Shui Wang. Whistler-mode waves trapped by density irregularities in the earth's magnetosphere. *Geophysical Research Letters*, 48(7):e2020GL092305, 2021.

[74] Charles F Kennel. Consequences of a magnetospheric plasma. *Reviews of Geophysics*, 7(1-2):379–419, 1969.

[75] Charles F Kennel and HE Petschek. Limit on stably trapped particle fluxes. *Journal of Geophysical Research*, 71(1):1–28, 1966.

[76] Charles F Kennel and Richard Mansergh Thorne. Unstable growth of unducted whistlers propagating at an angle to the geomagnetic field. *Journal of Geophysical Research*, 72(3):871–878, 1967.

[77] K Kersten, CA Cattell, A Breneman, K Goetz, PJ Kellogg, JR Wygant, LB Wilson III, JB Blake, MD Looper, and I Roth. Observation of relativistic electron microbursts in conjunction with intense radiation belt whistler-mode waves. *Geophysical Research Letters*, 38(8), 2011.

[78] Iwane Kimura. Effects of ions on whistler-mode ray tracing. *Radio Science*, 1(3):269–283, 1966.

[79] Wilhelm Kutta. *Beitrag zur näherungsweisen Integration totaler Differentialgleichungen*. Teubner, 1901.

[80] David Scott Lauben, Umran S Inan, Timothy F Bell, and DA Gurnett. Source characteristics of elf/vlf chorus. *Journal of Geophysical Research: Space Physics*, 107(A12):SMP–10, 2002.

[81] O Le Contel, A Roux, P Robert, C Coillot, Abdel Bouabdellah, B de La Porte, D Alison, Sébastien Ruocco, V Angelopoulos, K Bromund, et al. First results of the themis search coil magnetometers. *The THEMIS mission*, pages 509–534, 2009.

[82] MJ LeDocq, DA Gurnett, and GB Hospodarsky. Chorus source locations from vlf poynting flux measurements with the polar spacecraft. *Geophysical Research Letters*, 25(21):4063–4066, 1998.

[83] Jinxing Li, Jacob Bortnik, Wen Li, Xin An, Larry R Lyons, William S Kurth, George B Hospodarsky, David P Hartley, Geoffrey D Reeves, Herbert O Funsten, et al. Unraveling the formation region and frequency of chorus spectral gaps. *Geophysical Research Letters*, 49(19):e2022GL100385, 2022.

[84] W Li, J Bortnik, RM Thorne, and V Angelopoulos. Global distribution of wave amplitudes and wave normal angles of chorus waves using themis wave observations. *Journal of Geophysical Research: Space Physics*, 116(A12), 2011.

[85] W Li, J Bortnik, RM Thorne, Y Nishimura, V Angelopoulos, and L Chen. Modulation of whistler mode chorus waves: 2. role of density variations. *Journal of Geophysical Research: Space Physics*, 116(A6), 2011.

[86] W Li and MK Hudson. Earth's van allen radiation belts: From discovery to the van allen probes era. *Journal of Geophysical Research: Space Physics*, 124(11):8319–8351, 2019.

[87] W Li, B Ni, RM Thorne, J Bortnik, JC Green, CA Kletzing, WS Kurth, and GB Hospodarsky. Constructing the global distribution of chorus wave intensity using measurements of electrons by the poes satellites and waves by the van allen probes. *Geophysical Research Letters*, 40(17):4526–4532, 2013.

[88] W Li, RM Thorne, V Angelopoulos, J Bortnik, Chris M Cully, B Ni, Olivier LeContel, A Roux, U Auster, and W Magnes. Global distribution of whistler-mode chorus waves observed on the themis spacecraft. *Geophysical Research Letters*, 36(9), 2009.

[89] YuXuan Li, Chao Yue, Ying Liu, Qiu-Gang Zong, Hong Zou, and YuGuang Ye. Dynamics of the inner electron radiation belt: A review. *Earth and Planetary Physics*, 7(1):109–118, 2022.

[90] Jiang Liu, Vassilis Angelopoulos, Xiao-Jia Zhang, Drew L Turner, Christine Gabrielse, Andrei Runov, Jinxing Li, Herbert O Funsten, and HE Spence. Dipolarizing flux bundles in the cis-geosynchronous magnetosphere: Relationship between electric fields and energetic particle injections. *Journal of Geophysical Research: Space Physics*, 121(2):1362–1376, 2016.

[91] KR Lorentzen, JB Blake, US Inan, and J Bortnik. Observations of relativistic electron microbursts in association with vlf chorus. *Journal of Geophysical Research: Space Physics*, 106(A4):6017–6027, 2001.

[92] KR Lorentzen, MD Looper, and JB Blake. Relativistic electron microbursts during the gem storms. *Geophysical Research Letters*, 28(13):2573–2576, 2001.

[93] Quanming Lu, Yangguang Ke, Xueyi Wang, Kaijun Liu, Xinliang Gao, Lunjin Chen, and Shui Wang. Two-dimensional gcpic simulation of rising-tone chorus waves in a dipole magnetic field. *Journal of Geophysical Research: Space Physics*, 124(6):4157–4167, 2019.

[94] AS Lukin, AV Artemyev, AA Petrukovich, and X-J Zhang. Charged particle scattering in dipolarized magnetotail. *Physics of Plasmas*, 28(10), 2021.

[95] Lawrence R Lyons and Richard Mansergh Thorne. Equilibrium structure of radiation belt electrons. *Journal of Geophysical Research*, 78(13):2142–2149, 1973.

[96] Q Ma, HK Connor, X-J Zhang, W Li, X-C Shen, D Gillespie, CA Kletzing, WS Kurth, GB Hospodarsky, SG Claudepierre, et al. Global survey of plasma sheet electron precipitation due to whistler mode chorus waves in earth's magnetosphere. *Geophysical Research Letters*, 47(15):e2020GL088798, 2020.

[97] Qianli Ma, Wen Li, Richard M Thorne, Y Nishimura, X-J Zhang, Geoffrey D Reeves, CA Kletzing, WS Kurth, GB Hospodarsky, MG Henderson, et al. Simulation of energy-dependent electron diffusion processes in the earth's outer radiation belt. *Journal of Geophysical Research: Space Physics*, 121(5):4217–4231, 2016.

[98] David M Malaspina, Aleksandr Ukhorskiy, Xiangning Chu, and John Wygant. A census of plasma waves and structures associated with an injection front in the inner magnetosphere. *Journal of Geophysical Research: Space Physics*, 123(4):2566–2587, 2018.

[99] Ian Robert Mann, LG Ozeke, Kyle R Murphy, Seth G Claudepierre, Drew L Turner, Daniel N Baker, IJ Rae, Andy Kale, David K Milling, Alexander J Boyd, et al. Explaining the dynamics of the ultra-relativistic third van allen radiation belt. *Nature Physics*, 12(10):978–983, 2016.

[100] RA Marshall and J Bortnik. Pitch angle dependence of energetic electron precipitation: Energy deposition, backscatter, and the bounce loss cone. *Journal of Geophysical Research: Space Physics*, 123(3):2412–2423, 2018.

[101] A Masson, US Inan, H Laakso, O Santolik, and Pierrette Décréau. Cluster observations of mid-latitude hiss near the plasmapause. In *Annales Geophysicae*, volume 22, pages 2565–2575. Copernicus Publications Göttingen, Germany, 2004.

[102] Nigel P Meredith, Richard B Horne, Angélica Sicard-Piet, Daniel Boscher, Keith H Yearby, Wen Li, and Richard M Thorne. Global model of lower band and upper band chorus from multiple satellite observations. *Journal of Geophysical Research: Space Physics*, 117(A10), 2012.

[103] Nigel P Meredith, Richard B Horne, Richard M Thorne, and Roger R Anderson. Favored regions for chorus-driven electron acceleration to relativistic energies in the earth's outer radiation belt. *Geophysical Research Letters*, 30(16), 2003.

[104] Y Miyoshi, K Hosokawa, S ea Kurita, S-I Oyama, Y Ogawa, S Saito, I Shinohara, A Kero, E Turunen, PT Verronen, et al. Penetration of mev electrons into the mesosphere accompanying pulsating aurorae. *Scientific Reports*, 11(1):13724, 2021.

[105] Y Miyoshi, S Oyama, S Saito, S Kurita, H Fujiwara, R Kataoka, Y Ebihara, C Kletzing, G Reeves, O Santolik, et al. Energetic electron precipitation associated with pulsating aurora: Eiscat and van allen probe observations. *Journal of Geophysical Research: Space Physics*, 120(4):2754–2766, 2015.

[106] Yoshizumi Miyoshi, Yuto Katoh, Takanori Nishiyama, Takeshi Sakanoi, Kazushi Asamura, and Masafumi Hirahara. Time of flight analysis of pulsating aurora electrons, considering wave-particle interactions with propagating whistler mode waves. *Journal of Geophysical Research: Space Physics*, 115(A10), 2010.

[107] Yoshizumi Miyoshi, Shinji Saito, Satoshi Kurita, Kazushi Asamura, Keisuke Hosokawa, Takeshi Sakanoi, Takefumi Mitani, Yasunobu Ogawa, Shin-ichiro Oyama, Fuminori Tsuchiya, et al. Relativistic electron microbursts as high-energy tail of pulsating aurora electrons. *Geophysical Research Letters*, 47(21):e2020GL090360, 2020.

[108] Yoshizumi Miyoshi, Iku Shinohara, Takeshi Takashima, Kazushi Asamura, Nana Higashio, Takefumi Mitani, Satoshi Kasahara, Shoichiro Yokota, Yoichi Kazama, Shiang-Yu Wang, et al. Geospace exploration project erg. *Earth, Planets and Space*, 70:1–13, 2018.

[109] O Moullard, A Masson, H Laakso, Michel Parrot, Pierrette Décréau, Ondřej Santolík, and M Andre. Density modulated whistler mode emissions observed near the plasmapause. *Geophysical Research Letters*, 29(20):36–1, 2002.

[110] R Nakamura, M Isowa, Y Kamide, DN Baker, JB Blake, and M Looper. Sampex observations of precipitation bursts in the outer radiation belt. *Journal of Geophysical Research: Space Physics*, 105(A7):15875–15885, 2000.

[111] Binbin Ni, Richard M Thorne, Yuri Y Shprits, and Jacob Bortnik. Resonant scattering of plasma sheet electrons by whistler-mode chorus: Contribution to diffuse auroral precipitation. *Geophysical Research Letters*, 35(11), 2008.

[112] Y Nishimura, LR Lyons, V Angelopoulos, T Kikuchi, S Zou, and SB Mende. Relations between multiple auroral streamers, pre-onset thin arc formation, and substorm auroral onset. *Journal of Geophysical Research: Space Physics*, 116(A9), 2011.

[113] TP O'brien, KR Lorentzen, IR Mann, NP Meredith, JB Blake, JF Fennell, MD Looper, DK Milling, and RR Anderson. Energization of relativistic electrons in the presence of ulf power and mev microbursts: Evidence for dual ulf and vlf acceleration. *Journal of Geophysical Research: Space Physics*, 108(A8), 2003.

[114] Yoshiharu Omura, Mitsuru Hikishima, Yuto Katoh, Danny Summers, and Satoshi Yagitani. Nonlinear mechanisms of lower-band and upper-band vlf chorus emissions in the magnetosphere. *Journal of Geophysical Research: Space Physics*, 114(A7), 2009.

[115] Yoshiharu Omura, Yuto Katoh, and Danny Summers. Theory and simulation of the generation of whistler-mode chorus. *Journal of Geophysical Research: Space Physics*, 113(A4), 2008.

[116] TP O'Brien, J Bernard Blake, Joseph W Gangestad, and Air Force Space Command. Aerocube-6 dosimeter data readme (v3. 0). Technical report, Aerospace Report No. TOR-2016-01155, 2016.

[117] GD Reeves, Harlan E Spence, MG Henderson, SK Morley, RHW Friedel, HO Funsten, DN Baker, SG Kanekal, JB Blake, JF Fennell, et al. Electron acceleration in the heart of the van allen radiation belts. *Science*, 341(6149):991–994, 2013.

[118] J-F Ripoll, SG Claudepierre, AY Ukhorskiy, Chris Colpitts, Xinlin Li, JF Fennell, and Chris Crabtree. Particle dynamics in the earth's radiation belts: Review of current research and open questions. *Journal of Geophysical Research: Space Physics*, 125(5):e2019JA026735, 2020.

[119] Carl Runge. Über die numerische auflösung von differentialgleichungen. *Mathematische Annalen*, 46(2):167–178, 1895.

[120] S Saito, Y Miyoshi, and K Seki. Relativistic electron microbursts associated with whistler chorus rising tone elements: Gemsis-rbw simulations. *Journal of Geophysical Research: Space Physics*, 117(A10), 2012.

[121] O Santolík, DA Gurnett, JS Pickett, Michel Parrot, and N Cornilleau-Wehrlin. Spatio-temporal structure of storm-time chorus. *Journal of Geophysical Research: Space Physics*, 108(A7), 2003.

[122] O Santolik, DA Gurnett, JS Pickett, Michel Parrot, and N Cornilleau-Wehrlin. Central position of the source region of storm-time chorus. *Planetary and Space Science*, 53(1-3):299–305, 2005.

[123] Ondřej Santolík, Eva Macúšová, Ivana Kolmašová, Nicole Cornilleau-Wehrlin, and Yvonne de Conchy. Propagation of lower-band whistler-mode waves in the outer van allen belt: Systematic analysis of 11 years of multi-component data from the cluster spacecraft. *Geophysical Research Letters*, 41(8):2729–2737, 2014.

[124] RS Selesnick and SG Kanekal. Variability of the total radiation belt electron content. *Journal of Geophysical Research: Space Physics*, 114(A2), 2009.

[125] A Seppälä, E Douma, CJ Rodger, PT Verronen, Mark A Clilverd, and J Bortnik. Relativistic electron microburst events: Modeling the atmospheric impact. *Geophysical Research Letters*, 45(2):1141–1147, 2018.

[126] V Sergeev, Y Nishimura, M Kubyshkina, V Angelopoulos, R Nakamura, and H Singer. Magnetospheric location of the equatorward prebreakup arc. *Journal of Geophysical Research: Space Physics*, 117(A1), 2012.

[127] VA Sergeev, EM Sazhina, NA Tsyganenko, JÅ Lundblad, and F Søraas. Pitch-angle scattering of energetic protons in the magnetotail current sheet as the dominant source of their isotropic precipitation into the nightside ionosphere. *Planetary and Space Science*, 31(10):1147–1155, 1983.

[128] BW Sheeley, MB Moldwin, HK Rassoul, and RR Anderson. An empirical plasmasphere and trough density model: Crres observations. *Journal of Geophysical Research: Space Physics*, 106(A11):25631–25641, 2001.

[129] Sapna Shekhar, Robyn Millan, and David Smith. A statistical study of the spatial extent of relativistic electron precipitation with polar orbiting environmental satellites. *Journal of Geophysical Research: Space Physics*, 122(11):11–274, 2017.

[130] Yangyang Shen, Anton V Artemyev, Xiao-Jia Zhang, Ying Zou, Vassilis Angelopoulos, Ivan Vasko, Andrei Runov, Ethan Tsai, and Colin Wilkins. Contribution of kinetic alfvén waves to energetic electron precipitation from the plasma sheet during a substorm. *Journal of Geophysical Research: Space Physics*, 128(4):e2023JA031350, 2023.

[131] Yangyang Shen, Lunjin Chen, Xiao-Jia Zhang, Anton Artemyev, Vassilis Angelopoulos, Christopher M Cully, H Gordon James, Andrew W Yau, Andrew D Howarth, Jacob Bortnik, et al. Conjugate observation of magnetospheric chorus propagating to the ionosphere by ducting. *Geophysical Research Letters*, 48(23):e2021GL095933, 2021.

[132] Mykhaylo Shumko, Lauren W Blum, and Alexander B Crew. Duration of individual relativistic electron microbursts: A probe into their scattering mechanism. *Geophysical Research Letters*, 48(17):e2021GL093879, 2021.

[133] Mykhaylo Shumko, Bea Gallardo-Lacourt, Alexa J Halford, Jun Liang, Lauren W Blum, E Donovan, Kyle Robert Murphy, and Emma Spanswick. A strong correlation between relativistic electron microbursts and patchy aurora. *Geophysical Research Letters*, 48(18):e2021GL094696, 2021.

[134] Mykhaylo Shumko, Arlo T Johnson, John G Sample, Brady A Griffith, Drew L Turner, Thomas Paul O'Brien, Oleksiy Agapitov, J Bernard Blake, and Seth G Claudepierre. Electron microburst size distribution derived with aerocube-6. *Journal of Geophysical Research: Space Physics*, 125(3):e2019JA027651, 2020.

[135] Mykhaylo Shumko, John Sample, Arlo Johnson, Bern Blake, Alex Crew, Harlan Spence, David Klumpar, Oleksiy Agapitov, and Matthew Handley. Microburst scale size derived from multiple bounces of a microburst simultaneously observed with the firebird-ii cubesats. *Geophysical Research Letters*, 45(17):8811–8818, 2018.

[136] Mikhail I Sitnov, Grant Killian Stephens, Nikolai A Tsyganenko, Yukinaga Miyashita, Viacheslav G Merkin, Tetsuo Motoba, Shinichi Ohtani, and Kevin James Genestreti. Signatures of nonideal plasma evolution during substorms obtained by mining multimission magnetometer data. *Journal of Geophysical Research: Space Physics*, 124(11):8427–8456, 2019.

[137] RL Smith and JJ Angerami. Magnetospheric properties deduced from ogo 1 observations of ducted and nonducted whistlers. *Journal of Geophysical Research*, 73(1):1–20, 1968.

[138] Thomas H Stix. *Waves in plasmas*. Springer Science & Business Media, 1992.

[139] AV Streltsov. Spectral properties of high-density ducts. *Journal of Geophysical Research: Space Physics*, 112(A12), 2007.

[140] Danny Summers, Binbin Ni, and Nigel P Meredith. Timescales for radiation belt electron acceleration and loss due to resonant wave-particle interactions: 2. evaluation for vlf chorus, elf hiss, and electromagnetic ion cyclotron waves. *Journal of Geophysical Research: Space Physics*, 112(A4), 2007.

[141] X Tao, W Li, J Bortnik, RM Thorne, and V Angelopoulos. Comparison between theory and observation of the frequency sweep rates of equatorial rising tone chorus. *Geophysical Research Letters*, 39(8), 2012.

[142] Xin Tao, RM Thorne, W Li, B Ni, NP Meredith, and RB Horne. Evolution of electron pitch angle distributions following injection from the plasma sheet. *Journal of Geophysical Research: Space Physics*, 116(A4), 2011.

[143] Shangchun Teng, Xin Tao, Wen Li, Yi Qi, Xinliang Gao, Lei Dai, Quanming Lu, and Shui Wang. A statistical study of the spatial distribution and source-region size of chorus waves using van allen probes data. In *Annales Geophysicae*, volume 36, pages 867–878. Copernicus Publications Gottingen, Germany, 2018.

[144] Neethal Thomas, Kazuo Shiokawa, Yoshizumi Miyoshi, Yoshiya Kasahara, Iku Shinohara, Atsushi Kumamoto, Fuminori Tsuchiya, Ayako Matsuoka, Satoshi Kasahara, Shoichiro Yokota, et al. Investigation of small-scale electron density irregularities observed by the arase and van allen probes satellites inside and outside the plasmasphere. *Journal of Geophysical Research: Space Physics*, 126(3):e2020JA027917, 2021.

[145] Richard M Thorne, TP O'Brien, YY Shprits, Danny Summers, and Richard B Horne. Timescale for mev electron microburst loss during geomagnetic storms. *Journal of Geophysical Research: Space Physics*, 110(A9), 2005.

[146] Richard Mansergh Thorne. Radiation belt dynamics: The importance of wave-particle interactions. *Geophysical Research Letters*, 37(22), 2010.

[147] RM Thorne, W Li, B Ni, Q Ma, J Bortnik, L Chen, DN Baker, Harlan E Spence, GD Reeves, MG Henderson, et al. Rapid local acceleration of relativistic radiation-belt electrons by magnetospheric chorus. *Nature*, 504(7480):411–414, 2013.

[148] Ethan Tsai, Anton Artemyev, Qianli Ma, Didier Mourenas, Oleksiy Agapitov, Xiao-Jia Zhang, and Vassilis Angelopoulos. Key factors determining nightside energetic electron losses driven by whistler-mode waves. *Journal of Geophysical Research: Space Physics*, 129(3):e2023JA032351, 2024.

[149] Ethan Tsai, Anton Artemyev, Xiao-Jia Zhang, and Vassilis Angelopoulos. Relativistic electron precipitation driven by nonlinear resonance with whistler-mode waves. *Journal of Geophysical Research: Space Physics*, 127(5):e2022JA030338, 2022.

[150] Bruce T Tsurutani, Gurbax S Lakhina, and Olga P Verkhoglyadova. Energetic electron (¿ 10 kev) microburst precipitation,˜ 5–15 s x-ray pulsations, chorus, and wave-particle interactions: A review. *Journal of Geophysical Research: Space Physics*, 118(5):2296–2312, 2013.

[151] Bruce T Tsurutani and Edward J Smith. Postmidnight chorus: A substorm phenomenon. *Journal of Geophysical Research*, 79(1):118–127, 1974.

[152] Bruce T Tsurutani and Edward J Smith. Two types of magnetospheric elf chorus and their substorm dependences. *Journal of Geophysical Research*, 82(32):5112–5128, 1977.

[153] Nikolai A Tsyganenko. A magnetospheric magnetic field model with a warped tail current sheet. *Planetary and Space Science*, 37(1):5–20, 1989.

[154] DL Turner, V Angelopoulos, SK Morley, MG Henderson, GD Reeves, W Li, DN Baker, C-L Huang, A Boyd, Harlan E Spence, et al. On the cause and extent of outer radiation belt losses during the 30 september 2012 dropout event. *Journal of Geophysical Research: Space Physics*, 119(3):1530–1540, 2014.

[155] Andris Vaivads, O Santolík, G Stenberg, Mats André, CJ Owen, P Canu, and M Dunlop. Source of whistler emissions at the dayside magnetopause. *Geophysical research letters*, 34(9), 2007.

[156] James Alfred Van Allen, George H Ludwig, Ernest Clark Ray, and Carl E McIlwain. Observation of high intensity radiation by satellites 1958 alpha and gamma. *Journal of Jet Propulsion*, 28(9):588–592, 1958.

[157] Fernando Walter. Nonducted vlf propagation in the magnetosphere. Technical report, 1969.

[158] David F Webb and Joe H Allen. Spacecraft and ground anomalies related to the october-november 2003 solar activity. *Space Weather*, 2(3), 2004.

[159] Colin Wilkins, Vassilis Angelopoulos, Andrei Runov, Anton Artemyev, X-J Zhang, Jiang Liu, and Ethan Tsai. Statistical characteristics of the electron isotropy boundary. *Journal of Geophysical Research: Space Physics*, 128(10):e2023JA031774, 2023.

[160] Irving Yabroff. *Computation of whistler ray paths*. Stanford Research Institute, 1959.

[161] AG Yahnin, TA Yahnina, NV Semenova, BB Gvozdevsky, and AB Pashin. Relativistic electron precipitation as seen by noaa poes. *Journal of Geophysical Research: Space Physics*, 121(9):8286–8299, 2016.

[162] Xiao-Jia Zhang, Vassilis Angelopoulos, Anton Artemyev, Didier Mourenas, Oleksiy Agapitov, Ethan Tsai, and Colin Wilkins. Temporal scales of electron precipitation driven by whistler-mode waves. *Journal of Geophysical Research: Space Physics*, 128(1):e2022JA031087, 2023.

[163] Xiao-Jia Zhang, Vassilis Angelopoulos, Didier Mourenas, Anton Artemyev, Ethan Tsai, and Colin Wilkins. Characteristics of electron microburst precipitation based on high-resolution elfin measurements. *Journal of Geophysical Research: Space Physics*, 127(5):e2022JA030509, 2022.